POLITECNICO DI MILANO
FACOLTÀ DI INGEGNERIA INDUSTRIALE
CORSO DI LAUREA SPECIALISTICA IN INGEGNERIA AERONAUTICA

An innovative Direct Numerical Simulation code for high-Reynolds-number turbulent pipe flow

Relatore:
prof. Maurizio Quadrio

Nicolò Fabbiane 739994

ANNO ACCADEMICO 2010/2011

“Forty-two.”
said Deep Thought,
with infinite majesty and calm.

ABSTRACT

A pseudo-spectral parallel code for the direct numerical simulation of incompressible Navier Stokes equations in a cylindrical domain is presented. The codes is aimed at making possible the numerical simulations of high Reynolds number pipe flow. The method is based on Fourier expansion in the azimuthal and axial direction and compact finite-differences schemes along radial direction. This code has the peculiar feature of being able to vary the number of azimuthal Fourier modes along the radial direction. This feature, that is intended for addressing high values of *Re* while keeping the computational cost under control, allows us to avoid that the spatial resolution, set at the pipe wall by physical considerations, grows unboundedly as the pipe axis is approached. After an initial description of equations and used numerical method, the validation is performed by optimal energy growth and statistical analysis of a fully developed turbulent flows at low *Re*.

Keywords: Direct Numerical Simulation, turbulent flows, pipe, cylindrical coordinates, compact finite-differences, variable modes, regularity conditions, optimal energy growth.

In questo lavoro viene presentato un programma per la risoluzione numerica delle equazioni di Navier Stokes in un dominio cilindrico. L'obiettivo dello sviluppo di questo codice è il rendere possibile simulare numericamente correnti ad alto numero di Reynolds in geometrie cilindriche. Il metodo di calcolo si basa su un'espansione di Fourier lungo la direzione assiale e angolare e su un metodo a differenze finite compatte lungo la direzione radiale. La caratteristica principale del codice sviluppato è la possibilità di variare il numero dei modi angolari lungo il raggio: questo, pensato per contenere il costo computazionale all'aumentare del numero di Reynolds, permette di evitare che la risoluzione spaziale, dettata da considerazioni fisiche a parete, cresca senza controllo all'avvicinarsi dell'asse. Dopo una prima parte in cui vengono introdotte le equazioni e i metodi numerici utilizzati, ci si presta a validare il codice di calcolo, prima con l'analisi della perturbazione ottima e, quindi, delle statistiche di un flusso turbolento, a basso numero di Reynolds, completamente sviluppato.

CONTENTS

1. Introduction 1

2. Direct Numerical Simulation code 5
  2.1 Governing equations 5
    2.1.1 Transformed equations 6
    2.1.2 Regularity conditions 8
  2.2 Numerical methods 8
    2.2.1 Time integration scheme 8
    2.2.2 Radial derivatives 9
    2.2.3 Spatial resolution in the azimuthal direction 11
  2.3 Algorithm 13
    2.3.1 Computing convolutions 14
    2.3.2 Time step 15
    2.3.3 Files format 15
  2.4 Parallel strategies 17
    2.4.1 Parallel performances 19

3. Optimal energy growth 21
  3.1 Theoretical background 21
    3.1.1 Governing equations 21
    3.1.2 Kinetic energy and energy growth function 23
    3.1.3 Optimal initial condition 24
  3.2 Results 24
    3.2.1 Comparison between DNS and linear theory 24

4. Turbulent flow 29
  4.1 Transition 29
  4.2 Fully developed turbulent flow 33
    4.2.1 Variable and constant azimuthal modes 34

5. Conclusions 41

Bibliography 42

Appendix 47

A. Further statistics 49

NOMENCLATURE

Coordinate systems

x	Axial coordinate
r	Radial coordinate
θ	Azimuthal coordinate
u	Axial velocity
v	Radial velocity
w	Azimuthal velocity
y	Wall-normal coordinate $[y = 1 - r]$

Physical quantities

ν	Kinematic viscosity
k	Perturbation energy

Reference quantities

R	Pipe radius
D	Pipe diameter
L	Pipe length
U_c	Centerline mean axial velocity
U_b	Bulk velocity
$U_{c,P}$	Centerline velocity of the discharge equivalent Poiseuille flow
u_τ	Friction velocity
Re_c	Reynolds centerline $\left[\frac{U_c R}{\nu}\right]$

Re_b	Reynolds bulk $\left[\frac{U_b\,D}{\nu}\right]$
Re_P	Reynolds centerline of the discharge equivalent Poiseuille flow $\left[\frac{U_{c,P}\,R}{\nu}\right]$
Re_τ	Reynolds based on friction velocity $\left[\frac{u_\tau\,R}{\nu}\right]$

1. INTRODUCTION

Study of turbulence was born in the early 1870s when Osbourne Reynolds performed his first experiments on transition in pipe flows, [Rey83]. Since then pipe flow has had an uneven role in understanding turbulence: protagonist in first studies, such as Nikuradse experiments on roughness, pipe flow has ever been subjected to a divided attention during the second part of the past century.

A renewed interest

Projects like CICLoPE prove that experimentation on pipe flow is now living matter and testify that this type of flow is a valuable tool to verify commonly accepted theories or better understand open question, e.g. large scale structures and energy transfer in wall-boundend shear flows or objection on universality of von Kármán constant, [TPF$^+$08].

Other fields of interest, in which pipe flow is involved, are investigation upon similar behavior in turbulence structure between pipe, channel and turbulent boundary layers [MHN$^+$06] and development of flow control techniques for cylindrical geometries, such as recent experiments by [ABB$^+$10] on traveling waves.

One strong point of experiments regarding pipes is the lower amount of energy needed: as the pressure drop is smaller than in the channel counterpart, that require a bigger cross section to be considered two-dimensional, pipe facilities need smaller fans and a smaller amount of energy.

Other advantages of pipe flow experiments are that pressure drop along the pipe gives directly the wall mean shear stress and only length-to-radius ratio has to be decided. This feature distinguish pipe from channel, where also spanwise direction has to be set, and is common both to experiments and numerical simulations. In numerical approach, has even a more profound meaning: the periodical condition, that in channel flow case is a consequence of homogeneity hypothesis, in pipe flows is natural.

State of the art

Despite that, first pipe Direct Numerical Simulation by [EUW$^+$94] dates 7 years later than the its channel counterpart by [KMM87], probably due to the numerical difficulties associated to the cylindrical coordinate system.

In following years only a limited number of papers has followed, such as works by [OF97] and [QS00]. All first works has in common the use finite-differences schemes to approximates derivatives along the three coordinate directions: Fourier expansion

	Pipe					Annular pipe
	[EUW+94]	[OF97]	[QS00]	[WM08]	[COMB10]	[QL02]
L	$10R$	$10R$	$20R$	$15R$	$\pi R \dots 20\pi R$	$8\pi(R_o - R_i)$
Re_τ	170	170	170	180, 1142	170, 500	175
	FD2	FD2	FD2	FD2	S	FDC(r) S(x, θ)

Table 1.1: State of the art in pipe flow simulation – FD2: Second order finite-differences, FDC: Compact finite differences, S: Spectral method

along homogeneous directions appeared later with [QL02], where a DNS of a flow in a pipe with annular cross-section is performed and on which the developed program is based.

From Reynolds number point of view, [EUW+94], with its $Re_\tau = 180$, is a benchmark for all following works and it has become a standard value for the validation of a DNS codes. Run on higher values of Reynolds number, leaded to values around 1000, like recent work by [WM08], where scale separation starts to be visible.

As mentioned before, length of the pipe is also a sensible parameter in numerical simulations: a length of $10R$ was used in the beginning of pipe simulation, but more recent papers rose this value, up to $20R$ by [QS00] and $15R$ by [WM08]. Work by [COMB10] tried to give an organic view of the problem, establishing that a sufficient pipe length, in order to have correct statistics, is $8\pi R$.

Azimuthal resolution problem

Both using finite-differences schemes or spectral methods, a peculiar problem, in performing an efficient turbulent pipe flow simulation, has given by spatial resolution in the axis region. Once spatial resolution has been set at the pipe wall by physical considerations, azimuthal resolution grows unboundedly as the pipe axis is approached: this behavior leads to restrictive limitations on time step magnitude, due to stability issues of time integration schemes.

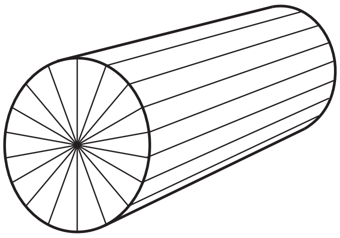

Figure 1.1: Azimuthal resolution issue

The solution implemented in our program is to vary number of azimuthal modes moving towards radial direction, as proposed by [QL02] for pipes with annular cross-section, and more recently by [Boe11] for a conventional pipe. In those works azimuthal modes vanish, taking no account of how they decay approaching the axis.

In this work we will try to consider that applying *reguarity conditions* on modes that vanish in the domain, derived by physical constraints on Fourier coefficients due to cylindrical coordinate system [LB90].

Parallel strategies

In order to raise Reynolds number, a parallelization of computation is needed. Currently a parallel strategy, designed on the architecture of the cluster computer [QL04] that will be used, has been preferred to a conventional MPI-based strategy, that nevertheless would be taken in account for further development of the program.

The idea developed by P. Luchini explits compact support of the numerical scheme used for the approximation of radial derivatives in order to easily split the calculation between different machines, dividing radially the domain into *slices* [LQ06].

One *slice* depends on contiguous ones only by first and last point considered slice. That being so, the amount of communication needed to perform a parallel simulation is very low and permits to use a very simple architecture cluster computer.

2. DIRECT NUMERICAL SIMULATION CODE

This program brings to a further step the process of evolution of the code developed by Luchini an Quadrio, [QL02], for an annular pipe flow, started by P. Luchini himself.

In this chapter a complete description of the DNS code is given. First of all equations, on which the program is based, are introduced and some particular issues with boundary condition will be faced.

Then, we will introduce adopted numerical method and give an overview to critical part of the developed algorithm. At least, strategies used to parallelize the calculus will be approached and evaluated.

2.1 Governing equations

The program is developed on the Fourier transformed Navier-Stokes equation along axial and azimuthal direction, in primitive variables: in this section we describe the derivation of those equations.

Geometry itself brings us to use a cylindrical coordinate system: x, r and θ are axial, radial and azimuthal coordinates, as reported in Figure 2.1, and u, v and w the respective velocities

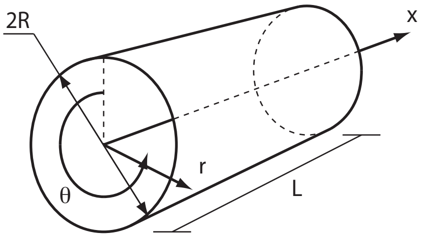

Figure 2.1: Coordinate system

Pipe radius R is taken as the reference length; once a reference velocity U is chosen, a Reynolds Number Re can be defined:

$$Re = \frac{U\,R}{\nu} \tag{2.1}$$

where ν is the kinematic viscosity of the fluid.

The non-dimensional Navier-Stokes equations for an incompressible fluid in cylindrical coordinates can be written as [VO96]:

$$\frac{\partial u}{\partial x}+\frac{1}{r}\frac{\partial\left(rv\right)}{\partial r}+\frac{1}{r}\frac{\partial w}{\partial\theta}=0 \tag{2.2}$$

$$\begin{aligned}\frac{\partial u}{\partial t}+\frac{\partial\left(uu\right)}{\partial x}+\frac{1}{r}\frac{\partial\left(r\,vu\right)}{\partial r}+\frac{1}{r}\frac{\partial\left(wu\right)}{\partial\theta}=-\frac{\partial p}{\partial x}+&\\ +\frac{1}{Re}\left[\frac{\partial^2 u}{\partial x^2}+\frac{1}{r}\frac{\partial}{\partial r}\left(r\frac{\partial u}{\partial r}\right)+\frac{1}{r^2}\frac{\partial^2 u}{\partial\theta^2}\right]&\end{aligned} \tag{2.3}$$

$$\begin{aligned}\frac{\partial\left(rv\right)}{\partial t}+\frac{\partial\left(r\,uv\right)}{\partial x}+\frac{\partial\left(r\,vv\right)}{\partial r}+\frac{\partial\left(wv\right)}{\partial\theta}-ww=-r\frac{\partial p}{\partial r}+&\\ +\frac{1}{Re}\left[\frac{\partial^2\left(rv\right)}{\partial x^2}+r\frac{\partial}{\partial r}\left(r\frac{\partial\left(rv\right)}{\partial r}\right)+\frac{1}{r^2}\frac{\partial^2\left(rv\right)}{\partial\theta^2}-\frac{2}{r}\frac{\partial w}{\partial\theta}\right]&\end{aligned} \tag{2.4}$$

$$\begin{aligned}\frac{\partial w}{\partial t}+\frac{\partial\left(uw\right)}{\partial x}+\frac{1}{r^2}\frac{\partial\left(r^2\,vw\right)}{\partial r}+\frac{1}{r}\frac{\partial\left(ww\right)}{\partial\theta}=-\frac{1}{r}\frac{\partial p}{\partial\theta}+&\\ +\frac{1}{Re}\left[\frac{\partial^2 w}{\partial x^2}+\frac{1}{r}\frac{\partial}{\partial r}\left(r\frac{\partial w}{\partial r}\right)+\frac{1}{r^2}\frac{\partial^2 w}{\partial\theta^2}-\frac{w}{r^2}+\frac{2}{r^3}\frac{\partial rv}{\partial\theta}\right]&\end{aligned} \tag{2.5}$$

To close the differential problem an initial condition and a suitable set of boundary condition are needed: the no-slip condition is imposed at wall and periodic boundary conditions are employed in x direction. Boundary conditions on the axis will be discussed in Section 2.1.2.

2.1.1 Transformed equations

As the flow is naturally periodical along the azimuthal direction and considered so along axial direction, because of the hypothesis of homogeneity along that direction, a truncated Fourier expansion along those two direction is performed, [QL02]. The generic field variable a is now expressed as:

$$a(x,r,\theta,t)=\sum_{i_x}^{+nx}\!\!{}_{-nx}\;\sum_{i_\theta}^{+n_\theta}\!\!{}_{-n_\theta}\;\hat{a}_{i_x,i_\theta}(r,t)\,e^{\mathrm{i}\alpha(i_x)\,x+\mathrm{i}\beta(i_\theta)\,\theta} \tag{2.6}$$

where:

$$\alpha(i_x)=\frac{2\pi\,i_x}{L}=\alpha_0\,i_x;\qquad\beta(i_\theta)=\frac{2\pi\,i_\theta}{2\pi}=\beta_0\,i_\theta=i_\theta.$$

Here i_x and i_θ are integer indices corresponding to the axial and azimuthal directions. α_0 and β_0 are the fundamental wavenumber: because of field natural periodicity along azimuthal direction, β_0 equals to 1.

In order to avoid any division by r, the equations of motion will be multiplied by r^2. Once the axial and azimuthal derivatives had been executed, the resultant equations are:

$$\alpha r\,\hat{u} - \mathcal{D}1\left(r\,\mathrm{i}\hat{v}\right) + \beta\,\hat{w} = 0 \tag{2.7}$$

$$\begin{aligned} r^2\frac{\partial \hat{u}}{\partial t} + \mathrm{i}\alpha r^2\,\widehat{uu} + \mathcal{D}1\left(r^2\,\widehat{uv}\right) - r\,\widehat{uv} + \mathrm{i}\beta r\,\widehat{uw} = -\alpha r^2\,\mathrm{i}\hat{p} + \\ + \frac{1}{Re}\left[\mathcal{D}_*\left(\hat{u}\right) - \left(\alpha^2 r^2 + \beta^2\right)\,\hat{u}\right] \end{aligned} \tag{2.8}$$

$$\begin{aligned} r^2\frac{\partial \hat{v}}{\partial t} + \mathrm{i}\alpha r^2\,\widehat{uv} + \mathcal{D}1\left(r^2\,\widehat{vv}\right) - r\,\widehat{vv} + \mathrm{i}\beta r\,\widehat{vw} - r\,\widehat{ww} = -\mathcal{D}1\left(r^2\,\hat{p}\right) + 2r\,\hat{p} + \\ + \frac{1}{Re}\left[\mathcal{D}_*\left(\hat{v}\right) - \left(\alpha^2 r^2 + \beta^2 + 1\right)\,\hat{v} - 2\mathrm{i}\beta\,\hat{w}\right] \end{aligned} \tag{2.9}$$

$$\begin{aligned} r^2\frac{\partial \hat{w}}{\partial t} + \mathrm{i}\alpha r^2\,\widehat{uw} + \mathcal{D}1\left(r^2\,\widehat{vw}\right) + \mathrm{i}\beta r\,\widehat{ww} = -\beta r\,\mathrm{i}\hat{p} + \\ + \frac{1}{Re}\left[\mathcal{D}_*\left(\hat{w}\right) - \left(\alpha^2 r^2 + \beta^2 + 1\right)\,\hat{w} + 2\beta\,\mathrm{i}\hat{v}\right] \end{aligned} \tag{2.10}$$

where $\mathcal{D}1$ denotes the first derivative in radial direction and $\mathcal{D}_*(\cdot)$ the second derivative $r\frac{\partial}{\partial r}\left(r\frac{\partial(\cdot)}{\partial r}\right)$.

Momentum equations are composed by a viscous linear term and a convective non-linear term. That being so, momentum equation can be rewritten as:

$$r^2\frac{\partial \hat{u}}{\partial t} = \mathcal{C}_u + \mathcal{V}_u \tag{2.11}$$

$$r^2\frac{\partial \hat{v}}{\partial t} = \mathcal{C}_v + \mathcal{V}_v \tag{2.12}$$

$$r^2\frac{\partial \hat{w}}{\partial t} = \mathcal{C}_w + \mathcal{V}_w \tag{2.13}$$

where the viscous and convective terms have been collapsed in:

$$\mathcal{C}_u = -\mathrm{i}\alpha r^2\,\widehat{uu} - \mathcal{D}1\left(r^2\,\widehat{uv}\right) + r\,\widehat{uv} - \mathrm{i}\beta r\,\widehat{uw} \tag{2.14}$$

$$\mathcal{C}_v = -\mathrm{i}\alpha r^2\,\widehat{uv} - \mathcal{D}1\left(r^2\,\widehat{vv}\right) + r\,\widehat{vv} - \mathrm{i}\beta r\,\widehat{vw} + r\,\widehat{ww} \tag{2.15}$$

$$\mathcal{C}_w = -\mathrm{i}\alpha r^2\,\widehat{uw} - \mathcal{D}1\left(r^2\,\widehat{vw}\right) - \mathrm{i}\beta r\,\widehat{ww} \tag{2.16}$$

$$\mathcal{V}_u = \frac{1}{Re}\left[\mathcal{D}_*\left(\hat{u}\right) - \left(\alpha^2 r^2 + \beta^2\right)\,\hat{u}\right] - \alpha r^2\,\mathrm{i}\hat{p} \tag{2.17}$$

$$\mathcal{V}_v = \frac{1}{Re}\left[\mathcal{D}_*\left(\hat{v}\right) - \left(\alpha^2 r^2 + \beta^2 + 1\right)\,\hat{v} - 2\mathrm{i}\beta\,\hat{w}\right] - \mathcal{D}1\left(r^2\,\hat{p}\right) + 2r\,\hat{p} \tag{2.18}$$

$$\mathcal{V}_w = \frac{1}{Re}\left[\mathcal{D}_*\left(\hat{w}\right) - \left(\alpha^2 r^2 + \beta^2 + 1\right)\,\hat{w} + 2\beta\,\mathrm{i}\hat{v}\right] - \beta r\,\mathrm{i}\hat{p} \tag{2.19}$$

This notation will be useful when the time integration method will be introduced.

Now we have a set of equations for each mode, where coupling is due to the non linear therm $\mathcal{C}$ only. Navier Stokes equation will be solved in interior points only: at the wall, the no slip condition is imposed. At the axis the solution is found by regularity condition.

2.1.2 Regularity conditions

Using a Fourier expansion set us on some considerations about the behavior of Fourier coefficients approaching the axis. These coefficients express both scalar quantities, i.e. pressure, and vectorial quantities, so a separete treatment is needed [LB90].

For pressure, assumption that each coefficient is a regular function of the space, leads to

$$\hat{p}(r) \sim r^{|\beta|} \quad \text{as } r \to 0. \tag{2.20}$$

A similar approach enables us to set the conditions on the three components of velocity vector. For $\beta \neq 0$, the derived conditions are

$$\left.\begin{array}{l} \hat{u}(r) \sim r^{|\beta|} \\ \hat{v}(r) \sim r^{|\beta|-1} \\ \hat{w}(r) \sim r^{|\beta|-1} \end{array}\right\} \quad \text{as } r \to 0 \tag{2.21}$$

while, for $\beta = 0$,

$$\left.\begin{array}{l} \hat{u}(r) \sim r^{0} \\ \hat{v}(r) \sim r \\ \hat{w}(r) \sim r \end{array}\right\} \quad \text{as } r \to 0. \tag{2.22}$$

Note that the behavior of axial components u is the same of the scalar p, predictable result because x coordinate does not takes part in the transformation between cartesian coordinates and cylindrical ones.

Considerations that have been made in this section will be useful when azimuthal variable modes will be introduced. Differently to other DNS codes found in literature, that just set to zero cut off modes, our implementation of this feature takes into account how they decay approaching the axis: in order to consider that, regularity conditions will be used as boundary conditions for modes that vanish in domain. This treatment in implementing variable modes is expected to better approximate modes trend, and so energy spectra, than former works.

2.2 Numerical methods

2.2.1 Time integration scheme

Time integration of the equations is performed by a partially implicit method, described in [RM91]: an explicit methods is used for nonlinear convective terms and an implicit methods for linear viscous ones.

Once the following notation is introduced

$$\boldsymbol{u} = \begin{bmatrix} \hat{u} \\ \hat{v} \\ \hat{w} \end{bmatrix} \qquad \mathcal{N}(\boldsymbol{u}) = \begin{bmatrix} \mathcal{C}_u \\ \mathcal{C}_v \\ \mathcal{C}_w \end{bmatrix} \qquad \mathcal{V}(\boldsymbol{u}, p) = \begin{bmatrix} \mathcal{V}_u \\ \mathcal{V}_v \\ \mathcal{V}_w \end{bmatrix} \tag{2.23}$$

time integration scheme can be written as

$$r^2\boldsymbol{u}_a = r^2\boldsymbol{u}_n + \Delta t\left[\alpha_1\left(\mathcal{V}(\boldsymbol{u}_n, p_n) + \mathcal{V}(\boldsymbol{u}_a, p_a)\right) + \gamma_1\mathcal{N}(\boldsymbol{u}_n)\right] \tag{2.24}$$

$$r^2\boldsymbol{u}_b = r^2\boldsymbol{u}_a + \Delta t\left[\alpha_2\left(\mathcal{V}(\boldsymbol{u}_a, p_a) + \mathcal{V}(\boldsymbol{u}_b, p_b)\right) + \gamma_2\mathcal{N}(\boldsymbol{u}_a) + \zeta_1\mathcal{N}(\boldsymbol{u}_n)\right] \tag{2.25}$$

$$r^2\boldsymbol{u}_{n+1} = r^2\boldsymbol{u}_b + \Delta t\left[\alpha_3\left(\mathcal{V}(\boldsymbol{u}_b, p_b) + \mathcal{V}(\boldsymbol{u}_{n+1}, p_{n+1})\right) + \gamma_3\mathcal{N}(\boldsymbol{u}_b) + \zeta_2\mathcal{N}(\boldsymbol{u}_a)\right] \tag{2.26}$$

with:

$$\begin{aligned} \alpha_1 &= \frac{4}{15} & \gamma_1 &= \frac{8}{15} & & \\ \alpha_2 &= \frac{1}{15} & \gamma_2 &= \frac{5}{12} & \zeta_1 &= -\frac{17}{60} \\ \alpha_3 &= \frac{1}{6} & \gamma_3 &= \frac{3}{4} & \zeta_2 &= -\frac{5}{12}. \end{aligned}$$

The method seen before takes no consideration of continuity condition. In order to introduce the continuity equation, we set this notation:

$$\boldsymbol{x} = \begin{bmatrix} \hat{p} \\ \hat{u} \\ \hat{v} \\ \hat{w} \end{bmatrix} \qquad \mathbf{c} = \begin{bmatrix} 0 \\ \alpha r \\ -\mathcal{D}1\, r \\ \beta \end{bmatrix} \qquad \mathbf{L} = \begin{bmatrix} \partial_p\mathcal{V}_u & \partial_u\mathcal{V}_u & \partial_v\mathcal{V}_u & \partial_w\mathcal{V}_u \\ \partial_p\mathcal{V}_v & \partial_u\mathcal{V}_v & \partial_v\mathcal{V}_v & \partial_w\mathcal{V}_v \\ \partial_p\mathcal{V}_w & \partial_u\mathcal{V}_w & \partial_v\mathcal{V}_w & \partial_w\mathcal{V}_w \end{bmatrix} \tag{2.27}$$

Now it is possible to write the closed system that let us to calculate the substep solution x_{s+1}, given x_s, where s is the substep index:

$$\begin{aligned} &\begin{bmatrix} \mathbf{c}^T \\ \left(r^2 - \Delta t\alpha_s\right)\mathbf{L} \end{bmatrix} \boldsymbol{x}_{s+1} = \\ &\qquad = \begin{bmatrix} 0 \\ r^2\boldsymbol{u}_s \end{bmatrix} + \begin{bmatrix} 0 \\ \Delta t\ \left(\alpha_s\,\mathcal{V}(\boldsymbol{u}_s, p_s) + \gamma_2\mathcal{N}(\boldsymbol{u}_s) + \zeta_1\mathcal{N}(\boldsymbol{u}_{s-1})\right) \end{bmatrix} \end{aligned} \tag{2.28}$$

This scheme is implemented in such a way to reduce the memory requirements to a minimum: for each substep the program needs to store only three vectors: current step right-hand-side, previous step state and previous step right-hand-side. Linear system solution needs no further vectors because it is performed in place on the right-hand-side stored memory.

2.2.2 Radial derivatives

The discretization of radial derivatives is performed through finite-differences compact scheme over a molecule composed by three arbitrary spaced grid points, [Lel92].

$$\mathcal{D}n\left(f\left(r_i\right)\right) \approx \mathrm{D}n\left(f\left(r_i\right)\right) = \overset{1}{\underset{-1}{\sum\nolimits_j}} d_n^j(i)\, f\left(r_{j+i}\right) \tag{2.29}$$

Compact schemes are also known as implicit finite-differences, because they typically require the inversion of a linear system for the calculation of the derivative. In this particular case it is possible to avoid that inversion introducing a zero-derivative operator D0.

Following a standard procedure in the theory of Padé approximants, the first derivative for i position is obtained by solving the linear system:

$$\underset{-1}{\overset{1}{\sum_j}} d_1^j(i)\ (r_{j+i}-r_i)^m = \mathcal{D}1\left((r_{j+i}-r_i)^m\right) \qquad \text{for } \ m = 0\ldots 2. \tag{2.30}$$

Imposing that

$$\underset{-1}{\overset{1}{\sum_j}} d_0^j(i)\,\mathcal{D}1\left((r_{j+i}-r_i)^{m+1}\right) = \underset{-1}{\overset{1}{\sum_j}} d_1^j(i)\ (r_{j+i}-r_i)^{m+1} \qquad \text{for } \ m = 1\ldots 3 \tag{2.31}$$

we obtain the zero-derivative coefficients $d_0^j(i)$. The remaining derivative is, finally, calculated by solving

$$\underset{-1}{\overset{1}{\sum_j}} d_*^j(i)\ (r_{j+i}-r_i)^m = \underset{-1}{\overset{1}{\sum_j}} d_0^j(i)\mathcal{D}_*\left((r_{j+i}-r_i)^m\right) \qquad \text{for } \ m = 0\ldots 2. \tag{2.32}$$

Order of accuracy of finite-differences schemes has been investigated. Discrete derivates obtained by applying compact schemes to sine function, has been compared to algebraic values, defining

$$\mathrm{err}_1(r) = \mathrm{D1}\left(\sin(r)\right) - \mathrm{D0}\left(\cos(r)\right) \tag{2.33}$$

$$\mathrm{err}_*(r) = \mathrm{D}_*\left(\sin(r)\right) - \mathrm{D0}\left(r\cos(r) - r^2\sin(r)\right) \tag{2.34}$$

As we can from Figure 2.2, D1 and D$_*$ operator present respectively a forth-order and a second-order accuracy.

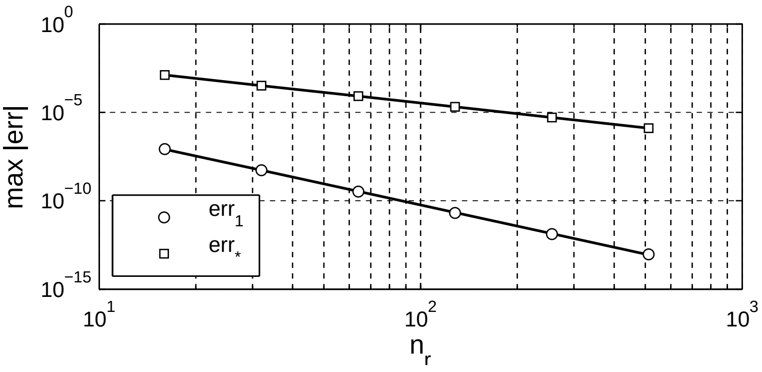

Figure 2.2: Finite-differences accuracy

Radial grid spacing

Law used to generate the radial grid is

$$r_i = \begin{cases} \dfrac{1}{\tanh\left(c_{th}\right)} \tanh\left(c_{th}\dfrac{i}{n_r}\right) & \text{if} \quad c_{th} > 0 \\ \dfrac{i}{n_r} & \text{if} \quad c_{th} = 0 \end{cases} \tag{2.35}$$

This law provide a knob parameter c_{th}, that permits to adjust grid spacing, loosing near axis and refining near wall, as shown in Figure 2.3.

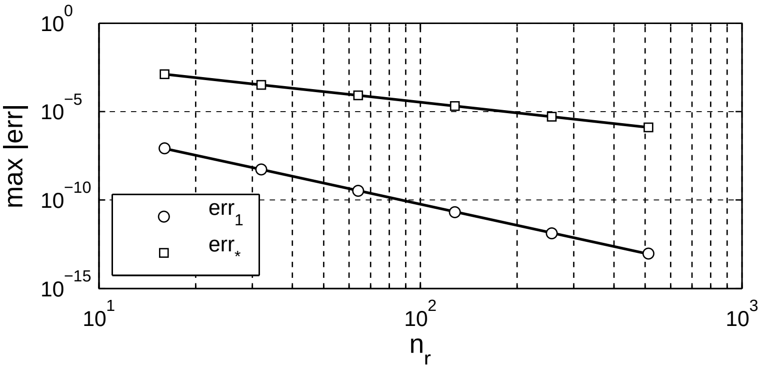

Figure 2.3: Finite-differences accuracy

2.2.3 Spatial resolution in the azimuthal direction

An intrinsic issue of cylindrical coordinates is that the azimuthal spatial resolution increase when approaching the axis, as n_θ is constant. This behavior has two undesired effects: first, the region near the axis has an over resolution along azimuthal direction and, second, the local CFL number increases in that area. This last consequence poses serious stability limitations on time-step: as we are going to see in Section 4.2.1, time step allowed for a constant distribution of azimuthal modes is dominated by local CFL near the axis.

To overcome those problems, the truncation of the azimuthal Fourier series has been made a function of the radial position. The expansion introduced with Eq. (2.6) will be replaced by

$$a(x,r,\theta,t) = \sum_{i_x}{}_{-nx}^{+nx} \sum_{i_\theta}{}_{-n_\theta(r)}^{+n_\theta(r)} \hat{a}_{i_x,i_\theta}(r,t)\, e^{\mathrm{i}\alpha(i_x)\,x+\mathrm{i}\beta(i_\theta)\,\theta}. \tag{2.36}$$

where $n_\theta(r)$ can be an arbitrary function of radial position.

In reducing the number of azimuthal modes, some constraints have to be considered: as highlighted by Lewis and Bellan in [LB90], we can see from Eq. (2.22) that the modes with $\beta = 1$ have a relevant importance because only those mode can have $\hat{v}$

and $\hat{w}$ finite at $r = 0$. Taking this into account, any distribution $n_\theta(r)$ should include modes with $\beta = 1$ on the axis.

A first attempt at define a proper azimuthal modes distribution has been made: the implemented $n_\theta(r)$ law set a linear variation of the number of azimuthal modes in order to maintain the spatial resolution $l_\theta = \frac{2\pi\, r}{2\, n_\theta(r)}$ as constant as possible along the radial direction, Figure 2.4.

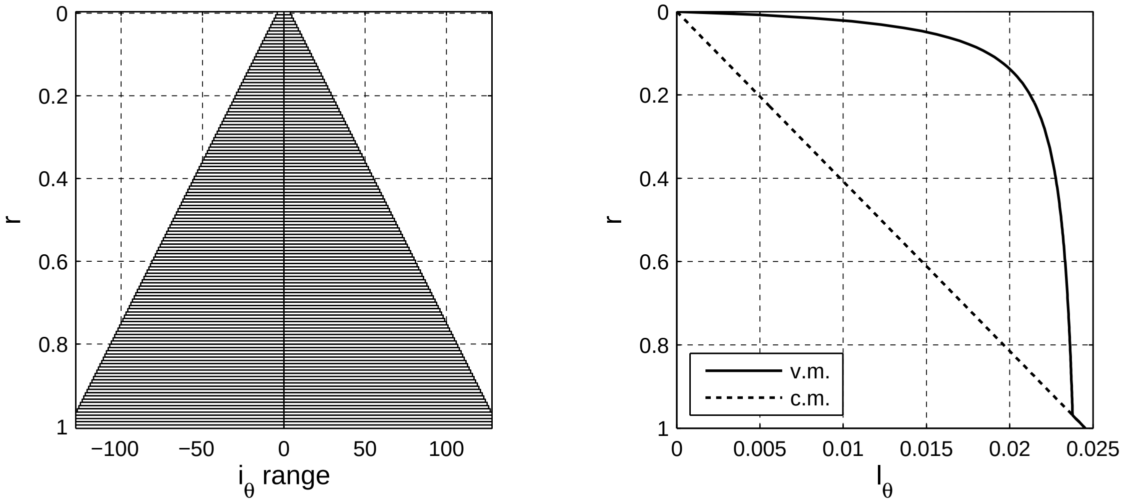

Figure 2.4: Radial distribution of azimuthal modes $-$ $n_r = 128$, $n_\theta = 128$, $c_{th} = 0$

This distribution has only geometric foundations and, probably, would not be optimal. A better evaluation of number of modes needed could be based on comparison of velocity power spectra between constant modes and variable modes. This should give a more accurate idea of which modes are involved for each radial station.

Values of flow quantities for the first radial station where a mode appear, are obtained applying regularity conditions, Section 2.1.2. Because of that and because of length of finite-difference molecula, a mode have to appear at least in 3 contiguous radial positions.

The discrete form of regularity conditions can be written as:

$$\hat{p}_{\alpha,\beta}\left(r_{i_{y0,\beta}}\right) + \overset{2}{\underset{1}{\sum\nolimits_j}} bc_0^j(\beta)\, \hat{p}_{\alpha,\beta}\left(r_{i_{y0,\beta}+j}\right) = 0 \tag{2.37}$$

$$\hat{u}_{\alpha,\beta}\left(r_{i_{y0,\beta}}\right) + \overset{2}{\underset{1}{\sum\nolimits_j}} bc_0^j(\beta)\, \hat{u}_{\alpha,\beta}\left(r_{i_{y0,\beta}+j}\right) = 0 \tag{2.38}$$

$$\hat{v}_{\alpha,\beta}\left(r_{i_{y0,\beta}}\right) + \overset{2}{\underset{1}{\sum\nolimits_j}} bc_1^j(\beta)\, \hat{v}_{\alpha,\beta}\left(r_{i_{y0,\beta}+j}\right) = 0 \tag{2.39}$$

$$\hat{w}_{\alpha,\beta}\left(r_{i_{y0,\beta}}\right) + \overset{2}{\underset{1}{\sum\nolimits_j}} bc_1^j(\beta)\, \hat{w}_{\alpha,\beta}\left(r_{i_{y0,\beta}+j}\right) = 0 \tag{2.40}$$

where $i_{y0,\beta}$ is the radial index where modes β appear. Coefficients $bc_s^j(\beta)$ are obtained by imposing, discretely, regularity conditions: hence, coefficients are calculated by solving the system:

$$\left(r_{i_{y0,\beta}}\right)^{|\beta|+2m-s} + \sum_{0}^{2}{}_{j}\, bc_s^j(\beta)\ \left(r_{i_{y0,\beta+j}}\right)^{|\beta|+2m-s} = 0 \qquad \text{for } \ m = 1\ldots 2. \tag{2.41}$$

A special treatment is needed for $bc_1^j(0)$, the regularity condition applied to $\hat{v}_{\alpha,0}$ and $\hat{w}_{\alpha,0}$. Their values is given by

$$\left(r_{i_{y0,0}}\right)^{2m+1} + \sum_{0}^{2}{}_{j}\, bc_1^j(0)\ \left(r_{i_{y0,0+j}}\right)^{2m+1} = 0 \qquad \text{for } \ m = 1\ldots 2. \tag{2.42}$$

2.3 Algorithm

The program is written using CPL, a programming language with related compiler conceived by Paolo Luchini, [QL04]. CPL source is subjected first to a preprocessing pass to generate an ANSI-C source, which is then compiled by any ANSI-compliant C compiler. The meaning of CPL statements, keyword and programming structures can be easily understood, since they are modeled after the most common programming languages.

A strong point of this programming language, particularly useful in developing this program, is the easy comb array management: variable modes need a comb array of Fourier coefficients whose number varies radially that is simply and efficiently implemented in the program, as we can see from the extract of the program reported below.

```
VELOCITY=STRUCTURED ARRAY(u,v,w) OF COMPLEX
SHARED ARRAY(0..nx,-nz..nz) OF POINTER TO ARRAY(*) OF VELOCITY V
LOOP FOR ALL ix,m
  IF iy0(m)>nyh THEN V(ix,m)=NULL ELSE
    V(ix,m)=NEW SHARED ARRAY(MAX(iy0(m),nyl-1)..nyh+1) OF VELOCITY
  END IF
REPEAT
```

Another useful feature are the implicit limits in flow control statements, that permit to reduce the number of command lines and make easier to read the program source. Here an example in calculating perturbation energy for each radial position:

```
LOOP FOR iy=MAX(0,nyl-1) TO MIN(ny-1,nyh)
  LOOP FOR ALL ix,iz EXCEPT (ix=0 AND iz=0) OR iy<iy0(iz) WITH V(ix,iz,iy)
    slice\_en(iy) = ~ + 1/2 * [NORM(u)+NORM(v)+NORM(w)]*[IF ix=0 THEN 1 ELSE 2]
  REPEAT
REPEAT
```

As we can see, upper and lower limits of first and second index of variable `V`, are automatically detected.

2.3.1 Computing convolutions

Evaluation of convective term $\mathcal{C}$, that is performed in function `buildrhs`, needs to compute six convolution in order to evaluate $\widehat{uu}$, $\widehat{vv}$, $\widehat{ww}$, $\widehat{uv}$, $\widehat{uw}$ and $\widehat{vw}$.

Computational cost of a direct convolution in Fourier space goes with $n_x^2\,n_\theta^2$. However, a standard procedure that permits to compute convolutions in a faster way is used: thanks to convolution theorem and Fast Fourier Transform (FFT), the computational cost can be reduced to $\mathcal{O}\left(n_x n_\theta\,\log\left(n_x n_\theta\right)\right)$.

Convolution theorem

The convolution theorem states that the Fourier transform of a convolution is the pointwise product of Fourier transforms. This theorem suggests us to calculate the convolution as a product in physical space and then transform back in Fourier space.

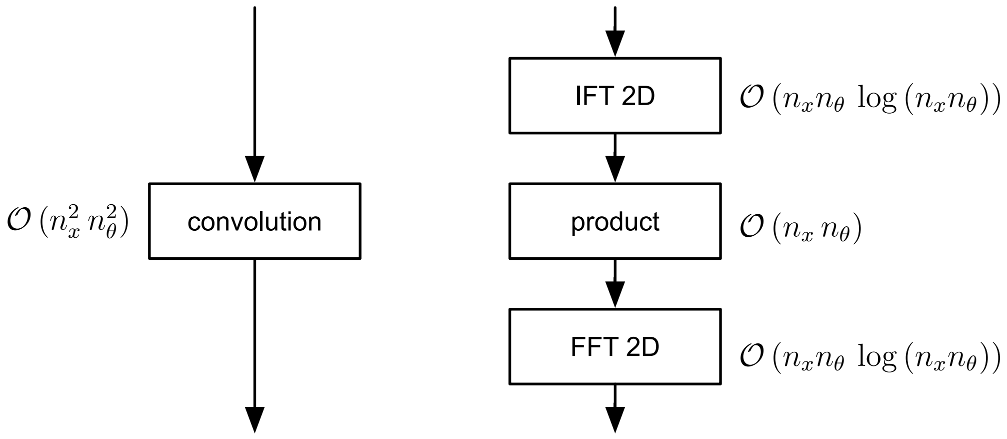
$\mathcal{O}\left(n_x^2\,n_\theta^2\right)$
convolution
IFT 2D
$\mathcal{O}\left(n_x n_\theta\,\log\left(n_x n_\theta\right)\right)$
product
$\mathcal{O}\left(n_x\,n_\theta\right)$
FFT 2D
$\mathcal{O}\left(n_x n_\theta\,\log\left(n_x n_\theta\right)\right)$

(a) Conventional convolution (b) Pseudospectral convolution

Figure 2.5: Computational cost

Thanks to FFT algorithm, computational cost of the whole operation is dominated by the cost of FFT itself: so cost of whole operation goes with $\mathcal{O}\left(n_x n_\theta\,\log\left(n_x n_\theta\right)\right)$, instead of $n_x^2\,n_\theta^2$ of the conventional one. This approach is called pseudospectral convolution.

Fast Fourier Transform (FFT)

Fast Fourier Transform has some constraints about the number of point processed: CPL built-in algorithm needs number of point in each direction to be a product of a power of 2 and possibly a factor of 3.

In the light of those consideration, the number of points in axial direction will be expanded, during the convolution evaluation, to $n_{x,d}$ and must satisfy:

$$n_{x,d} \mod 2 = 0 \quad \wedge \quad n_{x,d} \geq \frac{3}{2} n_x \tag{2.43}$$

Similarly, $n_{\theta,d}(i_r)$ has to be

$$n_{\theta,d}(i_r) \mod 2 = 0 \quad \wedge \quad n_{\theta,d}(i_r) \geq 3\, n_\theta \tag{2.44}$$

Note that $n_{\theta,d}(i_r)$ is a function of radial position because of the introduction of variable azimuthal modes.

A reduction of stored memory is possible considering that quantities in physical space are expressed by real numbers. Under this hypothesis, imaginary part is odd respect spatial frequency: because of this we can store the positive frequency plan only, for a one-dimension FFT. In two-dimension case, only one index can be reduced, in our case the axial one.

2.3.2 Time step

The program can work with both a fixed and variable time step Δt. The condition used for the estimation of a proper Δt is standard condition on CFL number. In order to do that, variable $\chi(i_r)$ is defined as:

$$\chi(i_r) = \max_{i_x, i_\theta}\left(\frac{|u|}{\Delta x}\right) + \max_{i_x, i_\theta}\left(\frac{|v|}{\Delta r}\right) + \max_{i_x, i_\theta}\left(\frac{|w|}{r\Delta\theta}\right) \tag{2.45}$$

where $\Delta x = \frac{L}{n_{x,d}}$ and $\Delta\theta = \frac{2\pi}{n_{\theta,d}(i_r)}$. Its evaluation, made in physical space, is performed during the first step of the time integration scheme where the convolution are calculated.

Once $\chi(i_r)$ is known for all radial station, the program sets Δt, that will be used in next iteration, as:

$$\Delta t = \frac{\mathrm{cfl}_{\max}}{\max\limits_{i_r}\left(\chi_{i_r}\right)}. \tag{2.46}$$

where $\mathrm{cfl}_{\max}$ is chosen by the user.

2.3.3 Files format

Simulation parameters file

This file sets up all parameters needed to perform a simulation and it must be named `cyl.in`. They are, in order:

- $\mathbf{n_x}, \mathbf{n_r}, \mathbf{n_\theta}$: number of axial and azimuthal modes and number of radial points;
- $\alpha_\mathbf{0}$: axial fundamental wavenumber;

- **Re**: Reynolds number;
- $\mathbf{Q}/2\pi$ or $\langle\partial_\mathbf{x}\mathbf{p}\rangle$: imposed mean axial flow or mean axial pressure gradient;
- $\boldsymbol{\Delta}\mathbf{t}$ or $\mathbf{cfl}_{\max}$: imposed constant or variable time step;
- $\mathbf{t}_{\max}$: final simulation time;
- $\boldsymbol{\Delta}\mathbf{t}_{\mathbf{field}}$: time interval at which a file containing current field is written;
- $\boldsymbol{\Delta}\mathbf{t}_{\mathbf{plot}}$: time interval at which mean flow profile is visualized using a `gnuplot`-based function;
- **input file**: name of the field file to be used as initial condition, if not specified a laminar flow with no disturbances is assumed.

Runtime file

During a simulation, a runtime file, containing some of peculiar flow quantities, is generated. A new line is written for each time step and its structure is described in Table 2.1.

time	$\partial_r\hat{u}_{0,0}(1,t)$	$\hat{u}_{0,0}(0,t)$	Q	$\max\limits_{i_r}(\chi_{i_r})$	$k(t)$	Δt
`0`	`2`	`1`	`0.25`	`0`	`19.2`	`0.0520834`
`0.0520834`	`2`	`1`	`0.25`	`0`	`19.2`	`0.0520834`
`0.104167`	`2`	`1`	`0.25`	`0`	`19.2`	`0.0520834`
...						

Table 2.1: Runtime file structure

Field file

The file where a field is stored is composed by a 1024 byte ASCII header, where some of `cyl.in` parameters are reported, and a binary part, which contains in order:

- radial nodes array;
- an array containing, for non negative azimuthal wavenumber, the index of first radial position where the wavenumber is considered;
- field file written by radial index, axial index and azimuthal index.

2.4 Parallel strategies

In order to parallelize the calculation, two complementary parallel strategies have been delineated. The firs one uses a group of distribuited-memory machines to radially divide the domain between nodes; the second one is an SMP strategy exploits shared memory configurations.

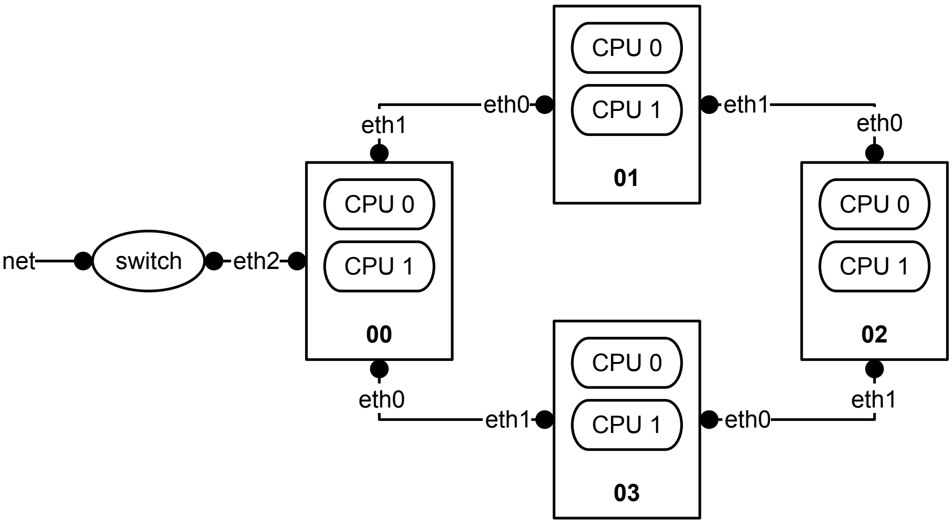

Figure 2.6: Cluster architecure

In Figure 2.6 a typical architecture, for which those strategies has been developed, it is shown.

Distribuited-memory machines

The domain is divided between n_p nodes: a radial slice, from $n_{r,l\,i_p}$ to $n_{r,h\,i_p}$ radial position, is assigned to each node.

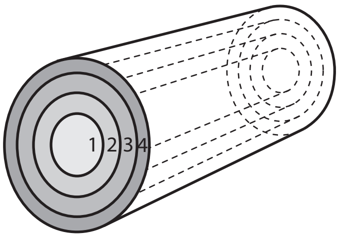

Figure 2.7: Radial partition

In dividing domain into slices, it is necessary to be careful with balancing computational load between nodes: if load is not equally divided, because all machines have to be synchronized during the simulation, the simulation speed will be the one of the slowest process.

In case of a constant azimuthal modes distribution, the optimal load distribution concurs with an equipartition of radial position between slides, because every $x\theta$-plane costs computationally the same as all other ones. It is different if variable modes are used: because of the variation of n_θ, and hence $n_{\theta,d}$, between radial position, computational cost varies with it.

A first and very preliminary attempt to balance computational load between nodes has been made. The idea is to predict the computational cost of each slice as a function of some simulation parameters. The function defined below, $W_{LB}(i_r)$, express the cumulative computational cost for each slice: that estimation is based on the computational cost of the two-dimension FFT, function that should take most of the computational time.

$$W_{LB}(i_r) = \sum_{n_{r,l\,i_p}}^{i_r}{}_{j_r} n_{x,d}\, n_{\theta,d}(j_r) \ \left[\ln\left(n_{x,d}\right) + \ln\left(n_{\theta,d}(j_r)\right)\right] \tag{2.47}$$

W_{LB} is defined in order to dimensions the various $W_{LB}(n_{r,h\,i_p})$ as computational cost estimation of i_p slice.

A simple algorithm sizes slices in order to get a computational cost partitioned as equal as possible between slices. In Figure 2.8, an attempt of load-balancing is shown.

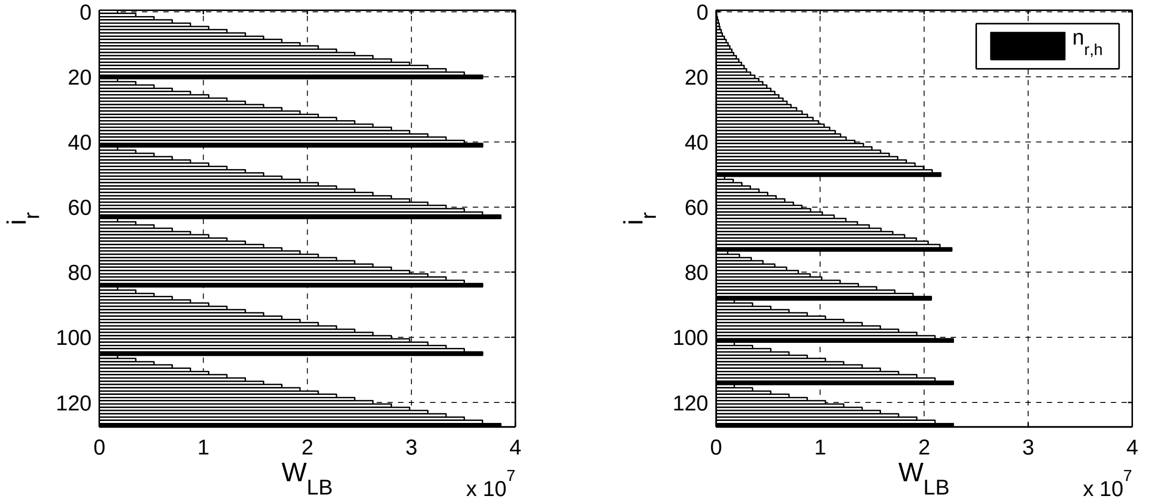

(a) constant modes

(b) variable modes

Figure 2.8: Load-balancing weight function − $n_x = 256$, $n_r = 128$, $n_\theta = 128$, $n_p = 6$

Parallel communication procedure is a development of the one used in [LQ06]: in this former work, duplication of two first and last points of each slice was necessary, limiting parallel performances. In this program, instead, this procedure has been written by P. Luchini with no need of duplications along radial direction in order to enhance parallel performances.

Symmetric MultiProcessing (SMP)

On each node, two-dimensional FFT can be parallelized: for each radial station $n_{x,d}$ stripes are divided between between the n_{SMP} CPUs on the node, and then the same with azimuthal direction. That is obtained by ”forking” new processes which read from and write to the same memory space; those are handled by the operating system itself, which assign one task to each CPU.

2.4.1 Parallel performances

Useful parameters for evaluating parallel performances are speedup factor S and parallel efficiency E:

$$S(n_p) = \frac{T_{n_p}}{T_1} \qquad E(n_p) = \frac{S(n_p)}{n_p} \tag{2.48}$$

where T_{n_p} is the simulation time using n_p machines.

Thanks to the optimized communication procedure ideated by P. Luchini, the ideal speedup factor S_i is equal to number of computational nodes with a unitary parallel efficiency:

$$S_i(n_p) = n_p \qquad E_i(n_p) = 1. \tag{2.49}$$

Some tests have been made on a system composed by ten AMD Opteron quad-core 800MHz CPUs, connected each other by GigabitLAN cards. The developed program was capable, on 10 machines, of a speedup factor of almost 7.5 for a simulation, where 1025 axial, 513 azimuthal modes and 201 radial points have been considered.

These performances are expected to raise as Reynolds, and so problem size, increases: bottleneck of this system is communication speed and, as the problem gets bigger, communications between nodes are going to take a smaller part of run-time. Helpful would be also a finer tuning of power-balancing procedure, that has been treated in a preliminary way only.

3. OPTIMAL ENERGY GROWTH

The study of optimal energy density growth has two goals: on one side, it would be useful as a first step on the validation of the developed program and, on the other hand, it will provide a initial field useful to generate a fully turbulent flow.

Reference for this part of the work will be the paper by Shmid and Henningson [SH94].

3.1 Theoretical background

First of all, it is introduced the theory that leads to the energy growth function and the optimal initial condition. As before, due to domain's geometry, it is useful to adopt a cylindrical coordinate system: x, r, θ indicate axial, radial and azimuthal direction and u, v, w the respective velocities.

3.1.1 Governing equations

Starting point for this analysis are the *linearized* Navier-Stokes equations, where an axial mean flow of the form $U(r)$ has been assumed:

$$\frac{\partial u}{\partial x} + \frac{1}{r}\frac{\partial}{\partial r}(rv) + \frac{1}{r}\frac{\partial w}{\partial \theta} = 0 \tag{3.1}$$

$$\frac{\partial u}{\partial t} + U\frac{\partial u}{\partial x} + vU' = -\frac{\partial p}{\partial x} + \frac{1}{Re_c}\left[\frac{1}{r}\frac{\partial}{\partial r}\left(\frac{\partial u}{\partial r}\right) + \frac{1}{r^2}\frac{\partial^2 u}{\partial \theta^2} + \frac{\partial^2 u}{\partial \theta^2}\right] \tag{3.2}$$

$$\frac{\partial v}{\partial t} + U\frac{\partial v}{\partial x} = -\frac{\partial p}{\partial r} + \frac{1}{Re_c}\left[\frac{1}{r}\frac{\partial}{\partial r}\left(\frac{\partial v}{\partial r}\right) + \frac{1}{r^2}\frac{\partial^2 u}{\partial \theta^2} + \frac{\partial^2 u}{\partial \theta^2} - \frac{v}{r^2} - \frac{2}{r^2}\frac{\partial w}{\partial \theta}\right] \tag{3.3}$$

$$\frac{\partial w}{\partial t} + U\frac{\partial w}{\partial x} = -\frac{1}{r}\frac{\partial p}{\partial \theta} + \frac{1}{Re_c}\left[\frac{1}{r}\frac{\partial}{\partial r}\left(\frac{\partial v}{\partial r}\right) + \frac{1}{r^2}\frac{\partial^2 u}{\partial \theta^2} + \frac{\partial^2 u}{\partial \theta^2} + \frac{w}{r^2} - \frac{2}{r^2}\frac{\partial v}{\partial \theta}\right] \tag{3.4}$$

Those equations have been non-dimensionalized by the pipe radius R and the center-line velocity U_c. As a result, Reynolds number Re_c is defined as $\frac{RU_{cl}}{\nu}$, where ν is the kinematic viscosity.

Flow is periodic on the azimuthal direction and, for this study, will be considered also periodic on axial direction: this assumption leads to express all the flow properties as:

$$\begin{bmatrix} u \\ v \\ w \\ p \end{bmatrix} = \sum_{\alpha,\,\beta} e^{(\mathrm{i}\alpha x + \mathrm{i}\beta\theta)} \begin{bmatrix} \hat{u} \\ \hat{v} \\ \hat{w} \\ \hat{p} \end{bmatrix} \tag{3.5}$$

where $\alpha \in \mathbb{R}$, $\beta \in \mathbb{Z}$ and $[\hat{u}, \hat{v}, \hat{w}, \hat{p}]^T \in \mathbb{C}$.

In order to transform an algebraic-differential problem, as the Navier-Stokes equations, in an evolutive only problem, the radial velocity($\hat{v}$)-radial vorticity($\hat{\eta}$) formulation is introduced. Defining the new variables

$$\hat{\boldsymbol{\phi}} = -\mathrm{i} r v \qquad \hat{\boldsymbol{\omega}} = \frac{\alpha r \hat{w} - \beta \hat{u}}{\beta k^2 Re_c\, r^2} = \frac{\hat{\eta}}{\mathrm{i} \beta k^2 Re_c\, r}, \tag{3.6}$$

the obtained equations are:

$$\left(Re_c \frac{\partial}{\partial t} + \mathrm{i}\alpha Re_c U\right) \mathcal{T}\, \hat{\boldsymbol{\phi}} - \frac{\mathrm{i}\alpha Re_c}{r} \left(\frac{U'}{k^2 r}\right)' \hat{\boldsymbol{\phi}} = \mathcal{T}\left(k^2 r^2 \mathcal{T}\right) \hat{\boldsymbol{\phi}} + 2\alpha\beta^2 Re_c\, \mathcal{T}\, \hat{\boldsymbol{\omega}} \tag{3.7}$$

$$k^2 r^2 \left(Re_c \frac{\partial}{\partial t} + \mathrm{i}\alpha Re_c\, U\right) \hat{\boldsymbol{\omega}} + \frac{\mathrm{i}U'}{r}\, \hat{\boldsymbol{\phi}} = \mathcal{S}\, \hat{\boldsymbol{\omega}} + \frac{2\alpha Re_c}{Re_c^2} \mathcal{T}\, \hat{\boldsymbol{\phi}} \tag{3.8}$$

with:

$$\begin{aligned} &k^2 = \alpha^2 + \frac{\beta^2}{r^2}, \\ &\mathcal{T} = \frac{1}{r^2} - \frac{1}{r}\frac{\partial}{\partial r}\left(\frac{1}{k^2 r}\frac{\partial}{\partial r}\right), \quad \mathcal{S} = k^4 r^2 - \frac{1}{r}\frac{\partial}{\partial r}\left(k^2 r^3 \frac{\partial}{\partial r}\right). \end{aligned}$$

New set of variables, $\hat{\boldsymbol{\phi}}$ and $\hat{\boldsymbol{\omega}}$, describe completely the problem: $\hat{u}$, $\hat{v}$ and $\hat{w}$ can be recovered exploiting the continuity equation and the definitions of the radial vorticity:

$$\hat{u} = -\frac{\alpha}{k^2 r}\frac{\partial \hat{\boldsymbol{\phi}}}{\partial r} - \beta^2 Re_c\, \hat{\boldsymbol{\omega}}, \qquad \hat{v} = -\frac{\mathrm{i}}{r}\, \hat{\boldsymbol{\phi}}, \qquad \hat{w} = -\frac{\beta}{k^2 r^2}\frac{\partial \hat{\boldsymbol{\phi}}}{\partial r} + \alpha\beta r Re_c\, \hat{\boldsymbol{\omega}} \tag{3.9}$$

The boundary conditions that have to be imposed on $\hat{\boldsymbol{\phi}}$ and $\hat{\boldsymbol{\omega}}$ for the solid wall are directly given by the no-slip condition:

$$\hat{\boldsymbol{\phi}} = \hat{\boldsymbol{\phi}}' = \hat{\boldsymbol{\omega}} = 0 \quad \text{at } \; r = 1. \tag{3.10}$$

The centerline boundary condition, instead, are given by the fact the velocity vector has a vanishing azimuthal dependence as the centreline is approached. That leads to

$$\left.\begin{array}{ll} \hat{\boldsymbol{\phi}} = \hat{\boldsymbol{\phi}}' = 0 & \text{for } \; \beta = 0 \\ \hat{\boldsymbol{\phi}} = \hat{\boldsymbol{\omega}} = 0 & \text{for } \; |\beta| = 1 \\ \hat{\boldsymbol{\phi}} = \hat{\boldsymbol{\phi}}' = \hat{\boldsymbol{\omega}} = 0 & \text{for } \; |\beta| \geq 2 \end{array}\right\} \quad \text{at } \; r = 0. \tag{3.11}$$

In order to make easier to work with those equations, it will be of advantage to adopt a matrix form of the problem. Introducing the vector $\mathbf{q} = \left[\hat{\boldsymbol{\phi}}, \hat{\boldsymbol{\omega}}\right]^{\mathrm{T}}$, the governing equations will assume the form

$$\mathcal{L}\mathbf{q} + Re_c \frac{\partial}{\partial t}\mathcal{M}\mathbf{q} = 0 \qquad \Rightarrow \qquad \frac{\partial \mathbf{q}}{\partial t} = \left(-\frac{1}{Re_c}\mathcal{M}^{-1}\mathcal{L}\right) \mathbf{q} = \mathcal{A}\mathbf{q} \tag{3.12}$$

with:

$$\mathcal{L} = \begin{bmatrix} \mathrm{i}\alpha Re_c U \mathcal{T} - \dfrac{\mathrm{i}\alpha Re_c}{r}\left(\dfrac{U'}{k^2 r}\right)' - \mathcal{T}\left(k^2 r^2 \mathcal{T}\right) & -2\alpha\beta^2 Re_c\, \mathcal{T} \\ \\ \dfrac{\mathrm{i}U'}{r} - \dfrac{2\alpha Re_c}{Re_c^2}\mathcal{T} & \mathrm{i}\alpha Re_c\, U\, k^2 r^2 - \mathcal{S} \end{bmatrix}$$

$$\mathcal{M} = \begin{bmatrix} \mathcal{T} & 0 \\ 0 & k^2 r^2 \end{bmatrix}.$$

Considering the numerical approximation $\mathbf{A}$ of the operator $\boldsymbol{\mathcal{A}}$ and its spectral decomposition $\mathbf{A} = \mathbf{T}\boldsymbol{\Lambda}\mathbf{T}^{-1}$, we are able to solve the Cauchy problem:

$$\begin{cases} \dot{\mathbf{q}} = \mathbf{A}\mathbf{q} \\ \mathbf{q}(0) = \mathbf{q_0} \end{cases} \quad \Rightarrow \quad \mathbf{q}(t) = e^{\mathbf{A}t}\,\mathbf{q_0} = \mathbf{T}e^{\boldsymbol{\Lambda}t}\mathbf{T}^{-1}\,\mathbf{q_0} \tag{3.13}$$

3.1.2 Kinetic energy and energy growth function

As we are interested in the transient growth of the perturbation energy, we must express k as a function of the variable $\mathbf{q}$. Manipulating its definition, we obtain:

$$\begin{aligned} k &= \int_0^{2\pi}\int_0^1 \frac{1}{2}\left(|\hat{u}|^2 + |\hat{v}|^2 + |\hat{w}|^2\right)\, r\, dr\, d\theta = \\ &= \pi\int_0^1 \left(|\hat{u}|^2 + |\hat{v}|^2 + |\hat{w}|^2\right)\, r\, dr = \\ &= \pi\int_0^1 \left(\frac{\left|\hat{\boldsymbol{\phi}}'\right|^2}{k^2 r^2} + \frac{\left|\hat{\boldsymbol{\phi}}\right|^2}{r^2} + k^2 r^2 \beta^2\, Re_c\, |\hat{\boldsymbol{\omega}}|^2\right)\, r\, dr, \end{aligned} \tag{3.14}$$

that is an expression of $\mathbf{q} = \left[\hat{\boldsymbol{\phi}}, \hat{\boldsymbol{\omega}}\right]^{\mathrm{T}}$. Defining the scalar product $(\cdot,\cdot)_E$ as

$$(\mathbf{q_1}, \mathbf{q_2})_E = \pi\int_0^1 \left(\frac{\hat{\boldsymbol{\phi}}_1' \hat{\boldsymbol{\phi}}_2^{*'}}{k^2 r^2} + \frac{\hat{\boldsymbol{\phi}}_1 \hat{\boldsymbol{\phi}}_2^*}{r^2} + k^2 r^2 \beta^2\, Re_c\, \hat{\boldsymbol{\omega}}_1 \hat{\boldsymbol{\omega}}_2^*\right)\, r\, dr. \tag{3.15}$$

we are able to rewrite k with its induced norm:

$$k = \|\mathbf{q}\|_E^2 = (\mathbf{q}, \mathbf{q})_E = \mathbf{q}^{\mathrm{H}}\ \mathcal{Q}_E\ \mathbf{q} \tag{3.16}$$

where $\mathcal{Q}_E$ is an appropriate weighting operator.

The energy growth function G(t) is defined as

$$G(t) = \max_{k(0)\neq 0} \frac{k(t)}{k(0)} \tag{3.17}$$

and, remembering the Eq. (3.16), it is possible to explicit its time dependency:

$$G(t) = \max_{\mathbf{q_0} \neq \mathbf{0}} \frac{\|\mathbf{q}(t)\|_E^2}{\|\mathbf{q_0}\|_E^2} = \left\|e^{\mathbf{\Lambda}t}\right\|_E^2 = \left\|\mathbf{C}\mathbf{T}e^{\mathbf{\Lambda}t}\mathbf{T}^{-1}\mathbf{C}^{-1}\right\|_2^2 \tag{3.18}$$

where $\mathbf{Q}_E$ is the numerical approximation of $\mathcal{Q}_E$ and $\mathbf{Q}_E = \mathbf{C}^{\mathrm{T}}\mathbf{C}$ its Cholesky decomposition.

3.1.3 Optimal initial condition

The optimal initial condition is defined as the $\mathbf{q_0}$ such that

$$G_{\max} = \max_{t \geq 0} G(t) = \max_{\mathbf{q_0} \neq \mathbf{0}} \frac{\left\|\mathbf{C}\mathbf{T}e^{\mathbf{\Lambda}t_{G_{\max}}}\mathbf{T}^{-1}\mathbf{C}^{-1}\mathbf{C}\,\mathbf{q_0}\right\|_2^2}{\|\mathbf{C}\,\mathbf{q_0}\|_2^2} \tag{3.19}$$

. Let $\mathbf{z}$ be the first right singular vector of $\mathbf{C}\mathbf{T}e^{\mathbf{\Lambda}t_{G_{\max}}}\mathbf{T}^{-1}\mathbf{C}^{-1}$. The optimal initial condition is:

$$\mathbf{q}_{\mathbf{0},\mathrm{opt}} = \mathbf{C}^{-1}\,\mathbf{z} \tag{3.20}$$

3.2 Results

In this section we will apply tools developed in the previous section in order to compare results given by linear theory and by DNS simulation.

For the numerical approximation of the introduced operators in linear theory, a fourth order finite-difference scheme is used for radial derivatives with an uniform radial grid.

First of all, Figure 3.1 shows the optimal energy growth function for a streamwise constant perturbation at various azimuthal wavenumbers, compared with the original results by Shmid and Henningson. As we can see the results obtained are compatible with the original work considering both energy growth function peaks and shape.

3.2.1 Comparison between DNS and linear theory

We will now compare with linear theory results on energy growth obtained by DNS code, in order both to get an initial validation of the program and to study the influence of initial energy magnitude.

A laminar flow, with Re_P equal to 3000, has been considered.

Direct Numerical Simulation

Thanks to Eq. (3.20), optimal initial condition in transformed variables can be calculated. However, in order to build an initial field compatible with the developed program, we need that field expressed in primitive variables. Applying Eq. (3.9), we get the three components field, as shown in Figure 3.2, where an arbitrary normalization has been used.

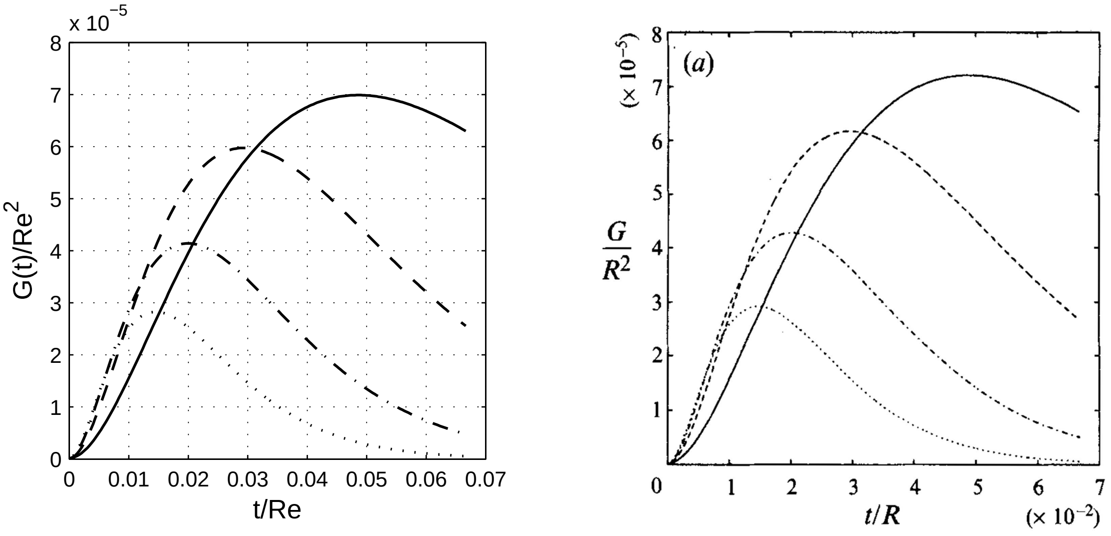

(a) Present (b) [SH94]

Figure 3.1: Optimal energy growth function − $Re = 3000$ and $\alpha = 0$

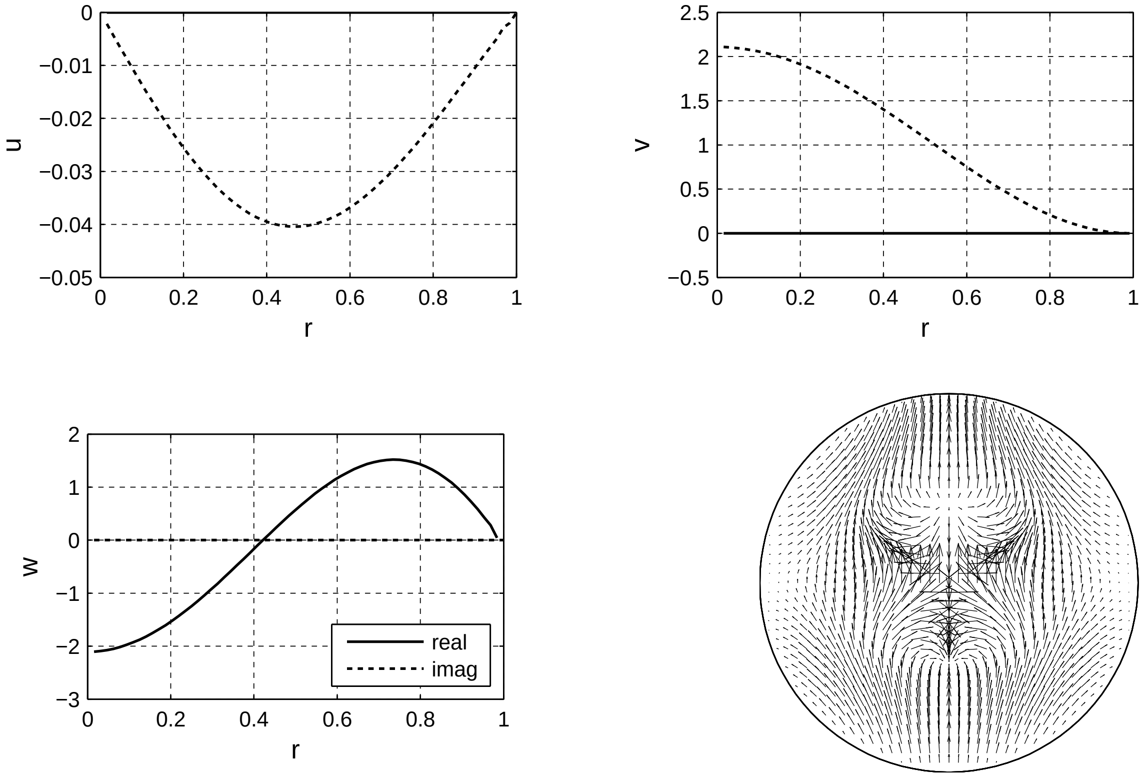

Figure 3.2: Optimal perturbation in primitive variables and cross section of perturbation field − $Re = 3000$, $\alpha = 0$ and $\beta = 1$

For all simulations of this chapter a pipe length of $2\pi R$ has been considered and number of azimuthal and axial modes has been set to 65 with an equally spaced radial grid, $c_{th} = 0$. Simulations have been run for 200 time units with a variable time step calculated in order to maintain a CFL number equal to 1.

n_x	n_r	n_θ	L	c_{ht}	Re	Q	$\text{cfl}_{\max}$	$t_{\max}$
32	64	32	$2\pi R$	0	3000	0.5π	1.0	200

Table 3.1: DNS parameters

Effects by initial energy magnitude

The theory developed before is based on linearized Navier-Stokes equations: considering that those equation have their validity for small perturbation of the laminar flow, we expect that growth of perturbation energy k will depend by the magnitude of the initial perturbation field. As a measure of initial magnitude has been considered the perturbation energy $k(0)$ at the initial time. The response of the system has been studied when varying $k(0)$ from 10^{-4} to 10^{-16}.

In Figure 3.3, we can have a first look of obtained results: as the lowest energy case match the theoretical function, for an initial energy equal to 10^{-6}, the energy growth shows a lower energy peak and, for $k(0) = 10^{-4}$, instead, there is no similarity to the linear case.

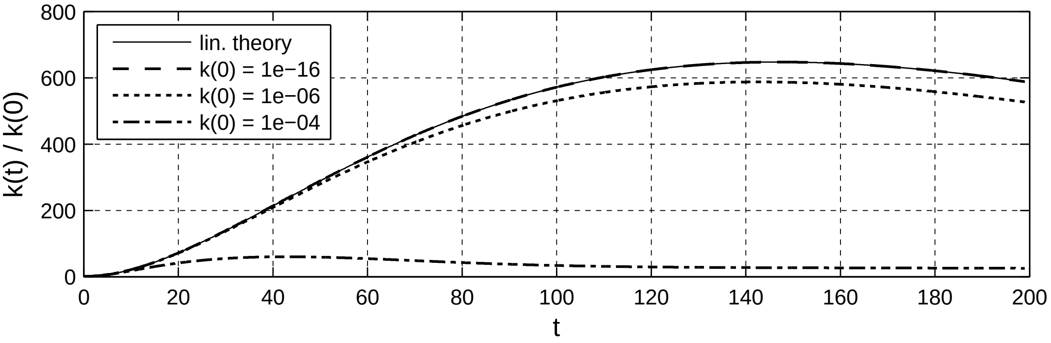

Figure 3.3: Energy transient growth $-$ $Re = 3000$, $\alpha = 0$ and $\beta = 1$

An explanation of this behavior is the loss of the monochromatic property of the energy growth because, during the time evolution, other modes are involved. Figure 3.4 reports a measure of this coupling effect, i.e. difference between the total perturbation energy and contribution to $k(t)$ given by initially excited mode. We can see that the higher the initial energy, the greater the coupling effect.

Introducing a scalar measure of these two errors may be useful. Here are defined the error on the energy growth err_k and a measure of coupling between modes $err_{coupl.}$:

$$err_k = \frac{\|g - g_{ref}\|^2_{L2}}{\|g_{ref}\|^2_{L2}}, \qquad err_{coupl.} = \frac{\|g - g_{\alpha,\beta}\|^2_{L2}}{\|g\|^2_{L2}} \tag{3.21}$$

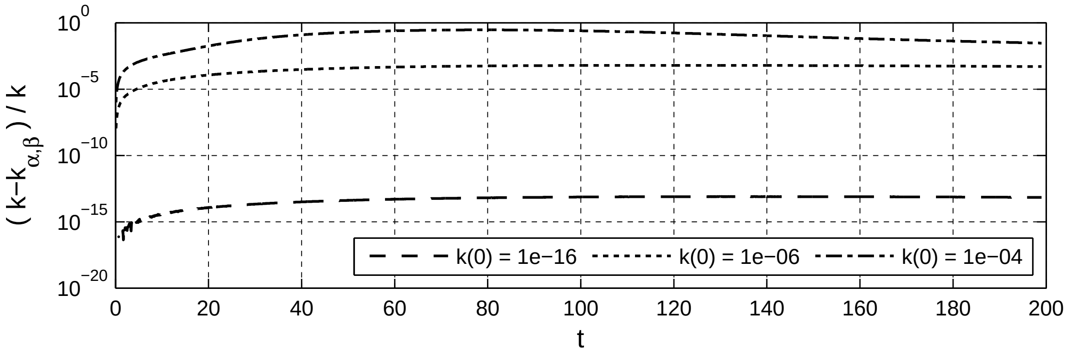

Figure 3.4: Coupling - $Re = 3000$, $\alpha = 0$ and $\beta = 1$

where $g(t) = \frac{k(t)}{k(0)}$. As reference for err_k, a simulation with $k(0) = 10^{-20}$ and cfl $= 0.2$ has been taken.

Figure 3.5 shows the influence of k(0) up these two quantities. As the coupling effect gets smaller, the error on the energy growth decreases, supporting the assumption that we have made before, until it reaches an asymptotic value, probably due to roundoff noise float or some issues due to CFL number.

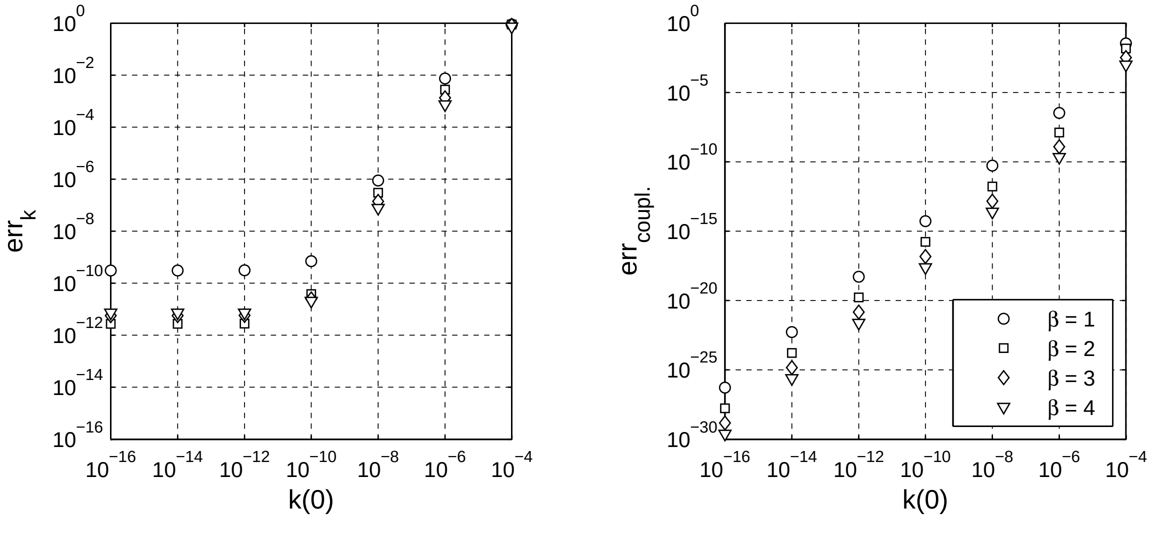

Figure 3.5: Influence of $k(0)$ - $Re = 3000$, $\alpha = 0$

The mean flow is also involved in this transient: as we can see from Figure 3.6 while coupling effect is higher, i.e. higher values of initial perturbation energy, mean flow characteristics vary enormously from Poiseuille flow. When k(0) is set to 10^{-4}, mean centerline axial velocity halves itself while wall-normal derivative peaks to one and a half of its initial value.

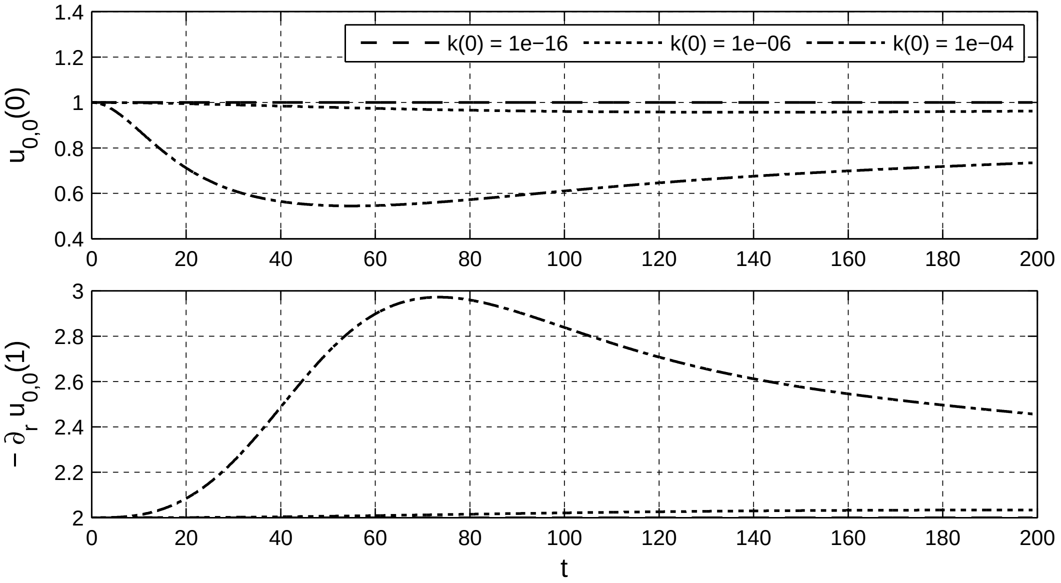

Figure 3.6: Mean flow

Effects by CFL number

A posteriori study on the influence on the energy growth by CFL number has been made: keeping an initial perturbation energy of 10^{-16}, CFL number has been varied between 0.2 and 1.0, value used for previous simulations.

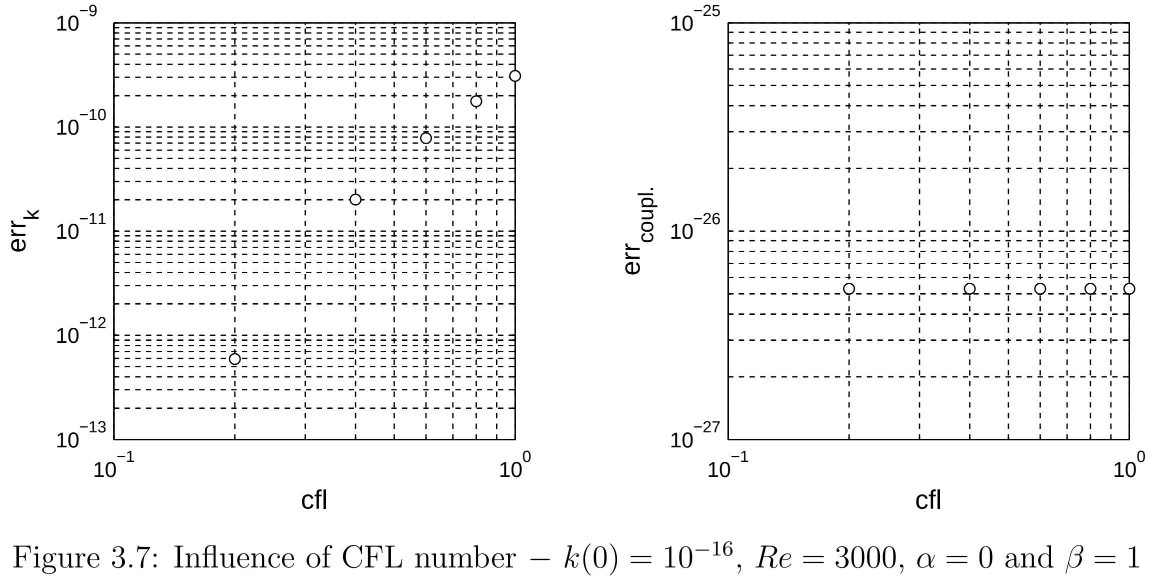

Figure 3.7: Influence of CFL number – $k(0) = 10^{-16}$, $Re = 3000$, $\alpha = 0$ and $\beta = 1$

Figure 3.7 shows no significative influence on coupling. Instead, there is a little effect on energy error, that decreases as the CFL number approaches to zero: because of regularity of this influence, all previous observations on function behavior are still well-founded.

4. TURBULENT FLOW

In this chapter previously developed, optimal initial condition theory will be used to generate a fully turbulent flow in order to compare its statistics with other similar work in literature.

As main reference has been chosen work developed by Quadrio an Sibilla, [QS00]. In this work, flow in $20R$ length pipe is studied for a Reynolds number Re_P, based on centerline velocity of discharge equivalent Poiseuille flow, of 4900.

n_x	n_r	n_θ	L	c_{ht}	Re	Q	$\text{cfl}_{\max}$
128	96	64	$20R$	0	4900	0.5π	1.0

Table 4.1: DNS parameters – it is reminded that n_x and n_θ are half the axial and azimuthal modes added to $\alpha = 0$ and $\beta = 0$ mode.

Simulation by Quadrio and Sibilla was performed on a finite difference grid with $257 \times 97 \times 129$ points along axial, radial and azimuthal direction: to maintain an equivalent spatial resolution we chose 257 modes along axial direction, 129 along azimuthal direction and 97 points on pipe radius and the same domain length. Variable azimuthal modes have been used.

4.1 Transition

As we saw in Section 3.2.1, for higher values of initial perturbation energy all modes are involved in energy growth and, also, the mean velocity profile is highly perturbed during transient. The idea is to exploit this behavior to force a Poiseuille flow to transient to a turbulent flow, despite its property to be linearly stable for any value of Reynolds number.

In order to do that we impose an initial optimal perturbation energy higher than used in previous investigations and add a small random noise in all the other modes.

optimal pert.			noise
α_{opt}	β_{opt}	$k_{opt}(0)$	$k_n(0)$
0	1	$5 \cdot 10^{-3}$	$5 \cdot 10^{-9}$

Table 4.2: Initial condition

Figure 4.1 shows the transient in $k(t)$, where various contributes to it are highlighted: $k_{0,1}$ indicates perturbation energy due to $\alpha = 0$ and $\beta = 1$ mode only, hence $k_{0,*}$ indicates all streamwise-constant contributes.

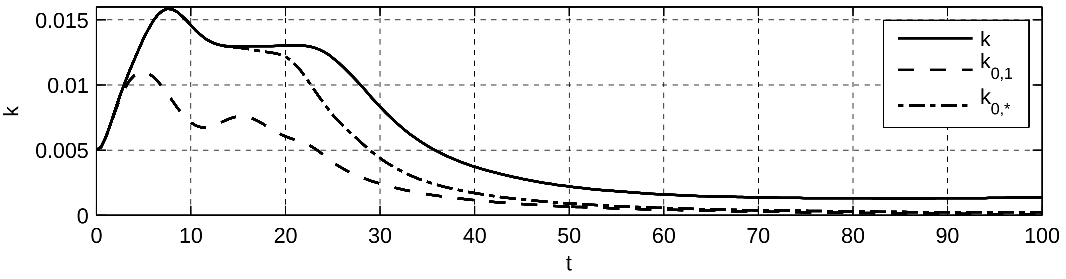

Figure 4.1: k during transition

After 5 time units perturbation energy is no longer monochromatic, and other streamwise-constant azimuthal modes are activated. Energy peaks after 8 units, while the perturbation still remain constant along the axis, Figure 4.3b.

First oscillations along axial direction appear after 14 time units, as we can see in Figure 4.1 and in Figure 4.3c. From this point flow nature changes radically: high magnitude oscillations compare in lower half of domain, decaying in a turbulent flow after almost 80 time units.

As we can see from Figure 4.3i, a distinction between a lower and a upper part of pipe is still visible after 50 time units and gradually vanishes as long as flow become fully turbulent, Figure 4.3j.

Some information about the behavoir of mean flow profile can be found in run-time file, Figure 4.2. Centerline velocity quickly decay while perturbation energy grows and, after a few oscillations, reaches its steady value. On the wall energy growing influence is lower and stramwise velocity wall-normal derivative starts to change when energy peaks: Figure 4.3a shows that wall mean stress starts to change when the perturbation structure reaches the wall.

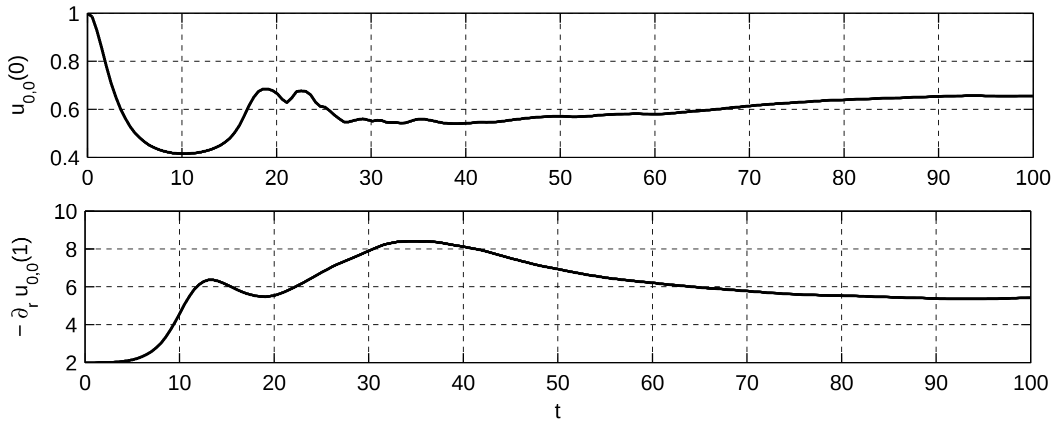

Figure 4.2: Mean flow during transition

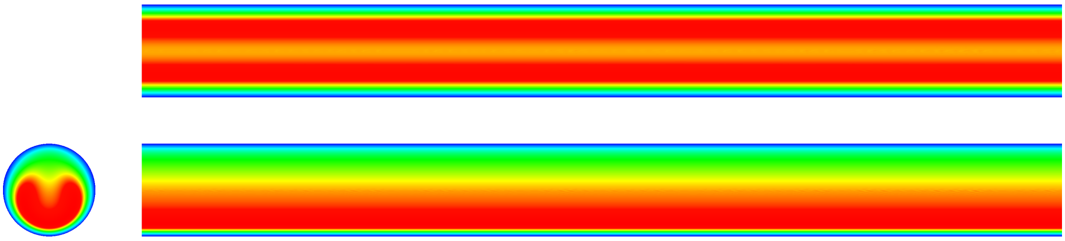

(a) $t = 4$

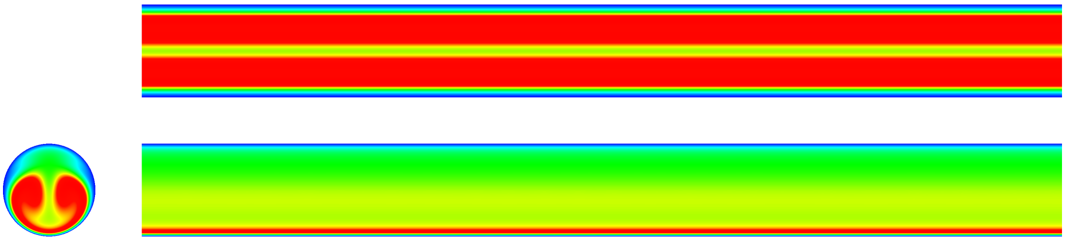

(b) $t = 8$

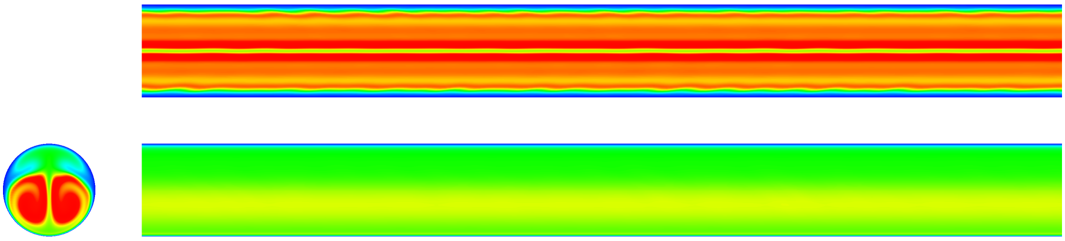

(c) $t = 14$

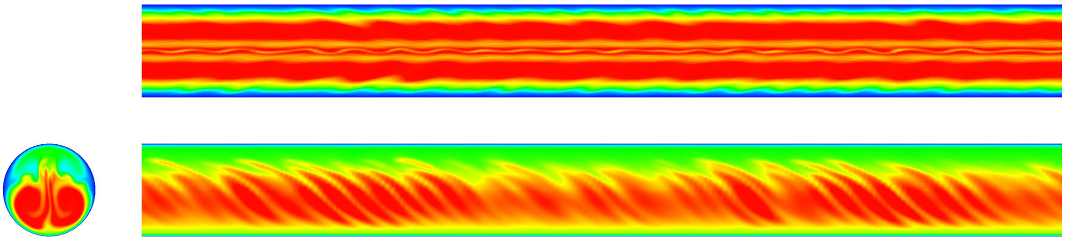

(d) $t = 18$

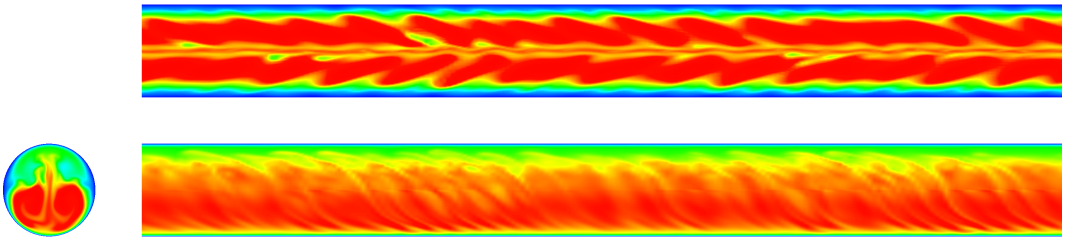

(e) $t = 20$

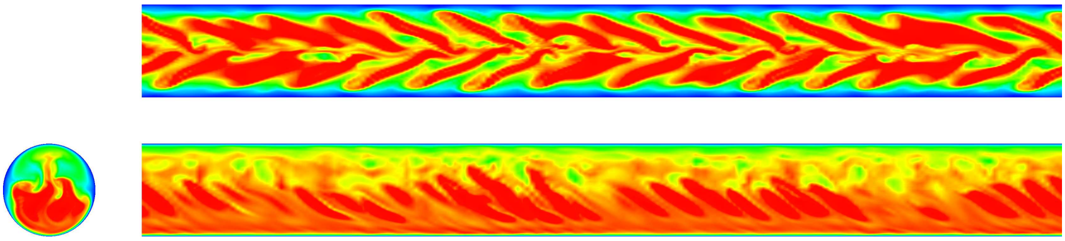

(f) $t = 22$

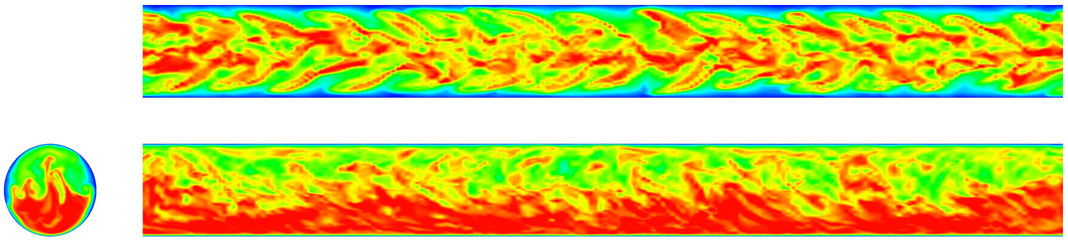

(g) $t = 26$

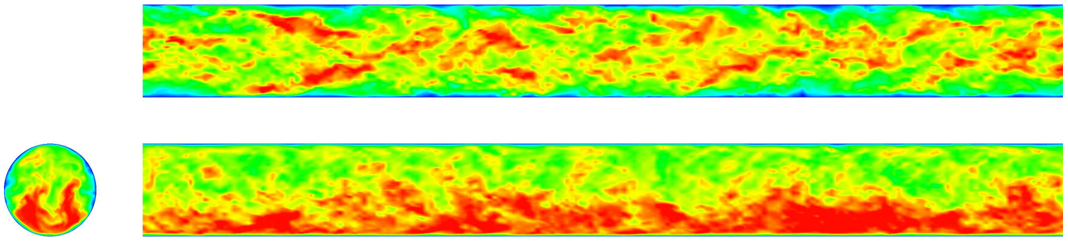

(h) $t = 32$

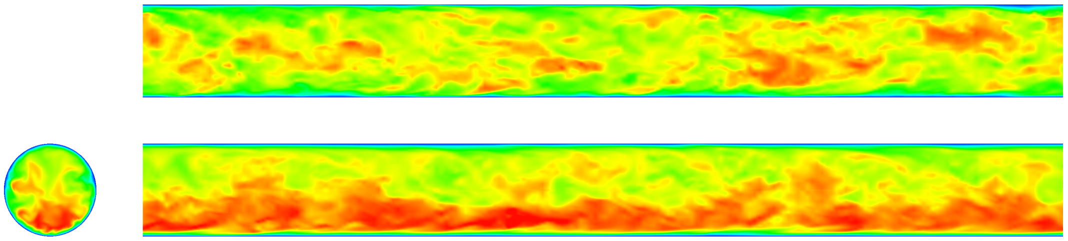

(i) $t = 50$

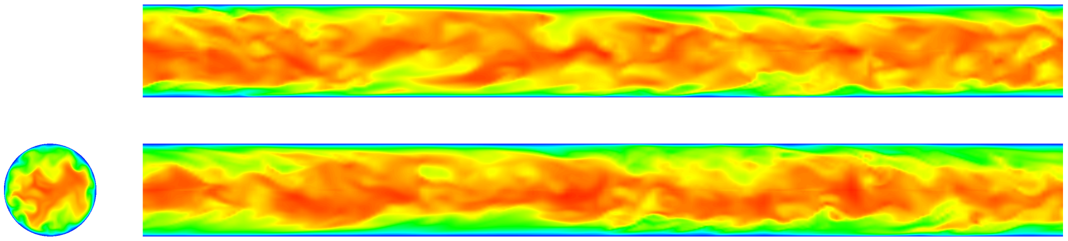

(j) $t = 100$

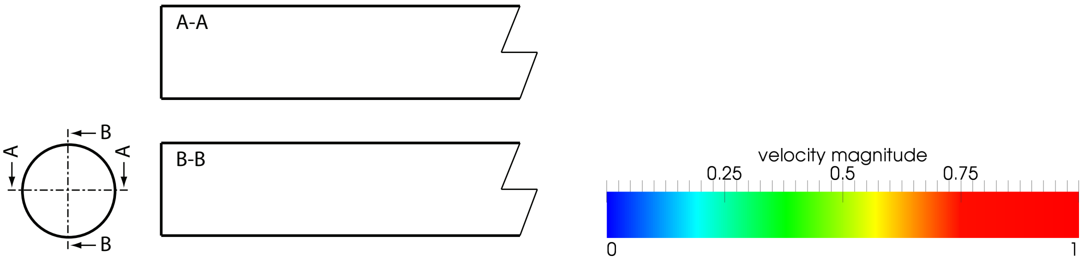
A-A
B-B
B
A
A
B
velocity magnitude
0.25
0.5
0.75
0
1

Figure 4.3: Evolution of mean velocity magnitude during transition − cross section: $x = 0$; upper section: A-A; lower section: B-B

4.2 Fully developed turbulent flow

After 500 time units, we considered turbulent flow fully developed. From this time, simulation have been forked into three distinct simulations: one uses constant azimuthal mode, another azimuthal variable modes with no regularity conditions and a last one azimuthal variable modes applying regularity conditions, as before. Figure 4.4 shows temporal stories of perturbation energy of the three simulations.

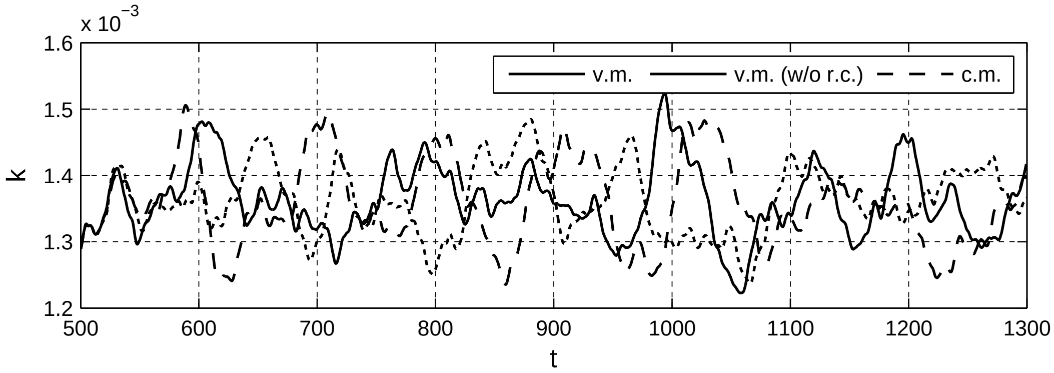

Figure 4.4: Perturbation energy evolution for fully turbulent flow

Statistics have been computed on 41 fields taken at a constant rate of 20 time units: total sampling time results to be 800 time units, corresponding to the time taken to cover 20 pipes length at U_b.

	Present			[QS00]	[OF97]
	v.m.	v.m. (w/o r.c.)	c.m.		
U_c/U_b	1.315	1.317	1.315	1.31	1.31
U_b/u_τ	14.40	14.40	14.50	14.24	14.41
U_c/u_τ	18.94	18.97	19.07	18.63	18.87
Re_P	4900	4900	4900	4900	4900
Re_c	3222	3228	3221	3210	3200
Re_τ	170.1	170.1	169.0	172	170

	[WM08]	[LMMC97]	[EUW$^+$94] DNS	[EUW$^+$94] PIV
U_c/U_b	1.31	1.29	1.31	1.30
U_b/u_τ	14.61	14.77	14.73	14.88
U_c/u_τ	19.25	19.11	19.31	19.38
Re_P	5300	5600	5300	5450
Re_c	3230	3620	3475	3550
Re_τ	180	190	180	183

Table 4.3: Global properties for mean turbulent flow

In Table 4.3, are shown some global quantities computed for the turbulent flows from the three different simulations. They are compared with results from both numerical simulations and experiments, at equal or similar Reynolds numbers: all flow indicators of performed simulations are very close to reference results reported in Table 4.3, even to experimental results by [EUW$^+$94].

All selected reference simulations are based upon second order finite-differences scheme for derivatives approximation in all coordinate directions. Main differences between those works can be found in pipe length. [QS00], with its L/R ratio equal to 20, is the longest simulation considered and the closest to $8\pi R$ pipe length, recommended by [COMB10] for convergence of turbulence statistics. L/R ratio for other simulations varies between 10 of older works by [EUW$^+$94], [LMMC97] and [OF97] to 15 by [WM08].

Turbulent flow present also the near-wall peak at $y^+ \approx 14$ and $\lambda^+ \approx 110$ described by [HM07] for channel flow, both for variable and constant modes, as we can see from Figure 4.5. However, because of low Reynolds number, there is not the outer peak.

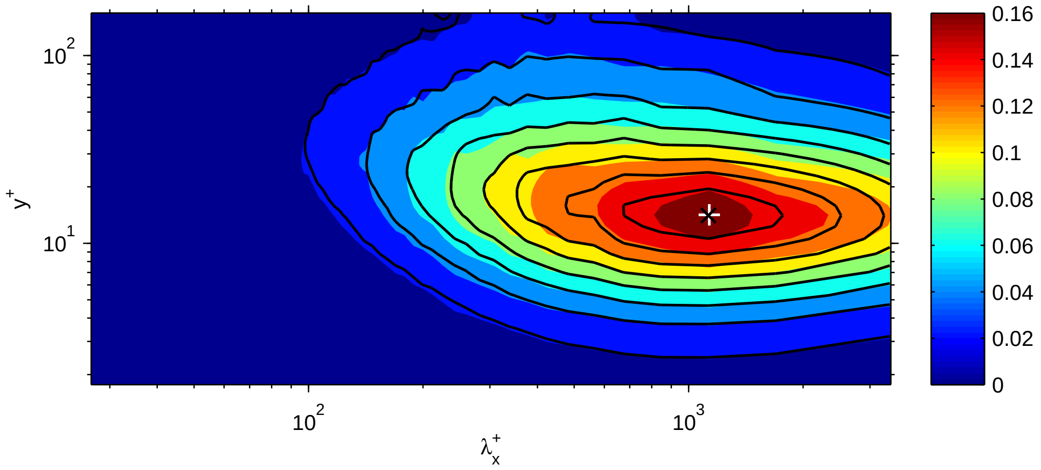

Figure 4.5: Premultiplied axial power spectrum of axial velocity fluctuation $\alpha\,\Phi^+_{uu}$ along wall-normal direction – colored surface: variable modes simulation; contour lines: constant modes simulation

Those peaks can be found in all wall-bounded turbulent flows, such as channels an boundary layers, at the same wall distance and wavelength measured in wall units, [MHN$^+$06].

4.2.1 Variable and constant azimuthal modes

A peculiarity of this code is our introduction of variable azimuthal modes: in this section we are going to compare results obtained with the two different modes distributions in order to find limits and advantages.

A first comparison is made on mean velocity and Reynolds mean stresses profiles: as we can see from Figure 4.6, where y denotes radial distance from the wall, no

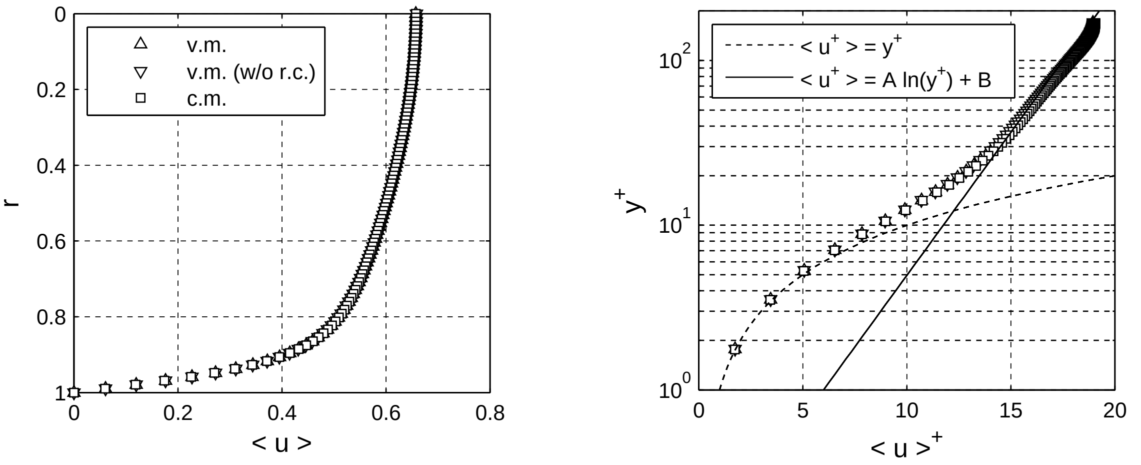

Figure 4.6: Mean velocity profile $-$ $A = 2.5$ and $B = 6.0$

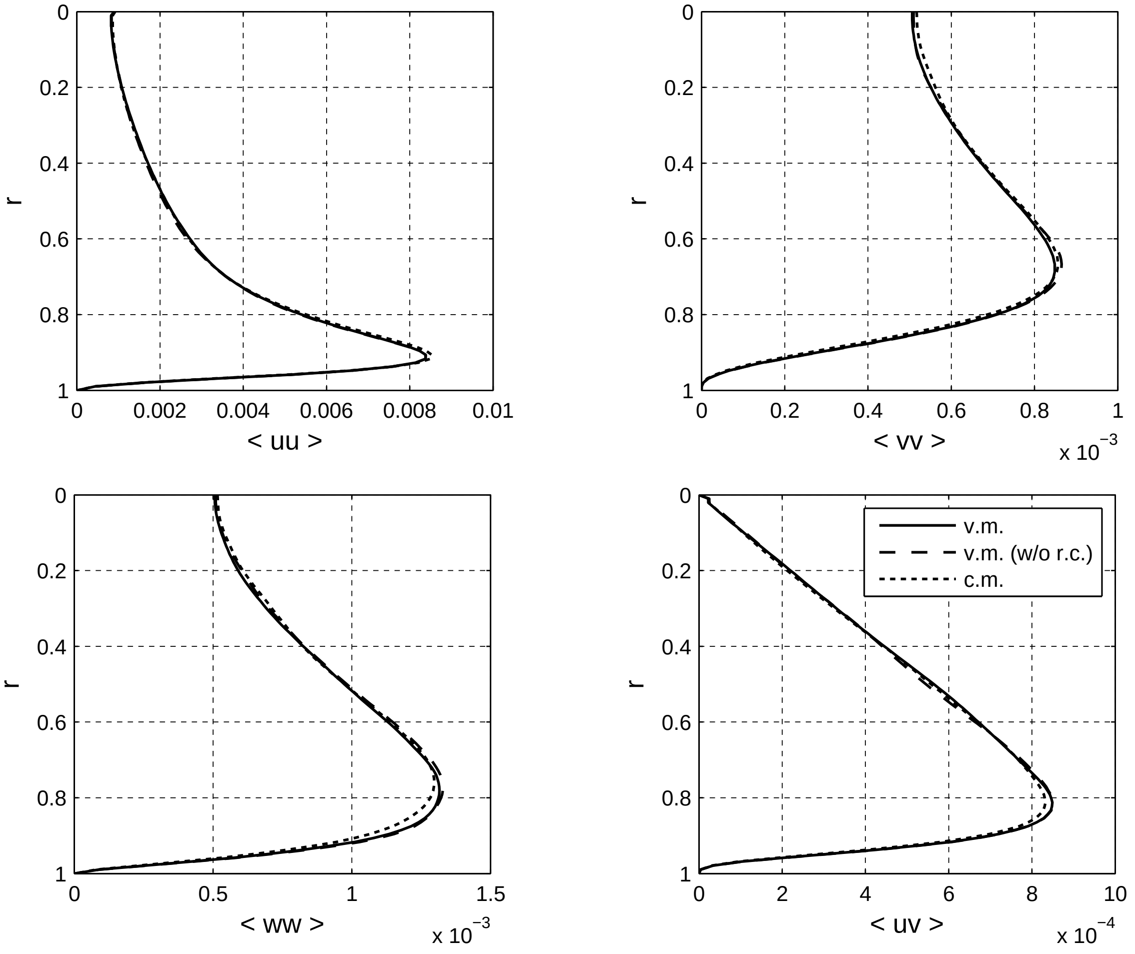

Figure 4.7: Reynolds mean stresses

significative difference is visible on mean velocity and also a good consistency with the log law is shown, despite the low Reynolds number. However, Reynolds mean stresses differ in near wall region, as reported in Figure 4.7. Especially on $\langle ww \rangle$ and $\langle ww \rangle$, variable modes simulations overestimate stress value respect constant modes one.

Azimuthal resolution

Resolution problems, due to the variable azimuthal modes distribution, can explain those differences. In order to better understand this behavior, in Figure 4.8, azimuthal power spectra of axial velocity fluctuation along radial direction are reported. This figure gives an idea of the approximation made by varying azimuthal modes by comparing energy levels along radial direction. Near the axis, energy cutoff due occurs for an energy level of 10^{-8} and variable modes energy contours match constant modes ones. However, in near wall region approaching inner energy peak, cutoff occurs for higher energy and energy contours differs between variable and constant modes simulations.

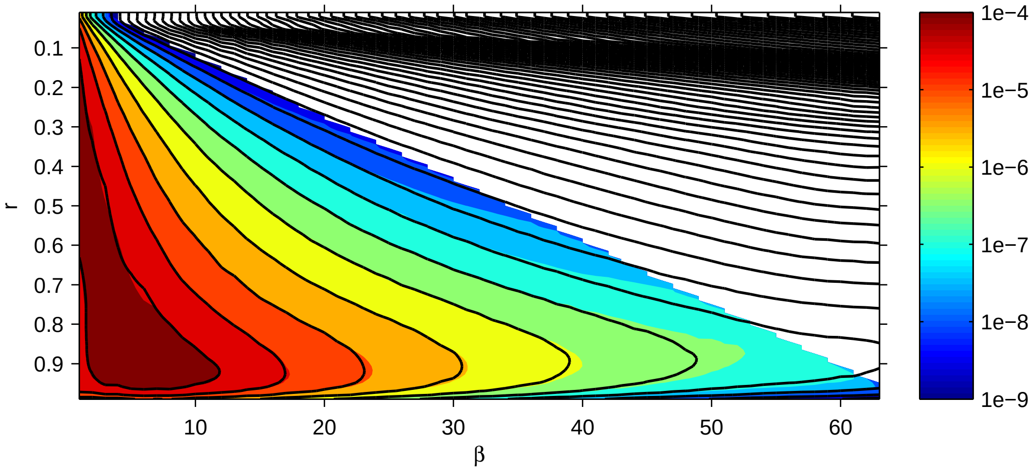

Figure 4.8: Azimuthal power spectra of axial velocity fluctuation Φ_{uu} – colored surface: variable modes simulation; contour lines: constant modes simulation

A solution for this problem could be an azimuthal modes distribution based on perturbation energy distribution along radial direction.

Regularity conditions

A distinctive characteristic of developed code is considering regularity constraints on Fourier series coefficients in using variable azimuthal modes, Section 2.1.2.

Azimuthal power spectra reported in Figure 4.9 permits us to appreciate benefits given by this feature on statistics: we can see that, both near the axis and the wall, energy cutoff is smoother and energy level more similar to constant modes simulation, if regularity conditions are applied.

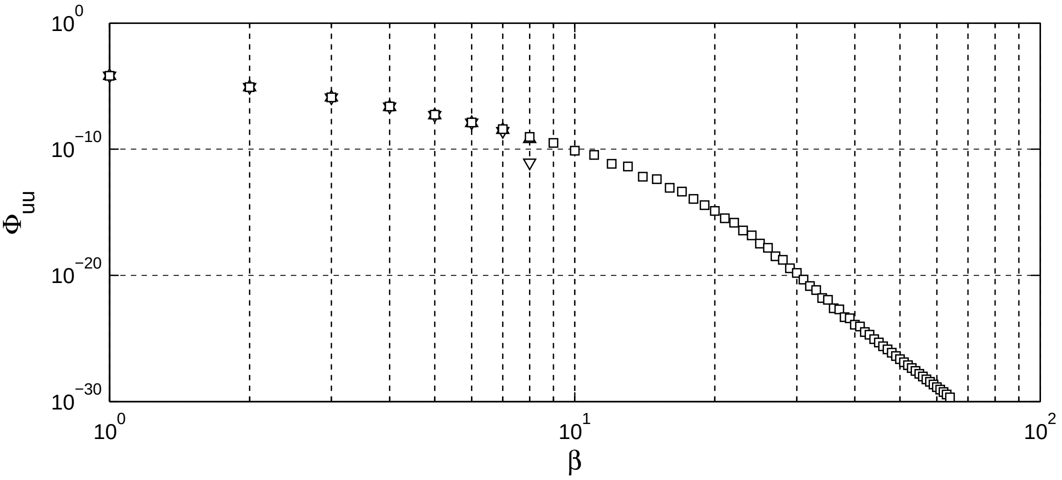

(a) $r = 0.08333$ ($y^+ \approx 156$)

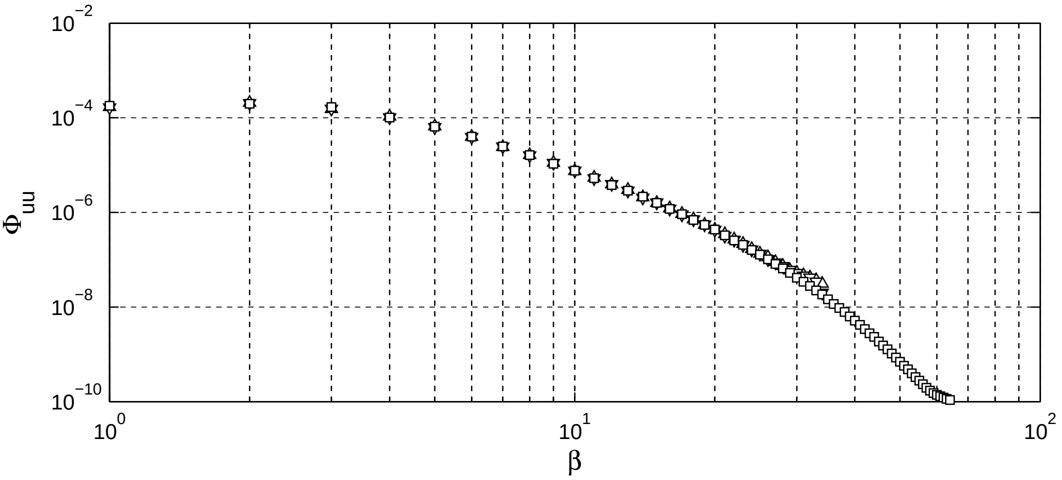

(b) $r = 0.5$ ($y^+ \approx 85$)

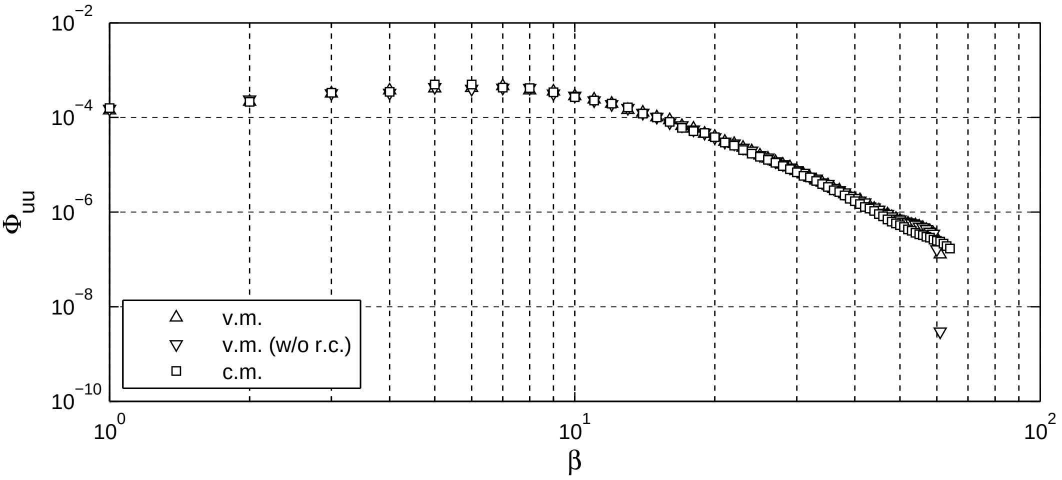

(c) $r = 0.91667$ ($y^+ \approx 14$)

Figure 4.9: Azimuthal power spectra of axial velocity fluctuation Φ_{uu}

Time step

A strong point of variable azimuthal modes is that they allow a higher time step than constant ones. We can see from Figure 4.10 that actual gain on time step is over 10 times.

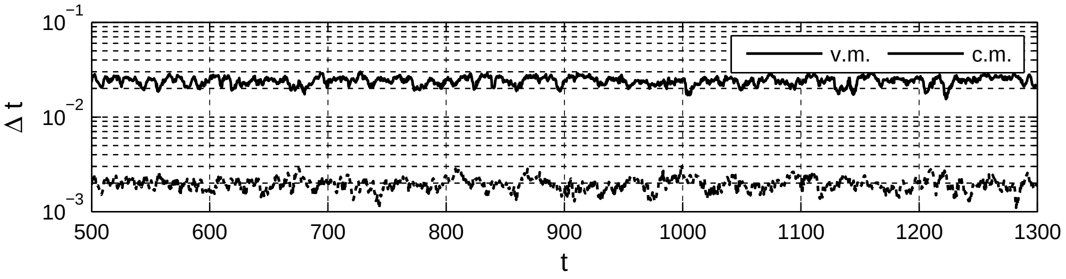

Figure 4.10: Time step

Obviously this has its influence on run-time: as we can see from Table 4.4, constant modes simulation needed a number of time steps 12.25 time higher than the variable one. Also, considering that a variable modes time integration step takes less time than constant, gain on runtime is higher than that.

v.m.	v.m. (w/o r.c.)	c.m.
16811	16800	205760

Table 4.4: Number of time integration steps from t=500 to t=900

An explanation of this behavior can be found in the evaluation of time step by a CFL condition. As we have described in Section 2.3.2, time step is calculated by the variable χ, which can be seen as the CFL number for an unitary time step.

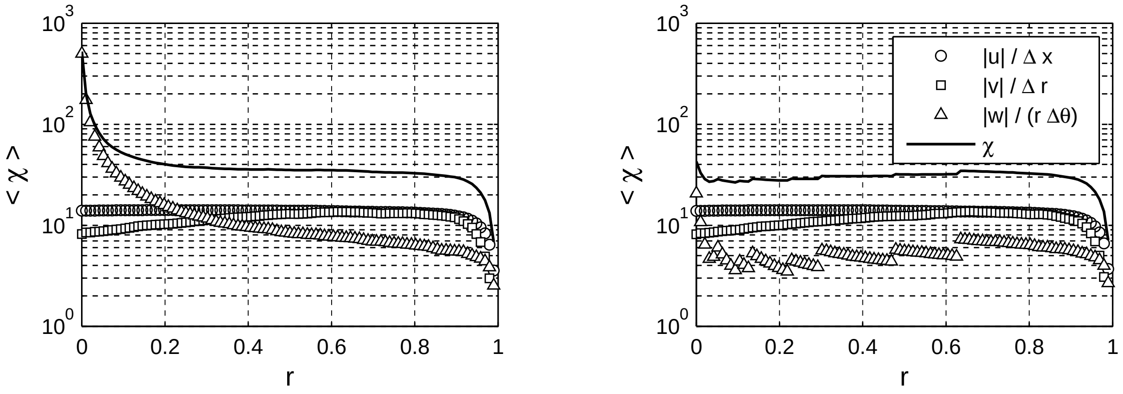

(a) constant modes

(b) variable modes

Figure 4.11: Mean χ distribution

Figure 4.11 reports mean χ along radial direction. The effect of variable modes is clearly visible: while, in constant modes case, the azimuthal contribute grows monotonically approaching the axis, in Figure 4.11(b) we can see the effect of $n_{x,d}$ changing along radial direction. The ratio between peaks of $\langle\chi\rangle$ results to be 12.25, that, as predictable, equals to the inverse of ratio of the number of time-integration.

5. CONCLUSIONS

A Direct Numerical Simulation code, based on an axial and azimuthal Fourier expansion of Navier Stokes equation, has been developed.

Innovative feature of this code is the introduction of variable azimuthal modes along radial direction on which regularity conditions are applied, Section 2.2.3: respect former implementation of variable azimuthal modes, this method allow us to take into account physical constraints on the coefficients of Fourier expansion.

Moreover, compact support given by compact finite-differences scheme, permitted us to easily parallelize the program, Section 2.4, this reducing to a minimum the amount of communications between machines.

Validation

Program has been validated following two different strategies, one based on laminar flow and one on turbulent statistics.

A first validation, Section 3.2.1, has been made comparing DNS results of optimal perturbation energy growth in laminar flow to its theoretical trend. Simulated results match linear theory as long as initial perturbation energy density remains under $10^{-10}\,U_{c,P}^2$.

Secondly, the code has been validated by comparing statistics, obtained from turbulent fields generated by developed program, to results found in literature, as reported in Section 4.2. In order to generate a fully developed turbulent flow, on which statistics can be calculated, an high energy optimal perturbation has been used to force laminar flow to reach the turbulent regime, as described in Section 4.1.

Discussion

Comparing results obtained by constant and variable azimuthal modes, some minor differences has been noticed in azimuthal power spectra. First attempt of variable azimuthal modes distribution was based on geometrical considerations only and didn't take into account the azimuthal modes energy distribution in near wall region.

This problem can be easily solved by adopting an azimuthal modes distribution that consider energy trend along radial direction, such as the proposed one in Figure 5.1. In this prospective the radial distribution of azimuthal modes will depend on Reynolds number: in fact, the position of the near wall energy peaks described by [MHN$^+$06] scales with Re.

The comparison between simulations performed with or without variable modes confirmed also other expected strong points of developed program. Use of regularity

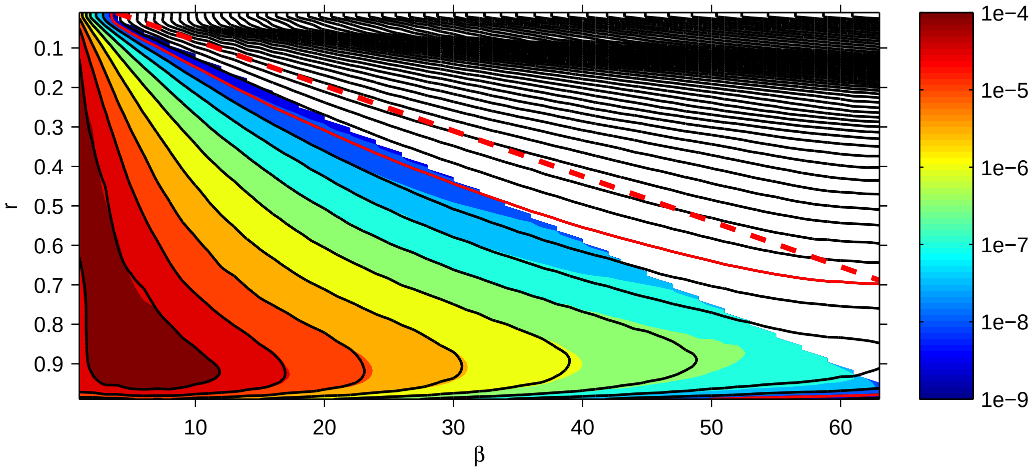

Figure 5.1: Azimuthal power spectra of axial velocity fluctuation Φ_{uu} – colored surface: variable modes simulation; contour lines: constant modes simulation, red contour: $\Phi_{uu} = 10^{-8}$; red dashed line: suggested energy-compliant azimuthal modes distribution

conditions, in variable modes approach, smoothed energy cutoff in azimuthal power spectra respect to simple cut condition. Expected gain on time step is also present: performing two simulation at the same imposed CFL number, variable modes simulation time step results higher by an order of magnitude respect constant simulation one, with direct impact on run-time of simulation.

Further developments

Compact finite-differences scheme, that have been used in calculating radial second derivative, presents only a second order accuracy, despite first derivative operator which is forth-order. An enhancement of order of accuracy of D_* operator would secure a forth-order accuracy to the whole method.

Parallel performances of the program are also to be tuned: a parallel efficiency by 75% has been achieved by a simulation split upon ten machines, Section 2.4.1, a long way off from theoretical speedup given by program architecture. Better results can be obtained by improving load-balancing between nodes: this enhancement can be easily carried out by refining load-balancing weight function, that has only been drafted in this version of the code.

Program source has been written in order to be flexible: it implements a pure DNS but the modular structure makes easier further development, such as a passive scalar equation or a time-dependent boundary condition on wall, feature that could be useful to a better study of flow-control strategies.

All those features makes the developed code a powerful instrument in turbulence study: we have built a virtual wind-tunnel, now it is only to be used.

BIBLIOGRAPHY

[ABB$^+$10] F. Auteri, A. Baron, M. Belan, G. Campanardi, and M. Quadrio. Experimental assessment of drag reduction by traveling waves in a turbulent pipe flow. *Phys. Fluids*, 22(11):115103/14, 2010.

[Boe11] B.J. Boersma. Direct Numerical Simulation of turbulent pipe flow up to a Reynolds number of 61, 000. Proc. of the XIII European Turbulence Conference, 2011.

[COMB10] C. Chin, A.S.H. Ooi, I. Marusic, and H.M. Blackburn. The influence of pipe length on turbulence statistics computed from direct numerical simulation data. *Phys. Fluids*, 22(115107):1–10, 2010.

[EUW$^+$94] J.G.M. Eggels, F. Unger, M.H. Weiss, J. Westerweel, R.J. Adrian, R. Fiedrich, and F.T.M. Nieuwstadt. Fully developed turbulent pipe flow: a comparison between direct numerical simulation and experiment. *Journal of Fluid Mechanics*, 268:175–209, 1994.

[HM07] N. Hutchins and I. Marusic. Evidence of very long meandering features in the logarithmic region of turbulent boundary layers. *J. Fluid Mech.*, 2007.

[KMM87] J. Kim, P. Moin, and R. Moser. Turbulence statistics in fully developed channel flow at low Reynolds number. *J. Fluid Mech.*, 177:133–166, 1987.

[LB90] H.R. Lewis and P.M. Bellan. Physical constraints on the coefficients of Fourier expansion in cylindrical coordinates. *J. Math. Phys.*, 31(11):2592–2596, 1990.

[Lel92] S.K. Lele. Compact Finite Difference Schemes with Spectral-like Resolution. *J. Comp. Phys.*, 103:16–42, 1992.

[LMMC97] P. Loulou, R.D. Moser, N.N. Mansour, and B. J. C. Cantwell. Direct Numerical Simulation of incompressible pipe flow using a B-spline spectral method. Technical Report 110436, NASA, 1997.

[LQ06] P. Luchini and M. Quadrio. A low-cost parallel implementation of direct numerical simulation of wall turbulence. *J. Comp. Phys.*, 211(2):551–571, 2006.

[MHN$^+$06] J.P. Monty, N. Hutchins, H. C. H. Ng, I. Marusic, and M.S. Chong. A comparison of turbulent pipe, channel and boundary layer flows. *J. Fluid Mech.*, 632:431–442, 2006.

[OF97] P. Orlandi and M. Fatica. Direct simulations of turbulent flow in a pipe rotating about its axis. *J. Fluid Mech.*, 343:43–72, 1997.

[QL02] M. Quadrio and P. Luchini. Direct numerical simulation of the turbulent flow in a pipe with annular cross-section. *Eur. J. Mech. B / Fluids*, 21:413–427, 2002.

[QL04] M. Quadrio and P. Luchini. The numerical solution of the incompressible Navier–Stokes equations in cartesian and cylindrical geometries on a low-cost, dedicated parallel computer. *Dip. Ing. Aerospaziale, Politecnico di Milano*, DIA-SR 04-16, 2004.

[QS00] M. Quadrio and S. Sibilla. Numerical simulation of turbulent flow in a pipe oscillating around its axis. *J. Fluid Mech.*, 424:217–241, 2000.

[Rey83] O. Reynolds. An experimental investigation on the circumstances which determine whether the motion of water shall be direct or sinuous, and the law of resistance in parallel channels. *Proc. R. Soc. London A*, 35:84, 1883.

[RM91] M.M. Rai and P. Moin. Direct simulations of turbulent flow using finite-difference schemes. *Journal of Computational Physics*, 96:15, 1991.

[SH94] P.J. Schmid and D.S. Henningson. Optimal energy density growth in Hagen-Poiseuille flow. *Journal of Fluid Mechanics*, 277:197–255, 1994.

[TPF$^+$08] A. Talamelli, F. Persiani, J.H.M. Frannsson, P.H. Alfredsson, A.V. Johansson, H.M. Nagib, J.D. Ruedi, K.R. Sreenivasan, and P.A. Monkewitz. CICLoPE – a response to the need for high Reynolds number experiments. *Fluid Dynamic Research*, 2008.

[VO96] R. Verzicco and P. Orlandi. A Finite-Difference Scheme for Three-Dimensional Incompressible Flows in Cylindrical Coordinates. *Journal of Computational Physics*, 123:402–414, 1996.

[WM08] X. Wu and P. Moin. A direct numerical simulation study of the mean velocity characteristics in turbulent pipe flow. *J. Fluid Mech.*, 608:81–112, 2008.

ACKNOWLEDGMENTS

Foremost, I owe my deepest gratitude to my supervisor, prof. Maurizio Quadrio, for his precious advice and patient assistance. I would also like to thank prof. Paolo Luchini that gives us his unique help to solve some crucial problems of this work.

APPENDIX

A. FURTHER STATISTICS

r	$\langle u \rangle$	$\langle uu \rangle$	$\langle vv \rangle$	$\langle ww \rangle$	$\langle uv \rangle$	$\langle \tau \rangle$
0.0000E+00	6.5757E-01	9.0353E-04	5.0621E-04	5.0537E-04	-4.5578E-22	7.2504E-19
1.0417E-02	6.5738E-01	8.3603E-04	5.0615E-04	5.0673E-04	2.2643E-05	-1.4063E-06
2.0833E-02	6.5738E-01	8.3603E-04	5.0615E-04	5.0674E-04	2.2644E-05	-1.7882E-06
3.1250E-02	6.5719E-01	8.3415E-04	5.0665E-04	5.0811E-04	3.3702E-05	-4.0711E-06
4.1667E-02	6.5696E-01	8.3219E-04	5.0742E-04	5.1006E-04	4.4030E-05	-5.0779E-06
5.2083E-02	6.5667E-01	8.3848E-04	5.0836E-04	5.1252E-04	5.5239E-05	-6.1365E-06
6.2500E-02	6.5633E-01	8.4534E-04	5.0966E-04	5.1548E-04	6.6255E-05	-7.2025E-06
7.2917E-02	6.5594E-01	8.5609E-04	5.1111E-04	5.1890E-04	7.7810E-05	-8.2429E-06
8.3333E-02	6.5549E-01	8.6752E-04	5.1294E-04	5.2275E-04	8.9225E-05	-9.2583E-06
9.3750E-02	6.5499E-01	8.8135E-04	5.1492E-04	5.2707E-04	1.0097E-04	-1.0246E-05
1.0417E-01	6.5445E-01	8.9575E-04	5.1733E-04	5.3179E-04	1.1253E-04	-1.1222E-05
1.1458E-01	6.5385E-01	9.1180E-04	5.1990E-04	5.3689E-04	1.2427E-04	-1.2200E-05
1.2500E-01	6.5320E-01	9.2837E-04	5.2289E-04	5.4225E-04	1.3584E-04	-1.3190E-05
1.3542E-01	6.5250E-01	9.4623E-04	5.2603E-04	5.4789E-04	1.4757E-04	-1.4184E-05
1.4583E-01	6.5175E-01	9.6476E-04	5.2955E-04	5.5381E-04	1.5922E-04	-1.5166E-05
1.5625E-01	6.5095E-01	9.8466E-04	5.3314E-04	5.6005E-04	1.7104E-04	-1.6114E-05
1.6667E-01	6.5011E-01	1.0056E-03	5.3709E-04	5.6660E-04	1.8277E-04	-1.7018E-05
1.7708E-01	6.4922E-01	1.0281E-03	5.4108E-04	5.7358E-04	1.9459E-04	-1.7883E-05
1.8750E-01	6.4828E-01	1.0516E-03	5.4540E-04	5.8103E-04	2.0625E-04	-1.8730E-05
1.9792E-01	6.4730E-01	1.0766E-03	5.4977E-04	5.8907E-04	2.1789E-04	-1.9576E-05
2.0833E-01	6.4628E-01	1.1024E-03	5.5450E-04	5.9764E-04	2.2937E-04	-2.0436E-05
2.1875E-01	6.4522E-01	1.1292E-03	5.5930E-04	6.0679E-04	2.4080E-04	-2.1315E-05
2.2917E-01	6.4411E-01	1.1566E-03	5.6448E-04	6.1648E-04	2.5213E-04	-2.2208E-05
2.3958E-01	6.4295E-01	1.1845E-03	5.6974E-04	6.2675E-04	2.6348E-04	-2.3106E-05
2.5000E-01	6.4175E-01	1.2131E-03	5.7537E-04	6.3746E-04	2.7484E-04	-2.3994E-05
2.6042E-01	6.4050E-01	1.2425E-03	5.8104E-04	6.4855E-04	2.8630E-04	-2.4860E-05
2.7083E-01	6.3921E-01	1.2729E-03	5.8704E-04	6.5989E-04	2.9782E-04	-2.5700E-05
2.8125E-01	6.3788E-01	1.3044E-03	5.9298E-04	6.7148E-04	3.0943E-04	-2.6520E-05
2.9167E-01	6.3650E-01	1.3371E-03	5.9921E-04	6.8329E-04	3.2109E-04	-2.7325E-05
3.0208E-01	6.3509E-01	1.3706E-03	6.0538E-04	6.9538E-04	3.3279E-04	-2.8120E-05
3.1250E-01	6.3363E-01	1.4046E-03	6.1183E-04	7.0775E-04	3.4454E-04	-2.8909E-05
3.2292E-01	6.3214E-01	1.4389E-03	6.1826E-04	7.2055E-04	3.5633E-04	-2.9696E-05
3.3333E-01	6.3060E-01	1.4735E-03	6.2505E-04	7.3376E-04	3.6818E-04	-3.0490E-05
3.4375E-01	6.2902E-01	1.5084E-03	6.3185E-04	7.4743E-04	3.8005E-04	-3.1294E-05
			...			

Table A.1: Flow mean quantities – variable modes with regularity conditions

r	$\langle u \rangle$	$\langle uu \rangle$	$\langle vv \rangle$	$\langle ww \rangle$	$\langle uv \rangle$	$\langle \tau \rangle$
			...			
3.5417E-01	6.2741E-01	1.5438E-03	6.3904E-04	7.6144E-04	3.9200E-04	-3.2104E-05
3.6458E-01	6.2575E-01	1.5799E-03	6.4624E-04	7.7578E-04	4.0398E-04	-3.2911E-05
3.7500E-01	6.2405E-01	1.6168E-03	6.5379E-04	7.9027E-04	4.1606E-04	-3.3710E-05
3.8542E-01	6.2231E-01	1.6547E-03	6.6129E-04	8.0494E-04	4.2816E-04	-3.4498E-05
3.9583E-01	6.2052E-01	1.6937E-03	6.6910E-04	8.1967E-04	4.4038E-04	-3.5271E-05
4.0625E-01	6.1871E-01	1.7341E-03	6.7678E-04	8.3457E-04	4.5262E-04	-3.6020E-05
4.1667E-01	6.1685E-01	1.7757E-03	6.8477E-04	8.4959E-04	4.6501E-04	-3.6739E-05
4.2708E-01	6.1496E-01	1.8184E-03	6.9264E-04	8.6486E-04	4.7740E-04	-3.7430E-05
4.3750E-01	6.1303E-01	1.8620E-03	7.0083E-04	8.8022E-04	4.8993E-04	-3.8099E-05
4.4792E-01	6.1107E-01	1.9064E-03	7.0891E-04	8.9568E-04	5.0239E-04	-3.8758E-05
4.5833E-01	6.0907E-01	1.9517E-03	7.1735E-04	9.1108E-04	5.1492E-04	-3.9420E-05
4.6875E-01	6.0704E-01	1.9980E-03	7.2563E-04	9.2652E-04	5.2728E-04	-4.0090E-05
4.7917E-01	6.0498E-01	2.0456E-03	7.3428E-04	9.4200E-04	5.3969E-04	-4.0758E-05
4.8958E-01	6.0288E-01	2.0947E-03	7.4270E-04	9.5768E-04	5.5192E-04	-4.1408E-05
5.0000E-01	6.0075E-01	2.1455E-03	7.5138E-04	9.7346E-04	5.6417E-04	-4.2034E-05
5.1042E-01	5.9859E-01	2.1979E-03	7.5970E-04	9.8942E-04	5.7616E-04	-4.2652E-05
5.2083E-01	5.9640E-01	2.2519E-03	7.6821E-04	1.0054E-03	5.8808E-04	-4.3290E-05
5.3125E-01	5.9417E-01	2.3077E-03	7.7619E-04	1.0215E-03	5.9966E-04	-4.3964E-05
5.4167E-01	5.9191E-01	2.3653E-03	7.8430E-04	1.0375E-03	6.1115E-04	-4.4685E-05
5.5208E-01	5.8961E-01	2.4248E-03	7.9184E-04	1.0538E-03	6.2225E-04	-4.5453E-05
5.6250E-01	5.8727E-01	2.4861E-03	7.9946E-04	1.0702E-03	6.3328E-04	-4.6267E-05
5.7292E-01	5.8489E-01	2.5489E-03	8.0643E-04	1.0869E-03	6.4393E-04	-4.7125E-05
5.8333E-01	5.8246E-01	2.6133E-03	8.1349E-04	1.1037E-03	6.5462E-04	-4.8032E-05
5.9375E-01	5.7998E-01	2.6791E-03	8.1973E-04	1.1205E-03	6.6499E-04	-4.8997E-05
6.0417E-01	5.7746E-01	2.7469E-03	8.2599E-04	1.1368E-03	6.7550E-04	-5.0030E-05
6.1458E-01	5.7488E-01	2.8173E-03	8.3129E-04	1.1528E-03	6.8572E-04	-5.1124E-05
6.2500E-01	5.7224E-01	2.8913E-03	8.3643E-04	1.1679E-03	6.9620E-04	-5.2257E-05
6.3542E-01	5.6954E-01	2.9697E-03	8.4041E-04	1.1826E-03	7.0637E-04	-5.3430E-05
6.4583E-01	5.6678E-01	3.0532E-03	8.4412E-04	1.1966E-03	7.1674E-04	-5.4689E-05
6.5625E-01	5.6396E-01	3.1425E-03	8.4647E-04	1.2106E-03	7.2664E-04	-5.6099E-05
6.6667E-01	5.6106E-01	3.2383E-03	8.4848E-04	1.2243E-03	7.3678E-04	-5.7717E-05
6.7708E-01	5.5807E-01	3.3414E-03	8.4881E-04	1.2380E-03	7.4646E-04	-5.9578E-05
6.8750E-01	5.5497E-01	3.4526E-03	8.4864E-04	1.2512E-03	7.5649E-04	-6.1723E-05
6.9792E-01	5.5176E-01	3.5727E-03	8.4648E-04	1.2642E-03	7.6597E-04	-6.4187E-05
7.0833E-01	5.4842E-01	3.7022E-03	8.4349E-04	1.2763E-03	7.7593E-04	-6.6982E-05
7.1875E-01	5.4493E-01	3.8421E-03	8.3802E-04	1.2873E-03	7.8535E-04	-7.0112E-05
7.2917E-01	5.4126E-01	3.9937E-03	8.3134E-04	1.2963E-03	7.9535E-04	-7.3588E-05
7.3958E-01	5.3742E-01	4.1583E-03	8.2138E-04	1.3037E-03	8.0459E-04	-7.7449E-05
7.5000E-01	5.3336E-01	4.3365E-03	8.0977E-04	1.3090E-03	8.1419E-04	-8.1816E-05
7.6042E-01	5.2906E-01	4.5287E-03	7.9428E-04	1.3130E-03	8.2242E-04	-8.6823E-05
7.7083E-01	5.2450E-01	4.7357E-03	7.7665E-04	1.3153E-03	8.3075E-04	-9.2611E-05
7.8125E-01	5.1961E-01	4.9583E-03	7.5460E-04	1.3162E-03	8.3710E-04	-9.9359E-05
7.9167E-01	5.1435E-01	5.1973E-03	7.3031E-04	1.3152E-03	8.4313E-04	-1.0731E-04
8.0208E-01	5.0865E-01	5.4539E-03	7.0111E-04	1.3124E-03	8.4643E-04	-1.1674E-04
8.1250E-01	5.0244E-01	5.7288E-03	6.6972E-04	1.3073E-03	8.4905E-04	-1.2801E-04
8.2292E-01	4.9559E-01	6.0228E-03	6.3327E-04	1.3006E-03	8.4794E-04	-1.4153E-04
8.3333E-01	4.8799E-01	6.3348E-03	5.9472E-04	1.2916E-03	8.4555E-04	-1.5776E-04
8.4375E-01	4.7948E-01	6.6631E-03	5.5118E-04	1.2796E-03	8.3814E-04	-1.7726E-04
8.5417E-01	4.6989E-01	7.0025E-03	5.0619E-04	1.2635E-03	8.2835E-04	-2.0082E-04
8.6458E-01	4.5898E-01	7.3458E-03	4.5654E-04	1.2419E-03	8.1151E-04	-2.2942E-04
8.7500E-01	4.4647E-01	7.6795E-03	4.0642E-04	1.2144E-03	7.9044E-04	-2.6431E-04
8.8542E-01	4.3200E-01	7.9849E-03	3.5274E-04	1.1789E-03	7.5913E-04	-3.0704E-04
8.9583E-01	4.1513E-01	8.2331E-03	3.0016E-04	1.1351E-03	7.2059E-04	-3.5939E-04
9.0625E-01	3.9531E-01	8.3849E-03	2.4598E-04	1.0787E-03	6.6776E-04	-4.2342E-04
9.1667E-01	3.7191E-01	8.3796E-03	1.9553E-04	1.0098E-03	6.0359E-04	-5.0120E-04
9.2708E-01	3.4415E-01	8.1421E-03	1.4640E-04	9.2387E-04	5.2123E-04	-5.9434E-04
9.3750E-01	3.1123E-01	7.5741E-03	1.0410E-04	8.2386E-04	4.2542E-04	-7.0254E-04
9.4792E-01	2.7243E-01	6.5916E-03	6.6223E-05	7.0543E-04	3.1499E-04	-8.2202E-04
9.5833E-01	2.2732E-01	5.1587E-03	3.7801E-05	5.7319E-04	2.0280E-04	-9.4323E-04
9.6875E-01	1.7614E-01	3.4089E-03	1.6262E-05	4.2065E-04	1.0232E-04	-1.0511E-03
9.7917E-01	1.2002E-01	1.6794E-03	4.9011E-06	2.5516E-04	3.3747E-05	-1.1303E-03
9.8958E-01	6.0757E-02	4.4088E-04	3.0631E-07	8.8298E-05	4.0892E-06	-1.1757E-03
1.0000E+00	0.0000E+00	0.0000E+00	0.0000E+00	0.0000E+00	0.0000E+00	-1.2050E-03

Table A.1: Flow mean quantities – variable modes with regularity conditions (continue)

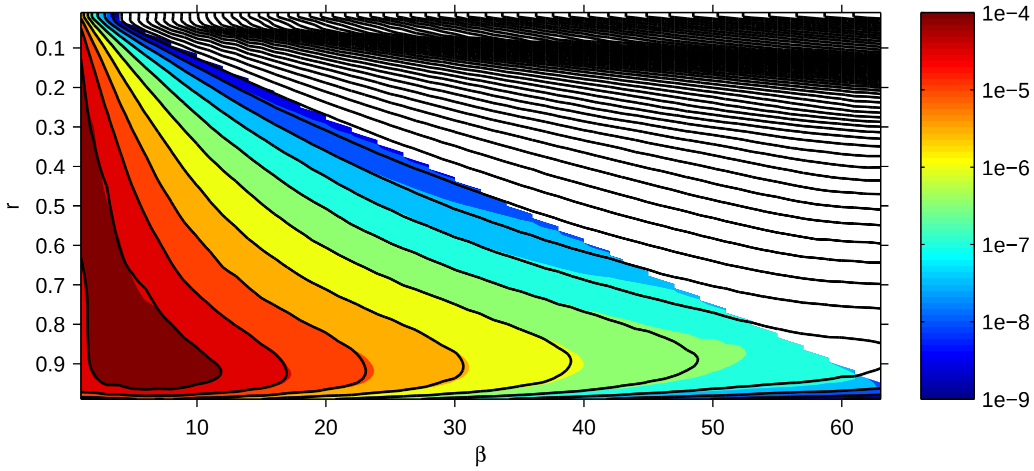

(a) Φ_{uu}

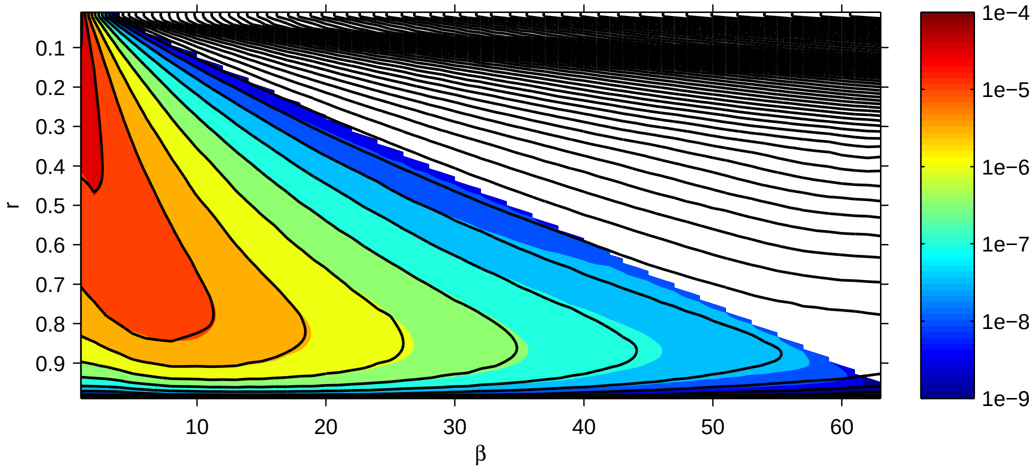

(b) Φ_{vv}

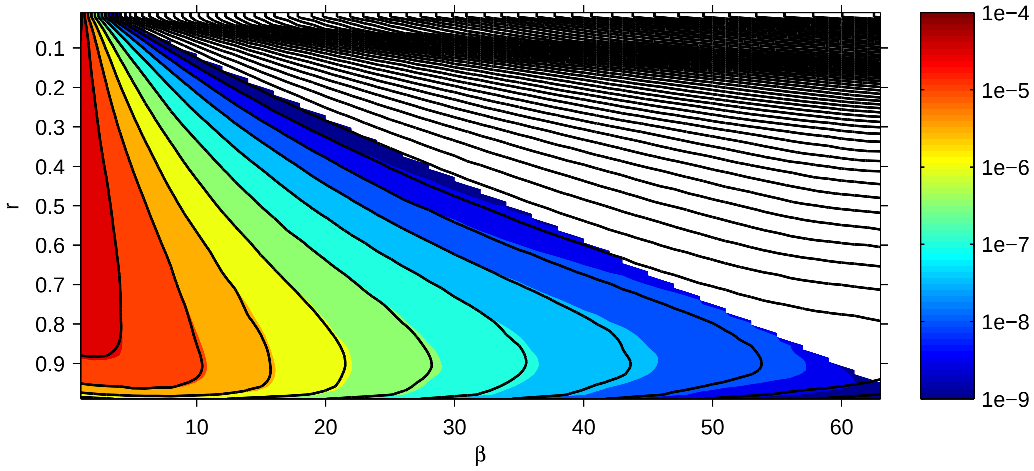

(c) Φ_{ww}

Figure A.1: Azimuthal power spectra of velocity fluctuation – colored surface: variable modes simulation; contour lines: constant modes simulation

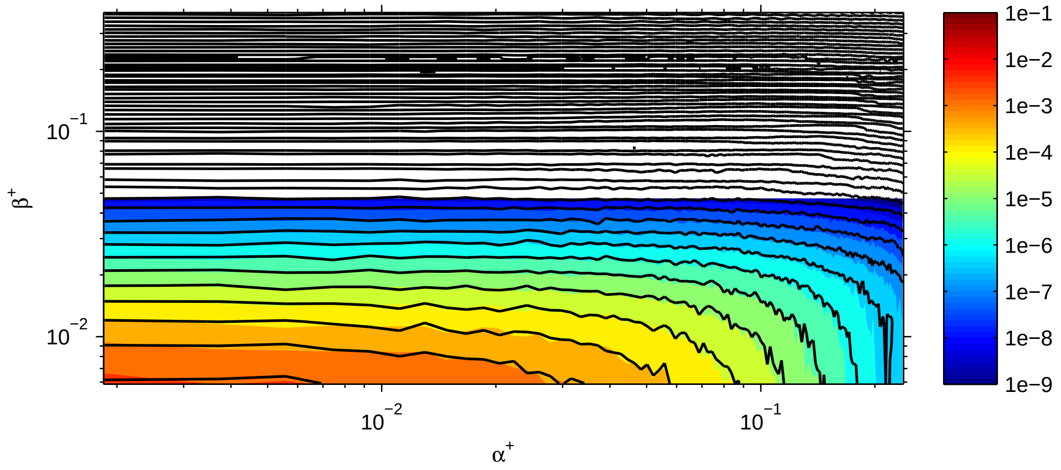

(a) $r = 0.08333$ ($y^+ \approx 156$)

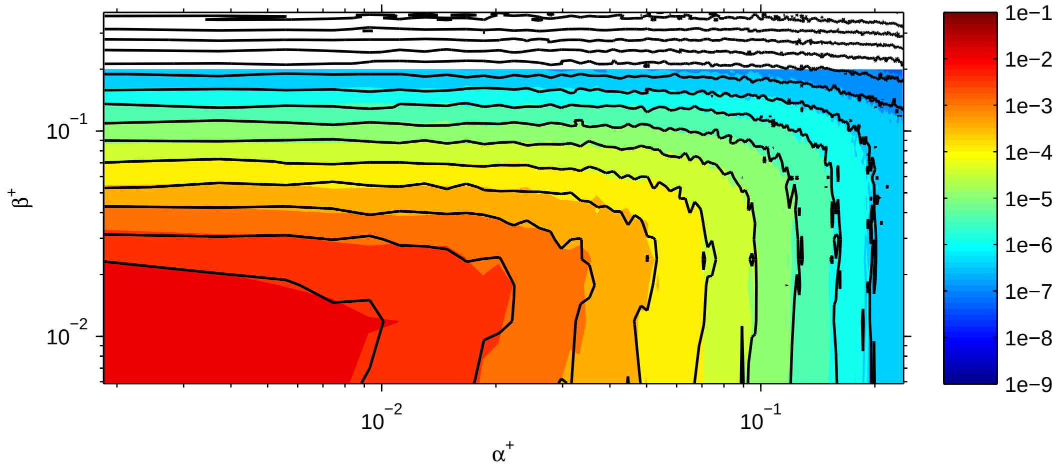

(b) $y = 0.5$ ($y^+ \approx 85$)

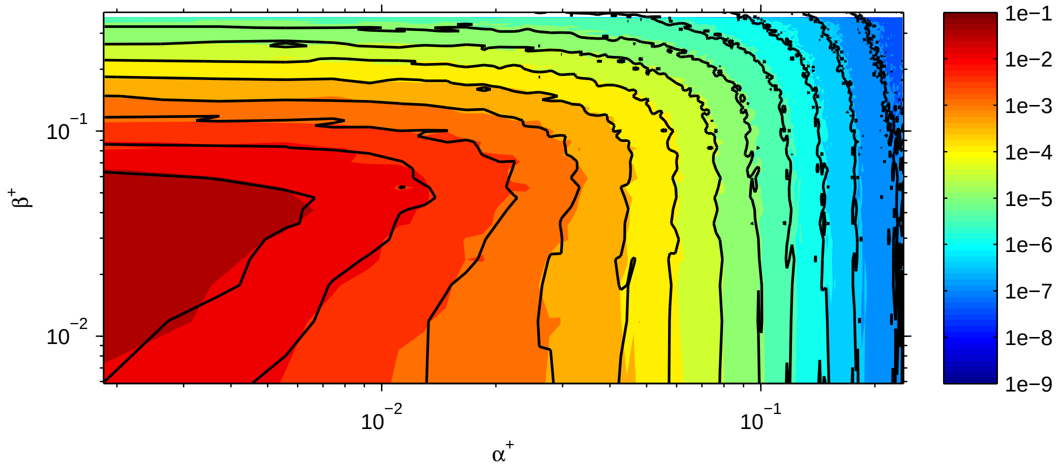

(c) $r = 0.91667$ ($y^+ \approx 14$)

Figure A.2: Power spectra of axial velocity fluctuation Φ^+_{uu} – colored surface: variable modes simulation; contour lines: constant modes simulation

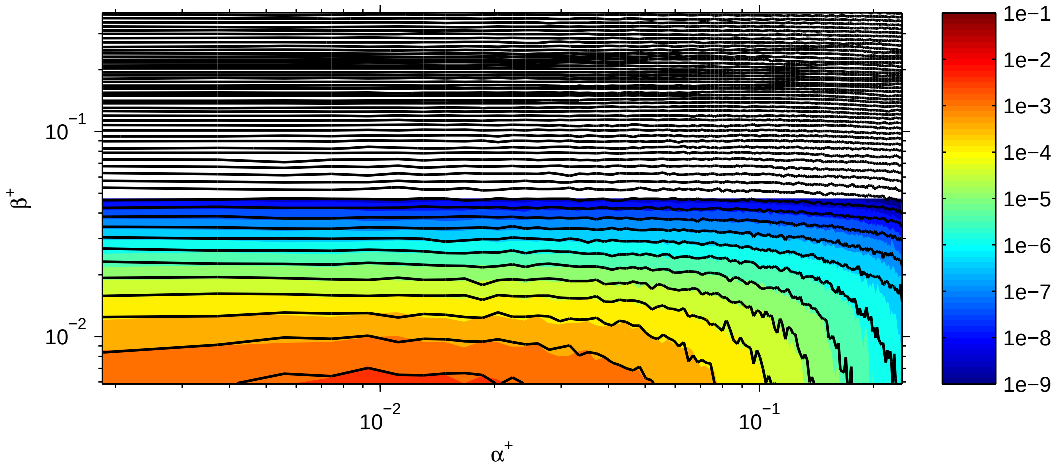

(a) $r = 0.08333$ ($y^+ \approx 156$)

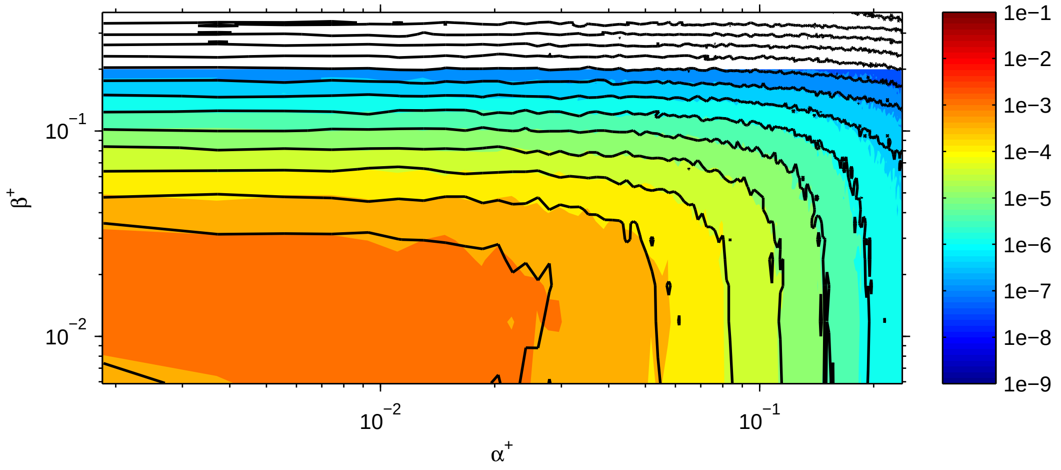

(b) $y = 0.5$ ($y^+ \approx 85$)

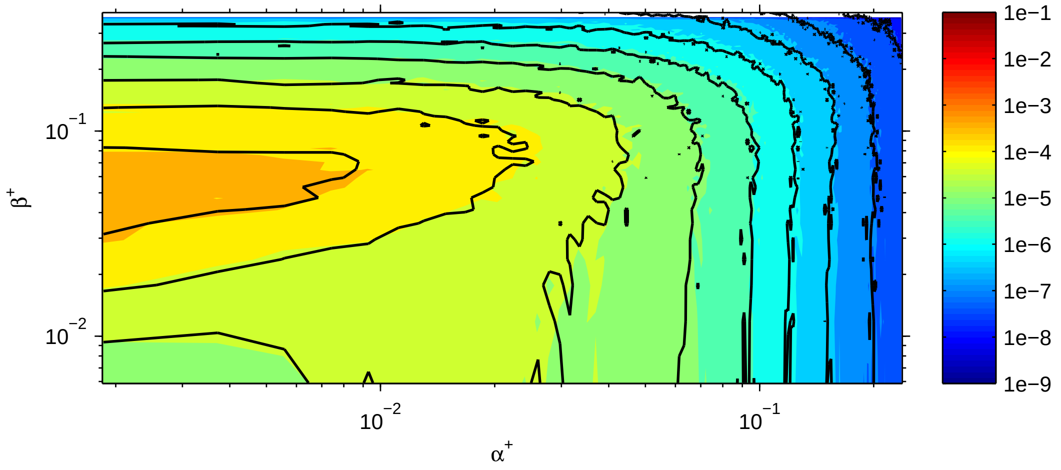

(c) $r = 0.91667$ ($y^+ \approx 14$)

Figure A.3: Power spectra of radial velocity fluctuation Φ_{vv}^+ – colored surface: variable modes simulation; contour lines: constant modes simulation

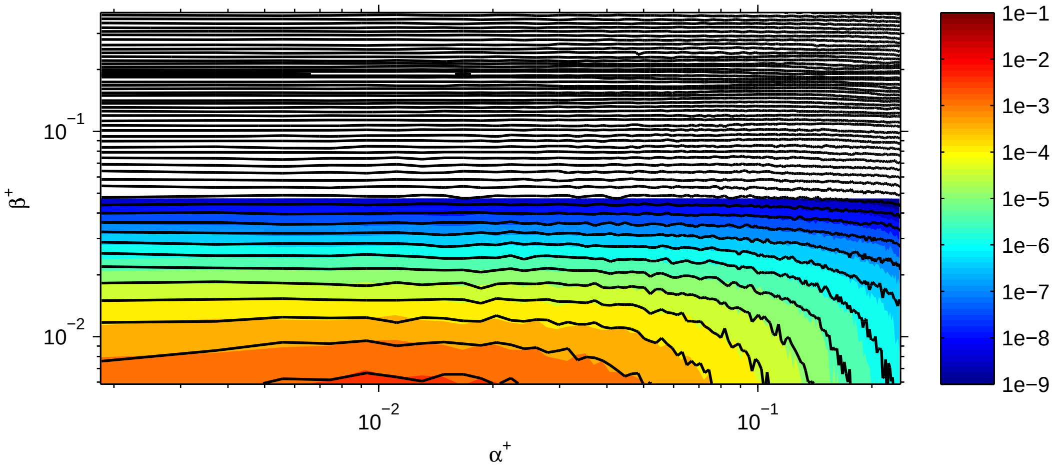

(a) $r = 0.08333$ ($y^+ \approx 156$)

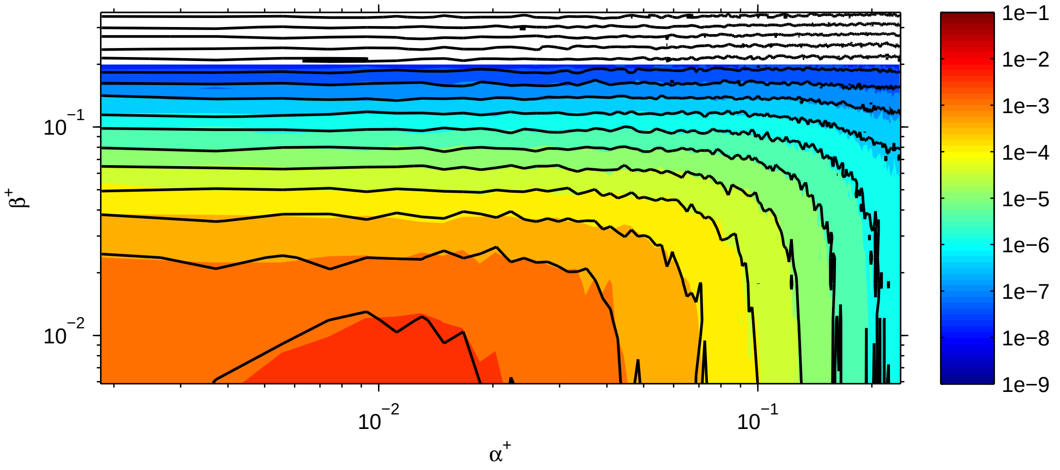

(b) $y = 0.5$ ($y^+ \approx 85$)

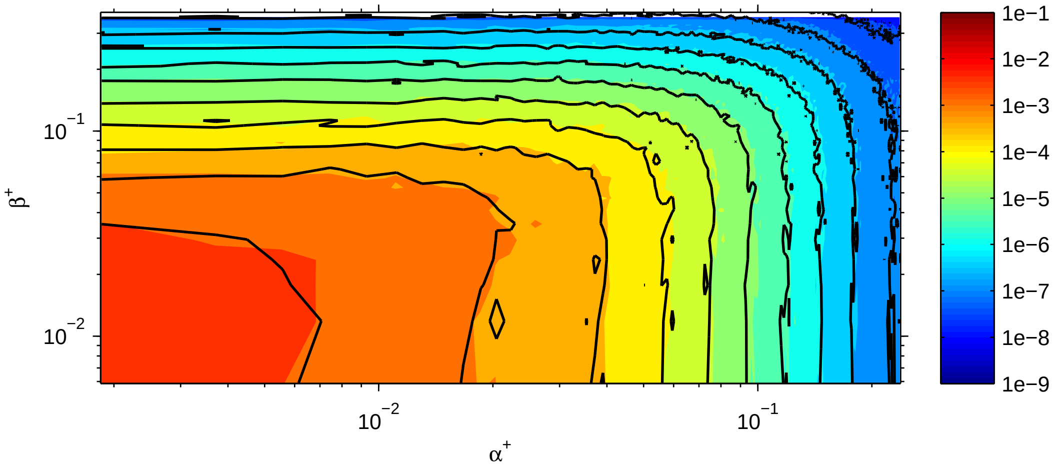

(c) $r = 0.91667$ ($y^+ \approx 14$)

Figure A.4: Power spectra of azimuthal velocity fluctuation Φ^+_{ww} – colored surface: variable modes simulation; contour lines: constant modes simulation

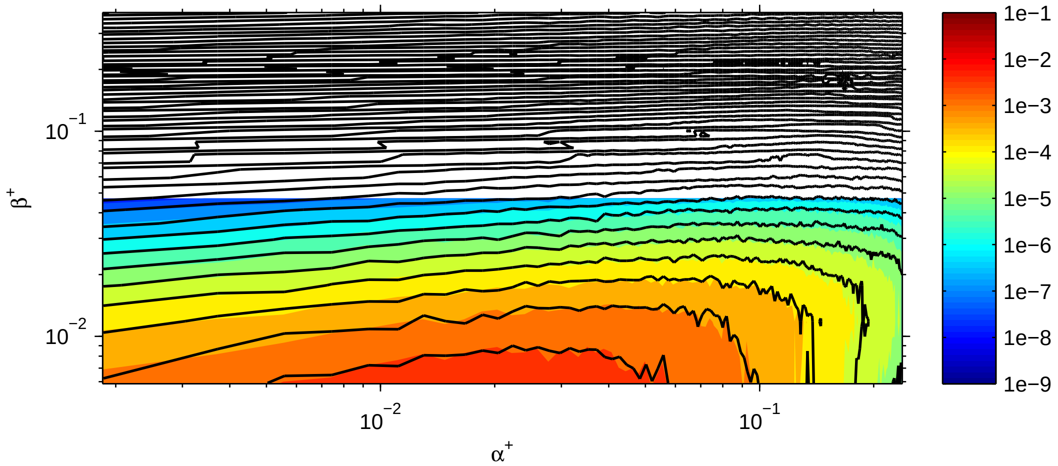

(a) $r = 0.08333$ $(y^+ \approx 156)$

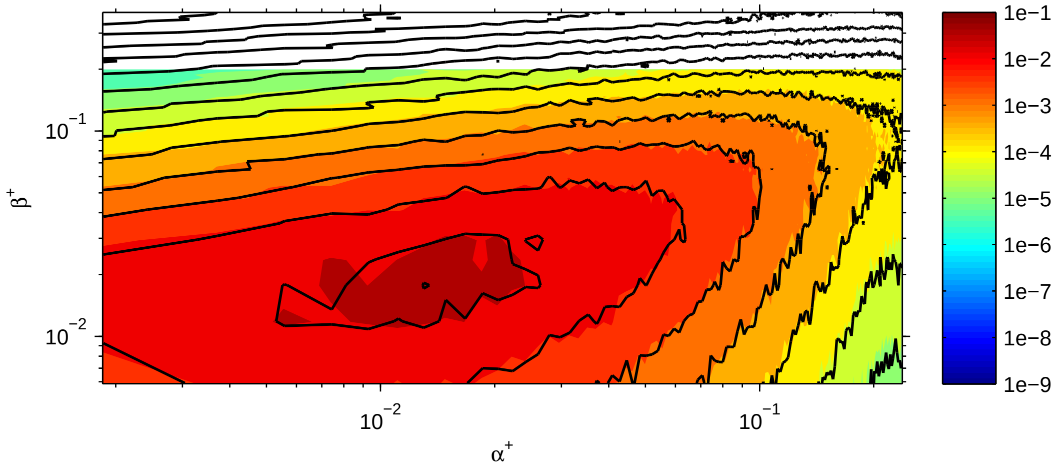

(b) $y = 0.5$ $(y^+ \approx 85)$

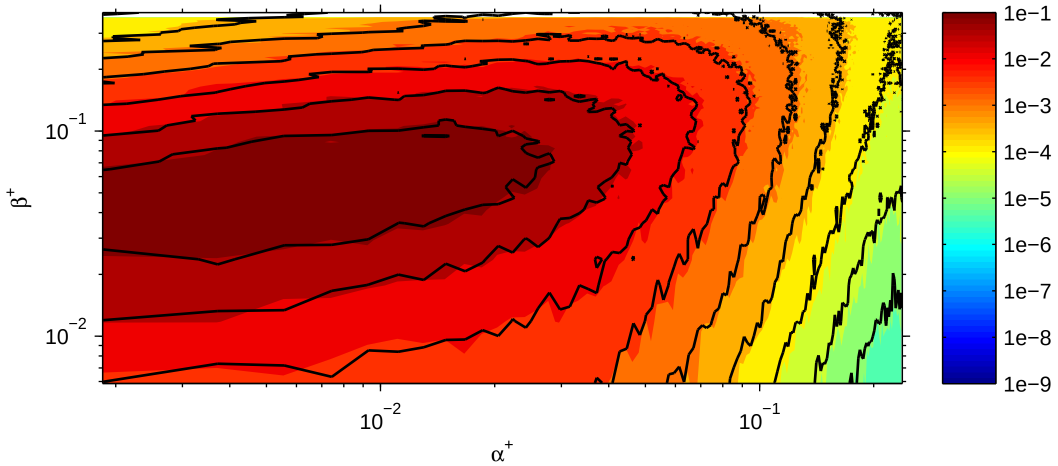

(c) $r = 0.91667$ $(y^+ \approx 14)$

Figure A.5: Premultiplied power spectra of axial velocity fluctuation $\alpha\beta\,\Phi^+_{uu}$ – colored surface: variable modes simulation; contour lines: constant modes simulation

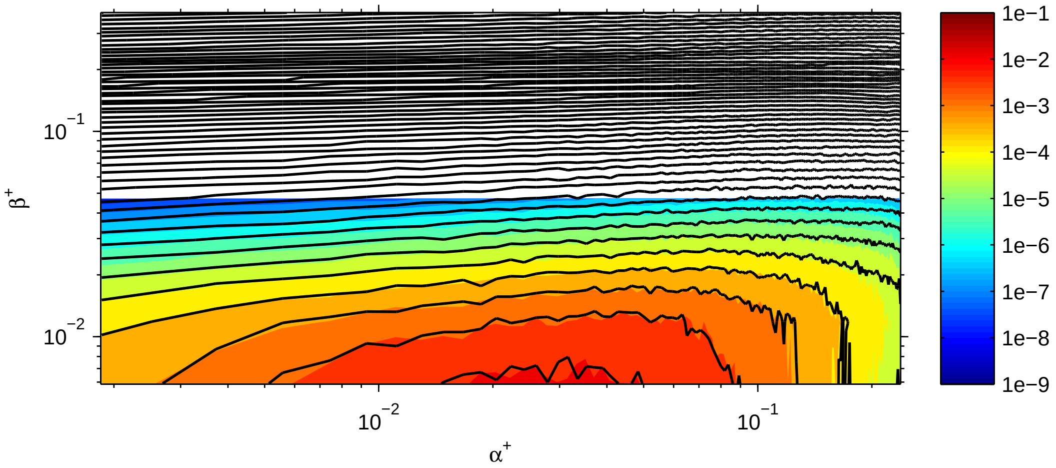

(a) $r = 0.08333$ ($y^+ \approx 156$)

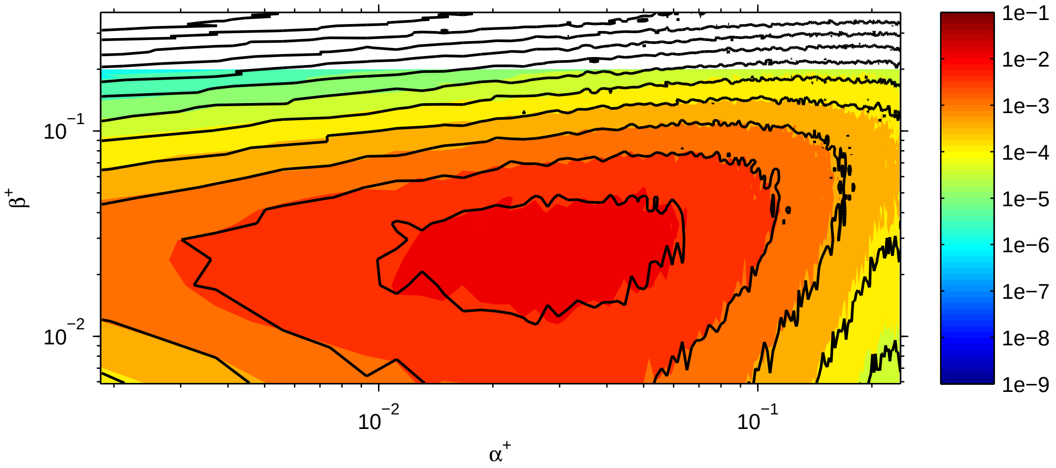

(b) $y = 0.5$ ($y^+ \approx 85$)

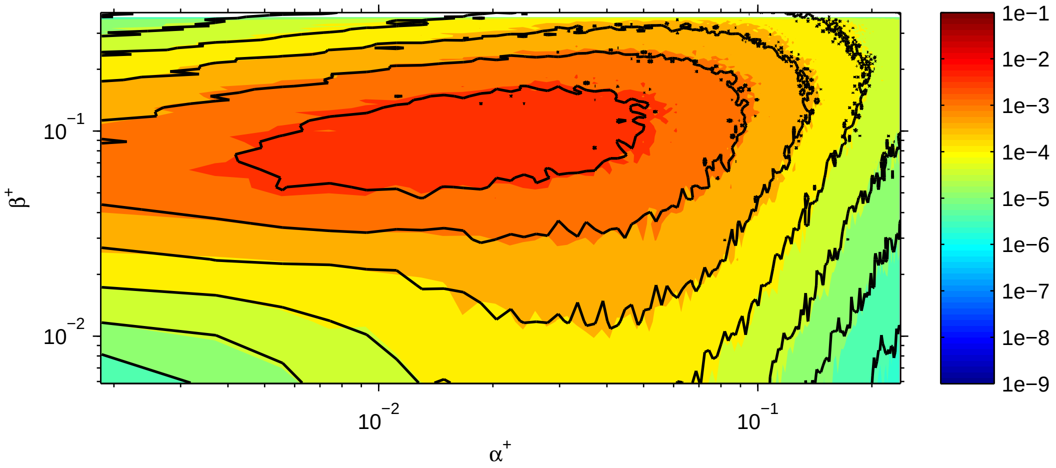

(c) $r = 0.91667$ ($y^+ \approx 14$)

Figure A.6: Premultiplied power spectra of radial velocity fluctuation $\alpha\beta\,\Phi^+_{vv}$ – colored surface: variable modes simulation; contour lines: constant modes simulation

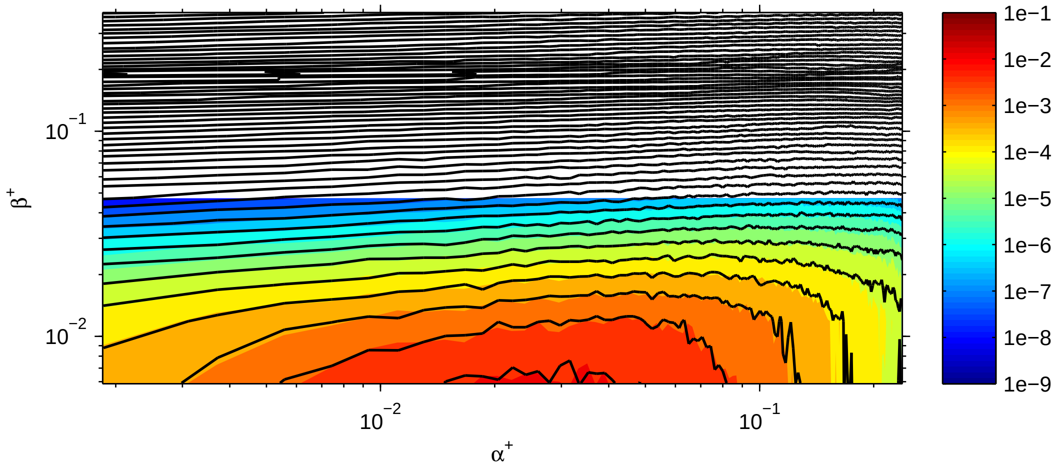

(a) $r = 0.08333$ ($y^+ \approx 156$)

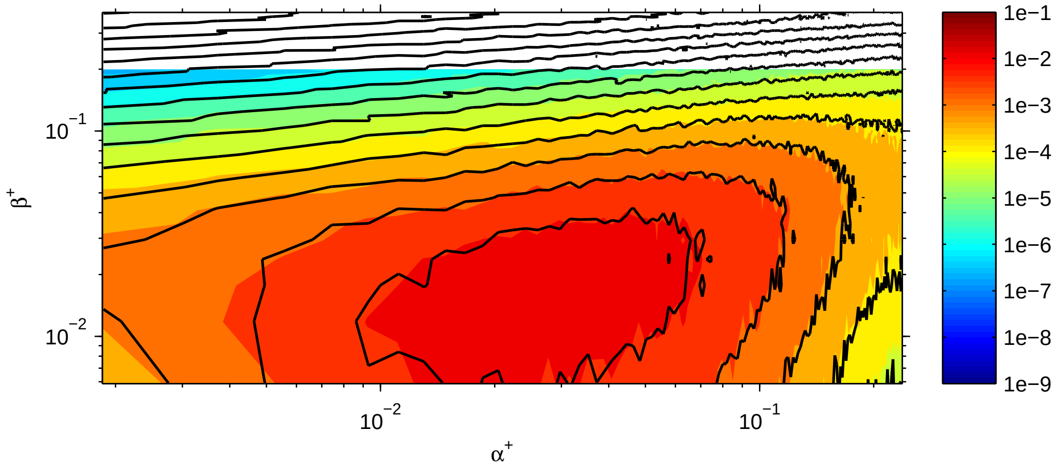

(b) $y = 0.5$ ($y^+ \approx 85$)

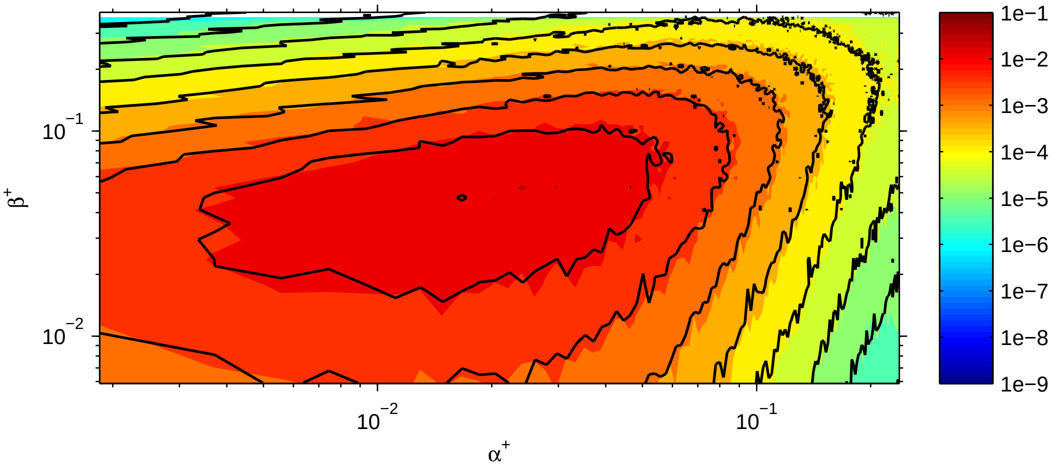

x

(c) $r = 0.91667$ ($y^+ \approx 14$)

Figure A.7: Premultiplied power spectra of azimuthal velocity fluctuation $\alpha\beta\,\Phi^+_{ww}$ – colored surface: variable modes simulation; contour lines: constant modes simulation

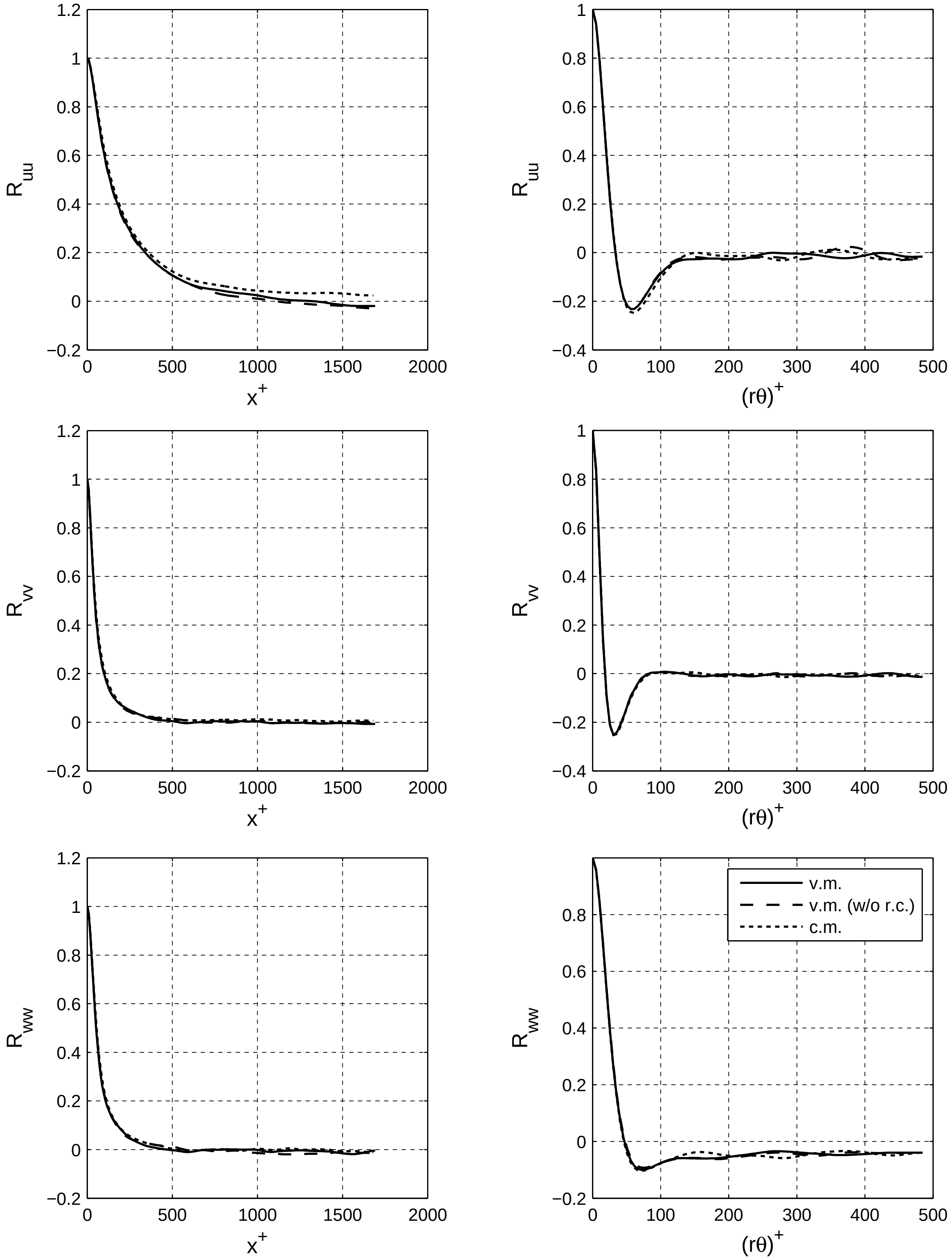

Figure A.8: Correlations of velocity fluctuation at $r = 0.91667\,(y^+ \approx 14)$

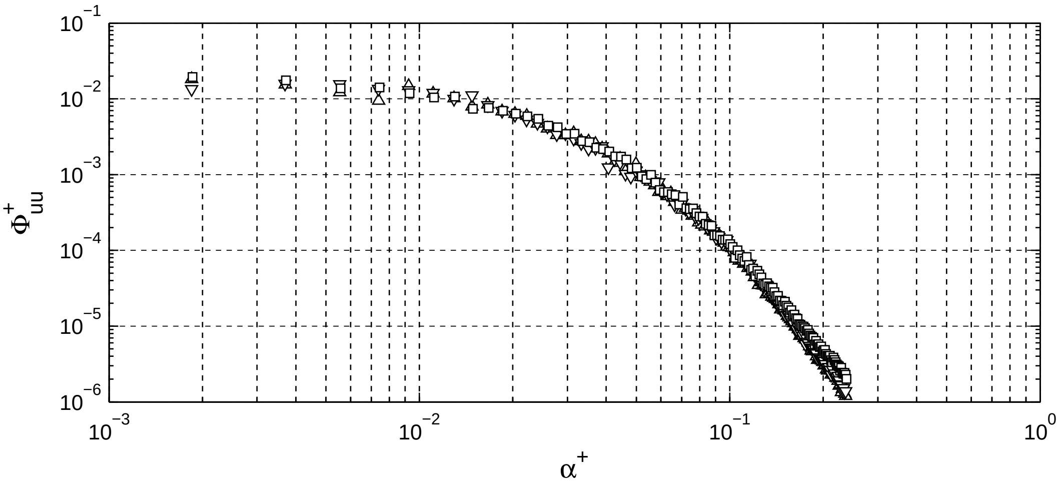

(a) $r = 0.08333$ ($y^+ \approx 156$)

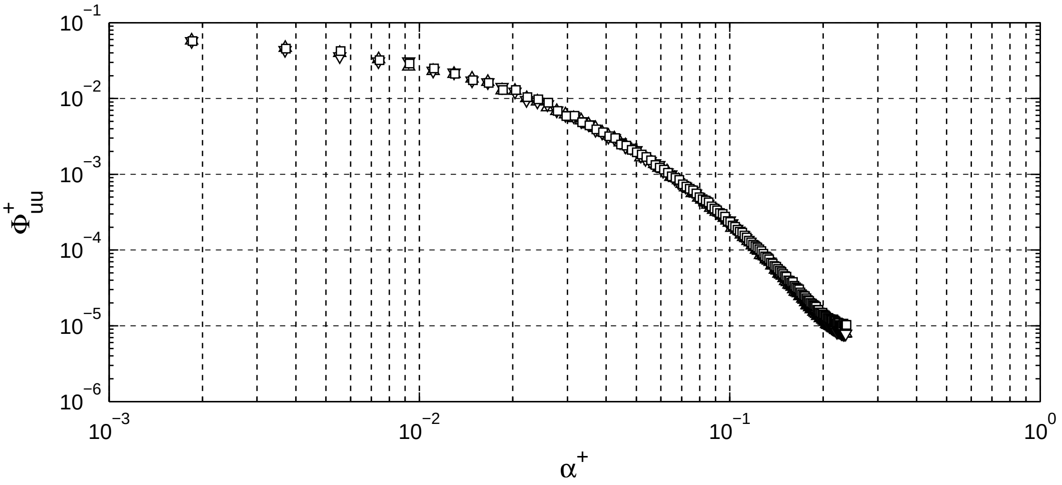

(b) $r = 0.5$ ($y^+ \approx 85$)

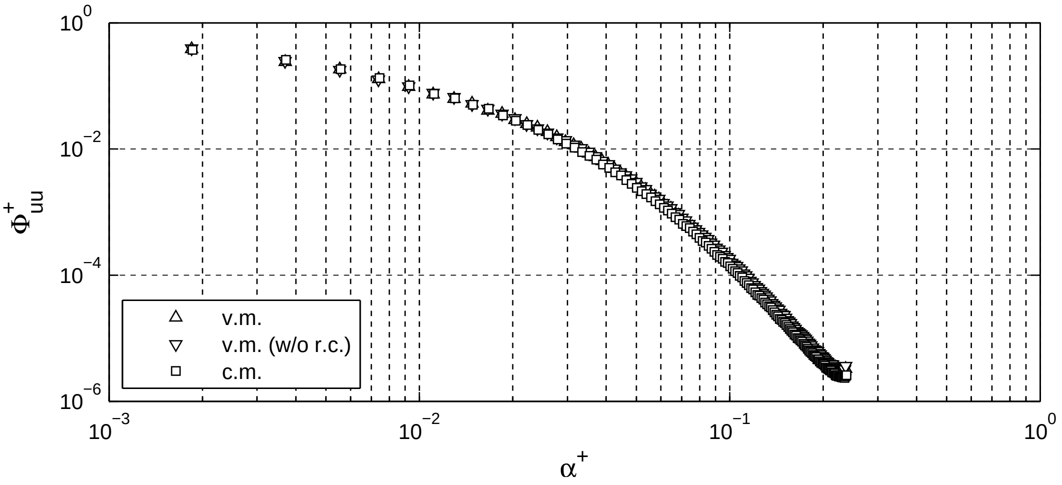

(c) $r = 0.91667$ ($y^+ \approx 14$)

Figure A.9: Axial power spectra of axial velocity fluctuation

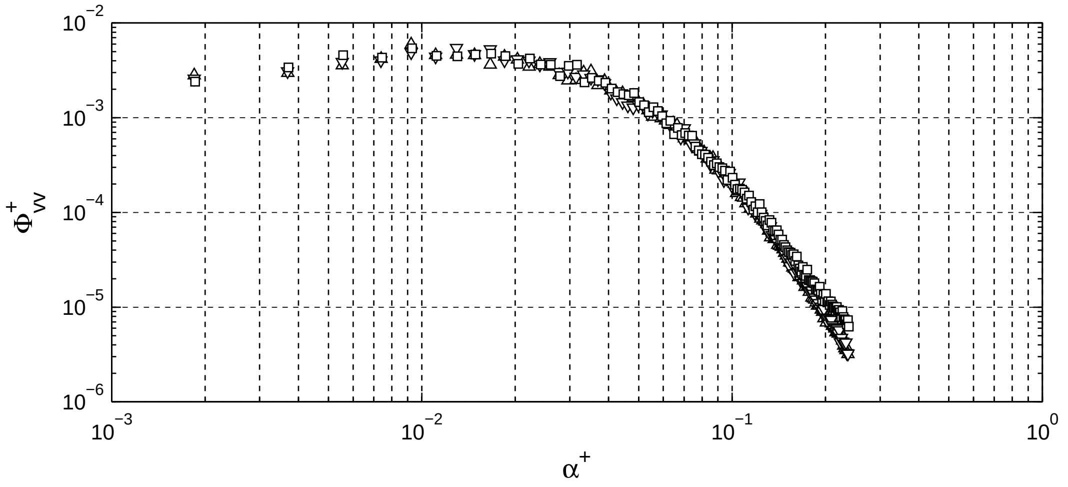

(a) $r = 0.08333$ ($y^+ \approx 156$)

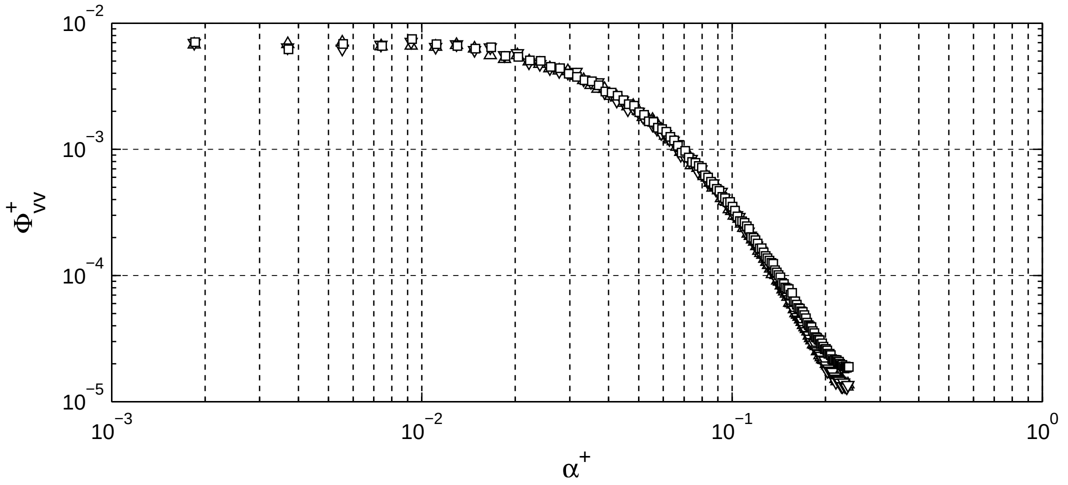

(b) $r = 0.5$ ($y^+ \approx 85$)

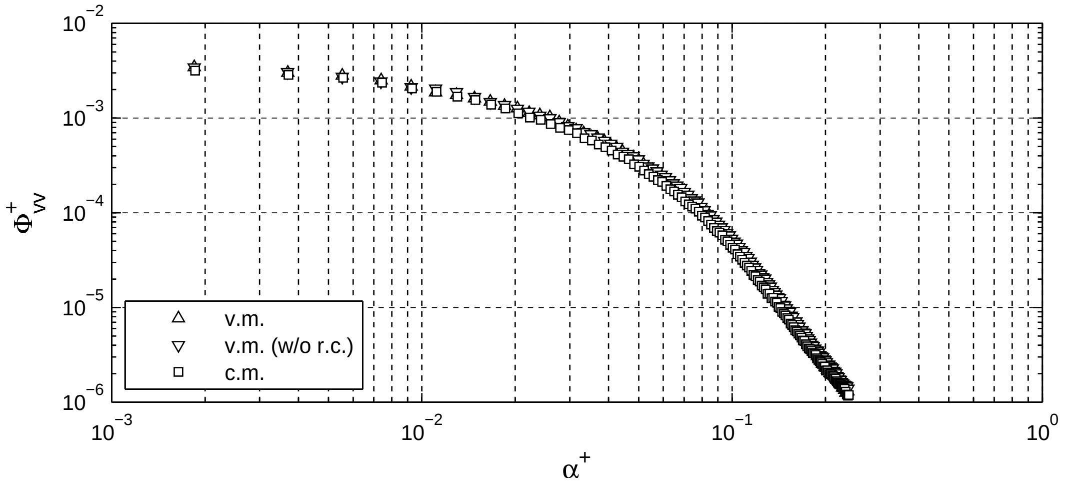

(c) $r = 0.91667$ ($y^+ \approx 14$)

Figure A.10: Axial power spectra of radial velocity fluctuation

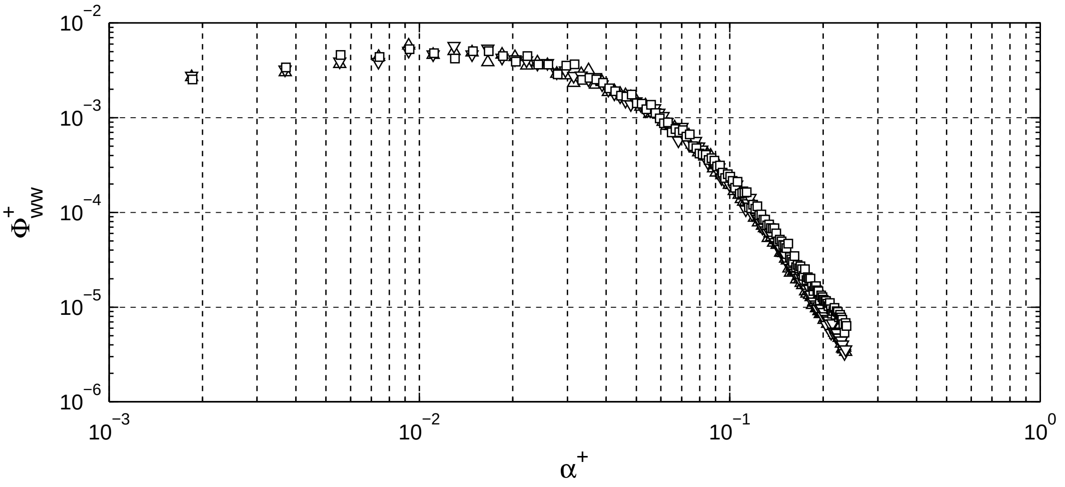

(a) $r = 0.08333$ ($y^+ \approx 156$)

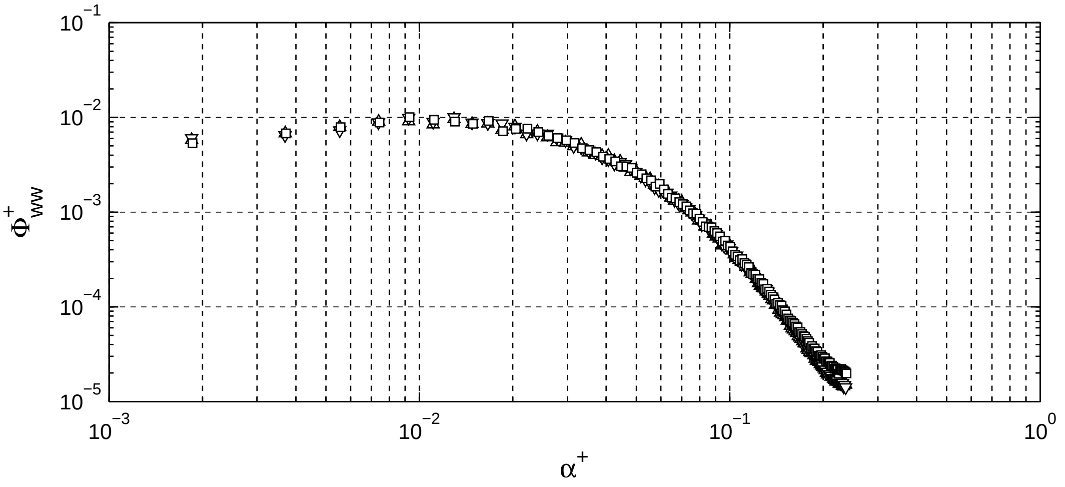

(b) $y = 0.5$ ($n^+ \approx 85$)

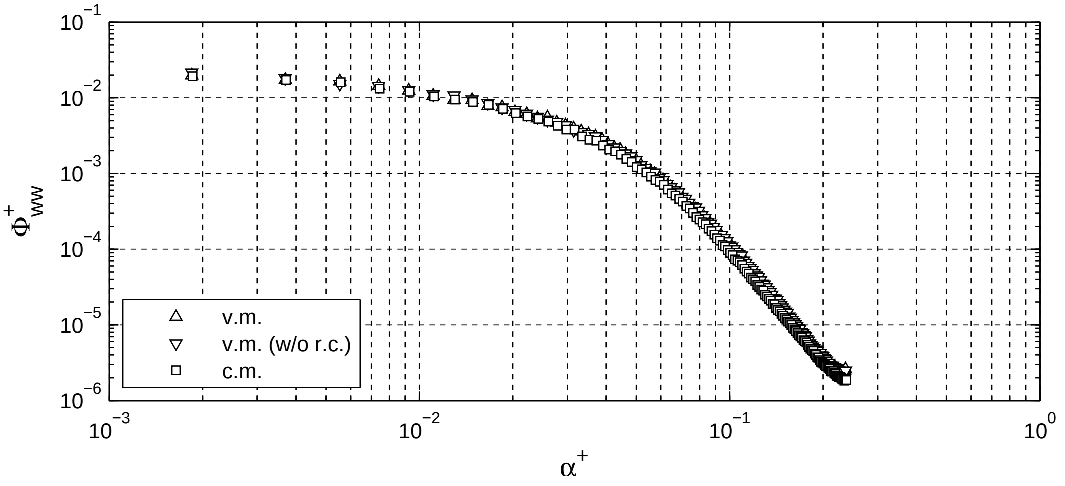

(c) $r = 0.91667$ ($y^+ \approx 14$)

Figure A.11: Axial power spectra of azimuthal velocity fluctuation

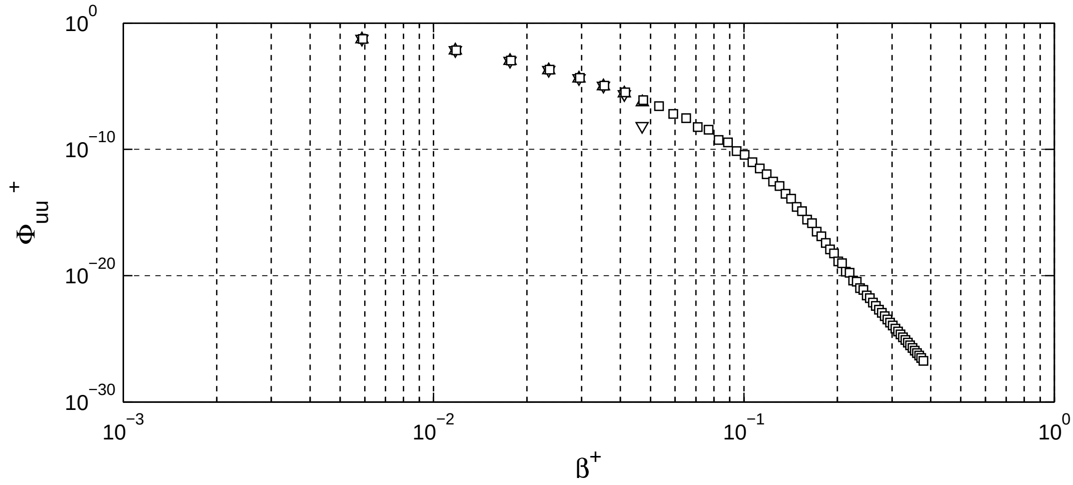

(a) $r = 0.08333$ ($y^+ \approx 156$)

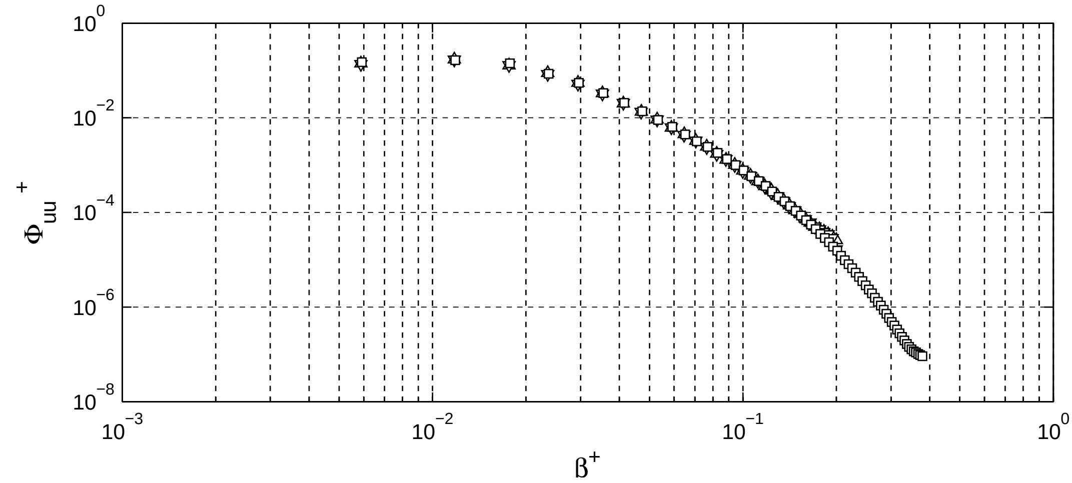

(b) $r = 0.5$ ($y^+ \approx 85$)

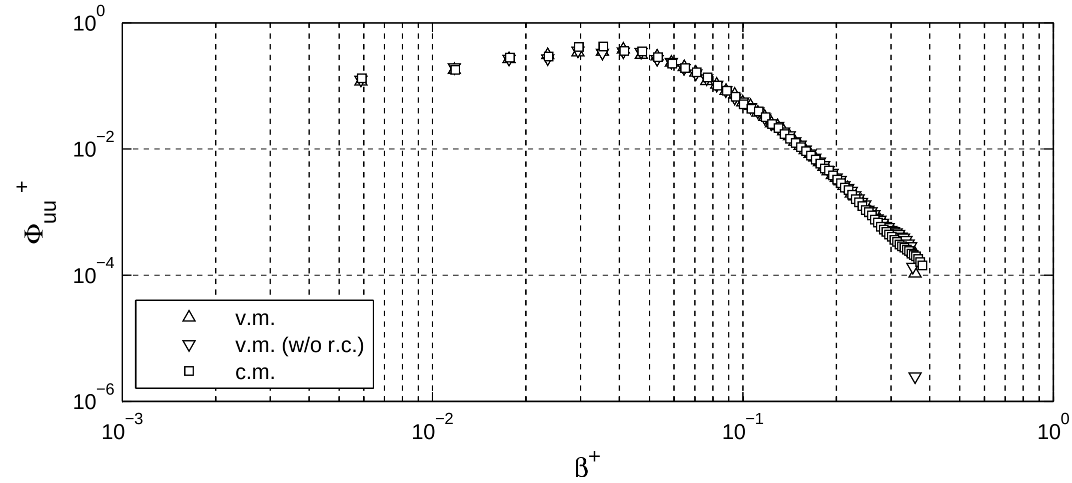

(c) $r = 0.91667$ ($y^+ \approx 14$)

Figure A.12: Azimuthal power spectra of axial velocity fluctuation

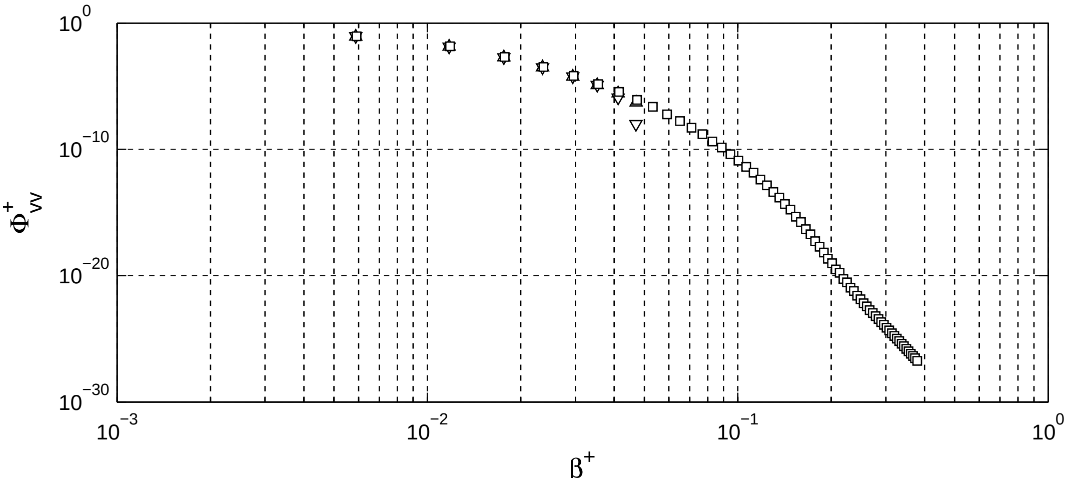

(a) $r = 0.08333$ ($y^+ \approx 156$)

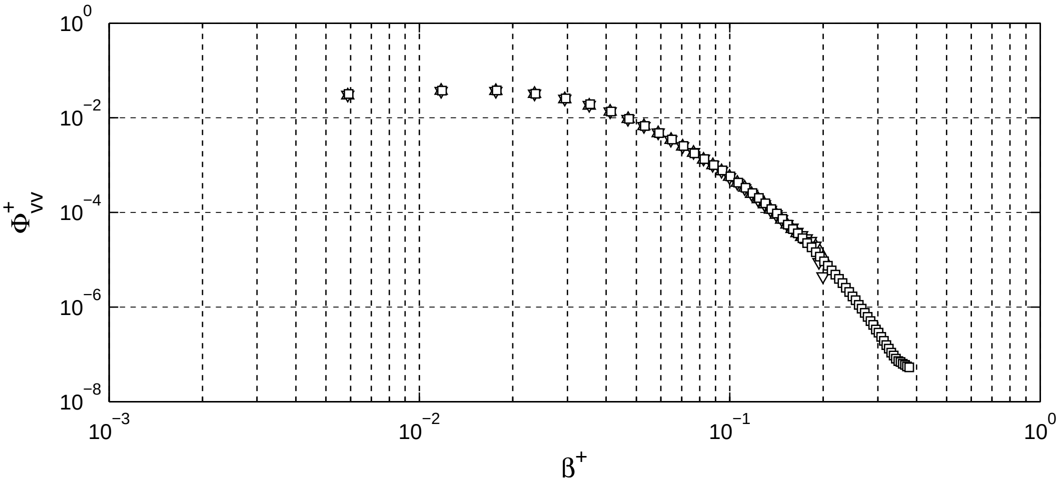

(b) $r = 0.5$ ($y^+ \approx 85$)

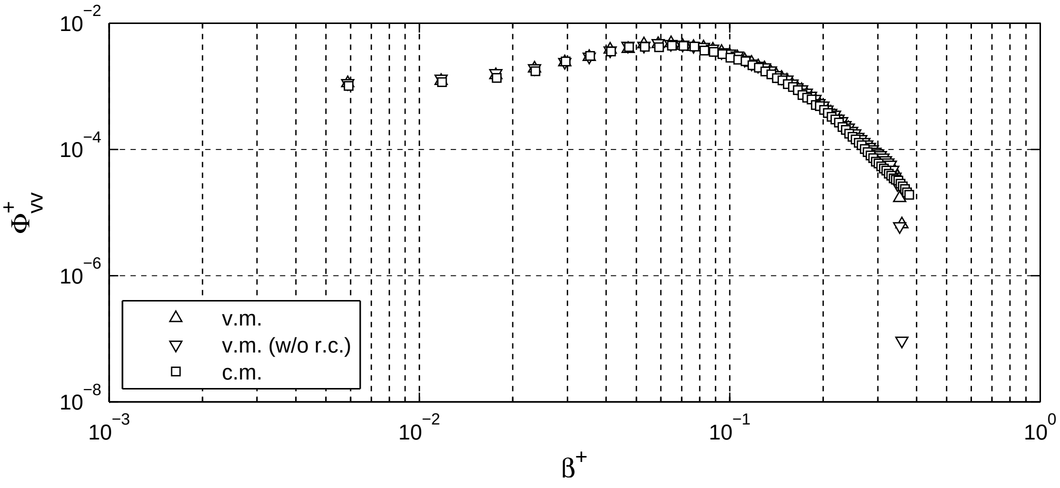

(c) $r = 0.91667$ ($y^+ \approx 14$)

Figure A.13: Azimuthal power spectra of radial velocity fluctuation

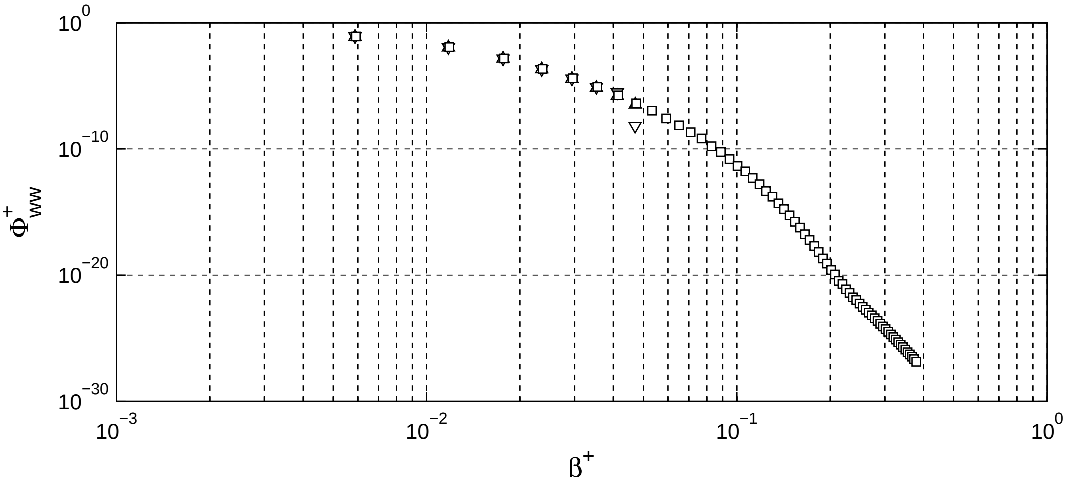

(a) $r = 0.08333$ ($y^+ \approx 156$)

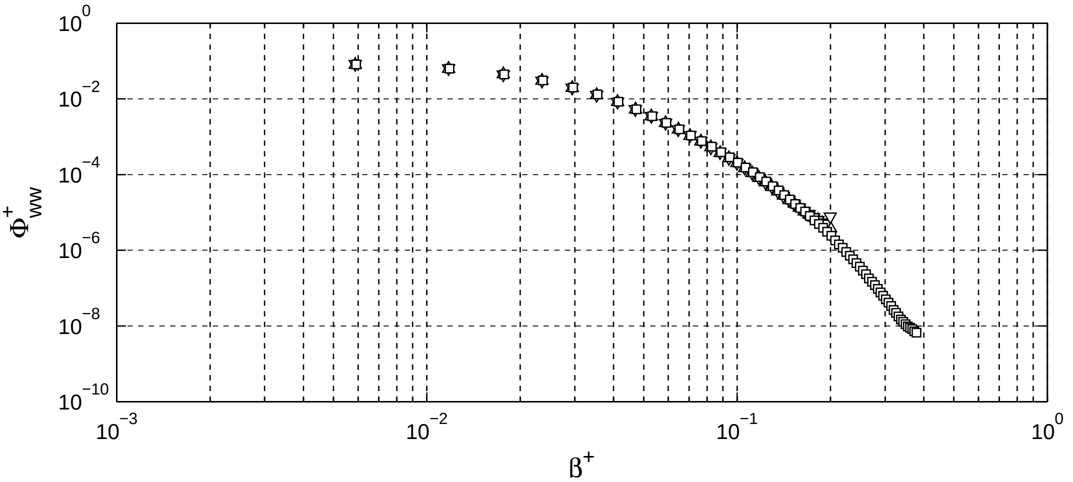

(b) $y = 0.5$ ($y^+ \approx 85$)

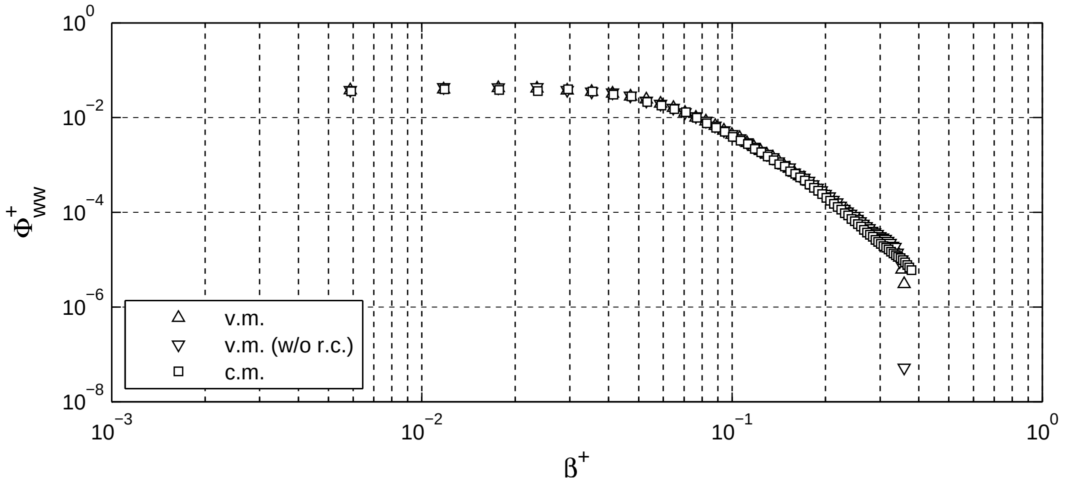

(c) $r = 0.91667$ ($y^+ \approx 14$)

Figure A.14: Azimuthal power spectra of azimuthal velocity fluctuation

LIST OF FIGURES

1.1 Azimuthal resolution issue 2

2.1 Coordinate system 5
2.2 Finite-differences accuracy 10
2.3 Finite-differences accuracy 11
2.4 Variable azimuthal modes 12
2.5 Computational cost 14
2.6 Cluster architecure 17
2.7 Radial partition 17
2.8 Load-balancing weight function 18

3.1 Optimal energy growth function 25
3.2 Optimal perturbation in primitive variables 25
3.3 Energy transient growth 26
3.4 Coupling 27
3.5 Influence of $k(0)$ 27
3.6 Mean flow 28
3.7 Influence of CFL number 28

4.1 k during transition 30
4.2 Mean flow during transition 30
4.3 Evolution of mean velocity magnitude during transition 31
4.3 Evolution of mean velocity magnitude during transition 32
4.4 Perturbation energy evolution for fully turbulent flow 33
4.5 Premultiplied axial power spectrum of axial velocity 34
4.6 Mean velocity profile 35
4.7 Reynolds mean stresses 35
4.8 Azimuthal power spectra of axial velocity fluctuation Φ_{uu} along radial direction 36
4.9 Azimuthal power spectra of axial velocity fluctuation Φ_{uu} 37
4.10 Time step 38
4.11 Mean χ distribution 38

5.1 Azimuthal power spectra of axial velocity fluctuation Φ_{uu} along radial direction 42

A.1 Azimuthal power spectra of velocity fluctuation 51
A.2 Power spectra of axial velocity fluctuation 52
A.3 Power spectra of radial velocity fluctuation 53
A.4 Power spectra of azimuthal velocity fluctuation 54

A.5 Premultiplied power spectra of axial velocity fluctuation 55
A.6 Premultiplied power spectra of radial velocity fluctuation 56
A.7 Premultiplied power spectra of azimuthal velocity fluctuation 57
A.8 Correlations of velocity fluctuation at $r = 0.91667$ ($y^+ \approx 14$) 58
A.9 Axial power spectra of axial velocity fluctuation 59
A.10 Axial power spectra of radial velocity fluctuation 60
A.11 Axial power spectra of azimuthal velocity fluctuation 61
A.12 Azimuthal power spectra of axial velocity fluctuation 62
A.13 Azimuthal power spectra of radial velocity fluctuation 63
A.14 Azimuthal power spectra of azimuthal velocity fluctuation 64

LIST OF TABLES

1.1 State of the art in pipe flow simulation 2

2.1 Runtime file structure 16

3.1 DNS parameters 26

4.1 DNS parameters 29
4.2 Initial condition 29
4.3 Global properties for mean turbulent flow 33
4.4 Number of time integration steps from t=500 to t=900 38

A.1 Flow mean quantities 49
A.1 Flow mean quantities (continue) 50